

**Strain distribution of buckled multilayer systems  
and its influence on the development  
of asymmetric parasitic folds**

Diploma thesis by  
Marcel Frehner

Swiss Federal Institute of Technology (ETH) Zurich  
Department of Earth Science  
Geological Institute

October 2005

Supervisor  
Dr. Stefan Schmalholz

© Copyright 2005

The author hereby agrees that this diploma thesis may be copied and used for private and personal scientific use. However, the making of multiple copies of the thesis or use of the thesis for commercial purposes is strictly prohibited. When making use of the results found in this thesis, the normal scientific methods of citation are to be followed.

# Abstract

In the first part a finite element code for incompressible linear viscous media is used to investigate the strain-evolution and distribution in single layer and double layer folds embedded in a weaker matrix. The concept of finite strain ellipses, which is long-established in the geological community but rarely applied to numerical models, is used to visualize the finite strain in two-dimensions. The single layer system shows a clear distinction of the deformation mechanism between the layer and the surrounding matrix. While the stiff layer is dominated by rigid body rotation without much shape change, the opposite is true for the matrix. Two different types of neutral lines are to be distinguished, the incremental and the finite neutral line, the incremental neutral line moves earlier than the finite neutral line from the outer arc to the inner arc of the fold.

The simulation of double layer folds is compared with a multilayer stack bounded by two much thicker layers. This comparison suggests that a double layer system is not influenced by the presence or absence of a multilayer stack situated in between. The deformation history between the two thick layers is tripartite with an initial layer-parallel compression without buckling of the thick layers, a buckling phase with shear deformation between the layers and a final amplifying phase with flattening normal to the layers between the fold limbs. During the first phase the multilayer stack between the two thick layers is folded and the superposed thin layers build vertical stacks of symmetrical folds. These stacks are almost passively deformed during the second and the third phase but the folds become asymmetric. The amplitude of such a fold stack at the transition from the first to the second deformation phase determines, whether it outlasts the flattening of the third phase or not. Besides the initial perturbation, the number of thin layers effects amplification during the first deformation phase. A multilayer stack with a high number of layers amplifies faster and has a higher chance to outlast the flattening phase and to develop asymmetric parasitic folds.

The finite element code and all visualization programs used for this study are self-developed, which was also the main aim of this diploma thesis.

# Table of contents

<b>Abstract.....</b>	<b>II</b>
<b>Chapter 1: Introduction.....</b>	<b>1</b>
<b>Chapter 2: Methods.....</b>	<b>3</b>
2.1. Introduction.....	3
2.2. Finite element formulation of the mechanical equations.....	3
2.3. The use of the Uzawa iteration algorithm.....	6
2.4. Numerical integration on the Q9/3 element.....	6
2.5. Normalization and boundary conditions.....	7
2.6. Benchmarks.....	8
2.6.1. Single layer fold growth rate.....	8
2.6.2. Pressure field around a rigid inclusion.....	9
<b>Chapter 3: Finite strain-evolution and visualization in single and double layer systems.....</b>	<b>11</b>
3.1. Introduction.....	11
3.2. Exact finite strain ellipse.....	11
3.3. Coloring of the finite strain ellipse.....	13
3.4. Finite strain in single layer folds.....	14
3.4.1. Finite strain-evolution during progressive folding.....	14
3.4.2. Finite and incremental strain distribution, the neutral line.....	20
3.5. Finite strain in double layer folds.....	23
3.5.1. Three phases of progressive deformation.....	24
3.5.2. Three regions of deformation in the matrix between the stiff layers.....	32
<b>Chapter 4: Asymmetric parasitic fold development in multilayer systems.....</b>	<b>36</b>
4.1. Introduction.....	36
4.2. Influence of the amplitude of the initial perturbation.....	37
4.3. Number of layers in the multilayer stack.....	41

<b>Chapter 5: Discussion.....</b>	<b>45</b>
5.1. Conditions for the occurrence of asymmetric parasitic folds.....	45
5.2. Model assumptions compared with a natural example.....	49
<b>Chapter 6: Conclusions and prospects.....</b>	<b>51</b>
6.1. Conclusions.....	51
6.2. Prospects.....	52
<b>Acknowledgments.....</b>	<b>53</b>
<b>References.....</b>	<b>54</b>
<b>Appendix A: Mechanical equations and their discretization with the finite element method.....</b>	<b>55</b>
A1. Derivation of the governing equations.....	55
A2. Incompressibility with the finite element method.....	56
A3. Discretization of equation (A20).....	57
A4. Discretization of equation (A21).....	61
A5. Derivation of the final equation system.....	62
A6. Incompressibility with the Uzawa algorithm.....	63
<b>Appendix B: Numerical integration and the use of local elements.....</b>	<b>65</b>
B1. Gauss-Legendre quadrature.....	65
B2. The Q9/3 element.....	68
<b>Appendix C: Flowchart of the finite element code.....</b>	<b>71</b>
<b>Appendix D: Dimensionless formulation.....</b>	<b>72</b>
<b>Appendix E: Strain distribution in single layer folds with different viscosity contrasts.....</b>	<b>74</b>

## Chapter 1

# Introduction

The investigation of folded rocks from a theoretical point of view has a very long history and many authors together published an extensive assemblage of literature on this topic. Early works (e.g. Biot, 1961) simplified the problem of a single layer fold and tried to find analytical solutions for different aspects of folded layers, for example the growth rate or the dominant wavelength. Even though the simplifications were significant, the obtained results already were very insightful and they remain fundamental knowledge for the present-day studies. Later workers (e.g. Fletcher, 1977) developed more sophisticated and exact models to describe the same aspects of single layer folds. With increasing knowledge of the processes involved in folding of rocks the theories were extended to the more general and near-natural case of multilayer folds. Analytical results were searched and found for this scenario (e.g. Smith and Marshall, 1993). In the upcoming computer simulations different rheologies, geometries and boundary conditions were implemented and it was possible to observe the fold development dynamically (e.g. Williams, 1980). In order to numerically model multilayer folds, many authors use special constraints that allow resolving only one layer of a multilayer sequence and repeat this layer (e.g. Casey and Butler, 2004). With such an approach calculation time is strongly reduced. The increasing available computational power now allows a higher resolution, hence more accuracy in the models. At the same time, more complex rheologies and more and more interactive processes are involved in such models. The increase of resolution makes the modeling of real multilayer systems possible where a whole stack of layers is resolved and no further constraints are necessary (e.g. Schmid and Podladchikov, 2005). The increase in complexity also leads to new insights in geometrically relatively simple systems such as single layer folds (e.g. Schmalholz et al., 2005).

Compared to analogue models the numerical models have the big advantage that properties within the models such as stress or pressure can be quantified at every point and for each and every every time step. This thesis goes in the line of works which use rheologically and geometrically simple models with a high enough resolution to model a real multilayer stack. In contrast to models where only one layer of a multilayer system is considered, this model also allows vertical variations between the individual layers to occur.

Many numerical models have deficits in the calculation and especially in the visual representation of the finite strain which accumulates over time. In contrast, the treatment of the incremental strain causes no big problems. For geologists, however, the finite strain is much more important since it is observable in the field. A common visualization tool for finite deformation is the concept of the strain ellipsoid, which is represented with an ellipse in two-dimensions. Field geologists and analogue modelers use this tool for a long time. Although this concept is well known it is rarely used in numerical models. Therefore, the calculation of finite strain ellipses is carried out as a first aim of this thesis. This visualization technique allows the investigation of the finite strain distribution of single layer and double layer folds as a second aim.

Once double layer systems are analyzed, multilayer stacks can be added to the system as the third aim of this thesis. This multilayer stack is situated between two thicker layers of a double layer system which folds with a different dominant wavelength and a different growth rate. The used rheology is linear viscous for the stiff layers, as well as for the matrix in between. The model has a free slip lower surface and an open surface at the top and it is horizontally compressed with a constant strain rate. With this relatively simple model asymmetric parasitic folds with a different wavelength than the thicker layers are produced, which makes the model fully multi scale. The conclusions from the double layer fold systems can be used to determine under which conditions parasitic folds develop.

Development and programming of the finite element code and all the visualization routines in MATLAB® are done by myself. The visualization is kept apart from the finite element code and both are written as general as possible for future use. This is important especially for the visualization routine, since it may be used by other researchers or for different projects. Development of the own finite element code and understanding of the mechanical equations behind was the main aim of this diploma thesis.

## Chapter 2

# Methods

### 2.1. Introduction

This chapter summarizes the basic principles and methods used to write the two dimensional finite element code. A much more detailed description is given in the appendices A, B and C. Since a standard finite element method is used, many of the techniques used here are also described in different text books and papers (e.g. Thomasset, 1981, Zienkiewicz and Taylor, 1994 or Hughes et al., 1979). The computer code itself is written in MATLAB<sup>®</sup> Version 6.5 by The MathWorks Inc. and was run on personal computers. No special computer setup or super computers were used. Visualization was also done with MATLAB<sup>®</sup> graphic tools.

### 2.2. Finite element formulation of the mechanical equations

The two-dimensional displacement field of an incompressible linear viscous fluid can be calculated by combining the following four sets of equations. Note that compressive stresses are defined as negative and that gravity is ignored in the first equation.

$$1) \text{ Force balance: } \mathbf{B}^T \vec{\sigma} = 0 \quad (1)$$

$$2) \text{ Conservation of mass: } \nabla^T \cdot \vec{v} = 0 \quad (2)$$

$$3) \text{ Rheological relation } \vec{\sigma} = -p\vec{m} + \tilde{\mathbf{D}}\vec{\epsilon}' \quad (3)$$

$$4) \text{ Kinematic equation } \vec{\epsilon} = \mathbf{B}\vec{v} \quad (4)$$

where  $\nabla$  is the Nabla operator,  $\vec{v}$  the velocity vector and  $p$  the pressure.  $\vec{\sigma}$  and  $\vec{\epsilon}$  are vectors containing the total stress and total strain rate values, respectively. The vector  $\vec{\epsilon}'$  contains the deviatoric strain rates.

The first and second entry are the normal components in x- and y-directions, while the third entry is the shear component. The third entry in the strain rate vector is defined as  $\dot{\gamma}_{xy} = 2\dot{\epsilon}_{xy}$ . The matrices  $\mathbf{B}$  and  $\tilde{\mathbf{D}}$  and the vector  $\vec{m}$  are defined as follows.

$$\mathbf{B} = \begin{bmatrix} \partial/\partial x & 0 \\ 0 & \partial/\partial y \\ \partial/\partial y & \partial/\partial x \end{bmatrix}, \quad \tilde{\mathbf{D}} = \begin{bmatrix} 2\mu & 0 & 0 \\ 0 & 2\mu & 0 \\ 0 & 0 & \mu \end{bmatrix}, \quad \vec{m} = \begin{Bmatrix} 1 \\ 1 \\ 0 \end{Bmatrix} \quad (5)$$

where  $\mu$  is the viscosity. With the definition of deviatoric strain rates, equation (3) can be reformulated. Thereby formulation of equation (3) does not change, only the definition of matrix  $\tilde{\mathbf{D}}$  has to be adjusted to  $\mathbf{D}$ .

$$\mathbf{D} = \begin{bmatrix} 4/3\mu & -2/3\mu & 0 \\ -2/3\mu & 4/3\mu & 0 \\ 0 & 0 & \mu \end{bmatrix} \quad (6)$$

Combination of equations (1) to (4) leads to the governing equations that describe the incompressible Newtonian flow with a mixed formulation.

$$\mathbf{B}^T \mathbf{D} \mathbf{B} \vec{v} - \nabla p = 0 \quad (7)$$

$$\nabla^T \cdot \vec{v} = 0 \quad (2)$$

Note that equation (7) is a set of two equations making equations (7) and (2) together a set of three equations for the three unknowns  $v_x$ ,  $v_y$  and  $p$ . Incompressibility implied in equation (2) holds major problems for solving the system and especially for generating an accurate pressure field. These problems are well summarized in Pelletier et al., 1989. Therefore, a compressible formulation has to be chosen while the Uzawa iteration will approximate the incompressibility. The more general compressible formulation of equations (2) is:

$$\frac{\partial p}{\partial t} = -K (\nabla^T \cdot \vec{v}) \quad (8)$$

where  $K$  is the incompressibility.

The formulation of equation (8) is often referred to as the penalty approach with the penalty parameter  $K$  (see e.g. Hughes, 2000, Chapter 4). This penalty parameter essentially is the elastic incompressibility parameter, which is to be chosen a big number for an incompressible formulation.

With the compressible formulation and the penalty approach the resulting governing equations are:

$$\mathbf{B}^T \mathbf{D} \mathbf{B} \vec{v} - \nabla p = 0 \quad (9)$$

$$\frac{\partial p}{\partial t} = -K (\nabla^T \cdot \vec{v}) \quad (10)$$

Before the spatial derivatives are considered, the time derivative in equation (10) is discretized with a finite difference approach.

$$p^{new} + K \Delta t (\nabla^T \cdot \vec{v}) = p^{old} \quad (11)$$

where  $\Delta t$  is a small time increment, and  $p^{old}$  and  $p^{new}$  is the pressure before and after the time increment. Discretization of equations (9) and (11) is carried out with a finite element method by approximating the velocity and the pressure within an element with their corresponding shape functions  $N_v$  and  $N_p$ , respectively. Integration over the whole element is performed after the Galerkin weighting functions (same functions as the shape functions) are applied to the equations. Integrating by parts reduces the system to a set of equations containing only first order derivatives which is often referred to as the weak formulation. This system has the following popular form (see e.g. Hughes, 2000, Equation 4.3.21 or Zienkiewicz and Taylor, 1994, Equation 12.18)

$$\begin{bmatrix} \mathbf{KM} & \mathbf{G} \\ -K \Delta t \mathbf{G}^T & \mathbf{M} \end{bmatrix} \begin{Bmatrix} \vec{v} \\ p^{new} \end{Bmatrix} = \begin{Bmatrix} 0 \\ \mathbf{M} p^{old} \end{Bmatrix} \quad (12)$$

In this mixed formulation,  $\mathbf{G}$  is the discrete gradient operator and  $\mathbf{G}^T$  is the discrete divergence operator.  $\vec{v}$  is the velocity vector containing all velocity components of all nodes of the element. The following definitions apply in equation (12).

$$\mathbf{KM} = \iint \tilde{\mathbf{B}}^T \mathbf{D} \tilde{\mathbf{B}} dx dy \quad , \quad \mathbf{G} = -\iint \tilde{\mathbf{B}}_G^T N_p dx dy \quad , \quad \mathbf{M} = \iint N_p^T N_p dx dy \quad (13)$$

where  $\tilde{\mathbf{B}}$  and  $\tilde{\mathbf{B}}_G$  are suitable organized matrices containing the spatial derivatives of the velocity shape functions.

The three equations (12) can be collapsed into two equations eliminating one degree of freedom,  $\overrightarrow{p^{new}}$  out of the system.

$$\mathbf{KL} \vec{v} = -\mathbf{G} \overrightarrow{p^{old}} \quad (14)$$

The lost degree of freedom,  $\overrightarrow{p^{new}}$  will be calculated later in the Uzawa iteration loop.

$\vec{p}^{old}$  must be predefined before solving the equation while the new matrix  $\mathbf{KL}$  is defined as

$$\mathbf{KL} = \mathbf{KM} + K \Delta t \mathbf{G} \mathbf{M}^{-1} \mathbf{G}^T \quad (15)$$

### 2.3. The use of the Uzawa iteration algorithm

Equations (9) and (11) are compressible formulations. To achieve incompressibility Pelletier et al., 1989 recommend the Uzawa iteration algorithm below as one of the best possibilities.

- 1) Choose  $\vec{p}^{old}$  as an arbitrary initial pressure. Very convenient is a zero value.
- 2) Let  $n$  be the iteration number. Derive  $\vec{v}$  with equation (14) for  $n \geq 1$ .
- 3) Calculate  $\vec{p}^{new}$  with equation (12) and use it as  $\vec{p}^{old}$  in the next iteration step.
- 4) Repeat step 2) and 3) until the divergence of the velocity field (equation (2)) is small enough (smaller than a certain exit criteria).

Besides the velocity field, the pressure field is a result of the Uzawa iteration. This pressure field was eliminated out of the governing equation before and is now regained. The penalty parameter  $K$  in equation (8) has to be chosen wisely in order to optimize the Uzawa algorithm. Though a high number reduces the iteration steps for the divergence to reach the exit criteria, it also reduces the accuracy of the matrix division necessary to solve equation (14).

### 2.4. Numerical integration on the Q9/3 element

In this study the so called Q9/3 elements are used, which are quadrilateral and built up of nine nodes for the velocity degrees of freedom, three for the pressure degrees of freedom and nine integration points. The corresponding shape functions for the velocity are bi-quadratic and continuous over the element boundaries. Shape functions for the pressure are bi-linear and discontinuous. This type of element is iso-parametric and is generally considered as one of the best elements for fluid flow problems (e.g. Hughes, 2000). The choice of discontinuous pressure shape functions allows calculating accurate pressure fields although the pressure is eliminated out of the equation system, which is actually solved. The numerical integration on this element is carried out using the Gauss-Legendre quadrature with its fundamental formula

$$\int_{-1}^1 \int_{-1}^1 f(\xi, \eta) d\xi d\eta \simeq \sum_{i=1}^{nx} \sum_{j=1}^{ny} f(\xi_i, \eta_j) w_i w_j = \sum_{n=1}^{nip} f(\xi_n, \eta_n) w_n \quad (16)$$

where  $f(\xi, \eta)$  is an arbitrary function in the local coordinate system  $(\xi, \eta)$ ,  $nip = nx \cdot ny$  is the total number of integration points within one element and  $w_n = w_i \cdot w_j$  is the weight of the  $n$ -th integration point.

In order to apply this formula, equations (13) have to be transformed from global to local coordinates using the determinant of the Jacobian.

Before doing this, the shape function derivatives which, for practical reasons, are defined in local coordinates have to be transformed to global coordinates using the Jacobian matrix. This needs to be done because equation (13) is given in terms of global coordinates. These coordinate-mapping steps, as well as the summation over all integration points in equation (16), is performed for every element within a loop over the integration points.

## 2.5. Normalization and boundary conditions

To avoid ill-conditioned matrices in the finite element code, all physical parameters are normalized using the characteristic value of one for the three fundamental quantities distance, time and viscosity, respectively. This normalization leads to a dimensionless formulation. To get physical values, the normalization has to be removed. It is described in further detail in Appendix D.

The boundary conditions used for the experiments on single layer, double layer and multilayer systems are given in table 1. Using these boundary conditions, it is possible to model only one half of a wavelength and mirror it to get a full wavelength (figure 1). Further conditions like the time increment, the initial perturbation of the layers or the resolution is given in the corresponding chapters.

<i>Boundary</i>	<i>Boundary condition</i>	<i>Values specified at the boundary</i>
<i>Top</i>	<i>Free surface</i>	<i>Nothing</i>
<i>Bottom</i>	<i>Free slip</i>	$v_y = 0$
<i>Left</i>	<i>Free slip</i>	$v_x = 0$
<i>Right</i>	<i>Constant strain rate</i>	$v_x = x \cdot \dot{\epsilon}_x$ , whereas $\dot{\epsilon}_x = 1$

**Table 1:** Boundary conditions used in the experiments on single layer, double layer and multilayer systems.

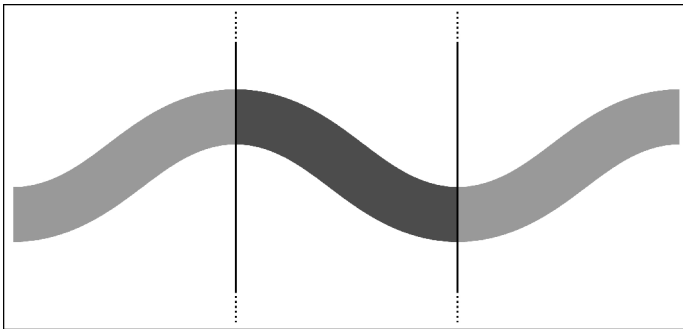


**Fig. 1:** The modeled area of a fold is restricted to a half wavelength and the matrix above and below this half wavelength.

## 2.6. Benchmarks

Before using the finite element code to model folds, it was tested with two different types of benchmarks. The general idea of these benchmarks is to approximate an analytical solution with the computer code and to see whether the numerical solution converges towards the analytical with increasing resolution. In both tests the exit criteria for the velocity divergence in the Uzawa algorithm is set to  $10^{-12}$  and the time increment to  $10^{-8}$ .

### 2.6.1. Single layer fold growth rate

Fletcher, 1977 provides the following exact solution for the growth rate  $q$  of a single layer fold with higher viscosity than the surrounding media. The rheology used in his paper is linear viscous for all materials and therefore is the same as that in this study.

$$q_{analytic}(k; R) = \frac{-2(1-R)}{(1-R^2) - \frac{1}{2k}((1+R)^2 e^k - (1-R)^2 e^{-k})} \quad (17)$$

where  $k = 2\pi H/L$  is the wave number with  $H$  as the layer thickness,  $L$  as the wavelength and  $R = \mu_{matrix} / \mu_{layer}$  as the viscosity contrast between the surrounding matrix and the layer.

The growth rate defines how fast a fold amplifies according to the amplification law (Biot, 1961):

$$A(t) = A_0 e^{(1+qt)} \quad (18)$$

The analytical fold growth rate  $q_{analytical}$  is evaluated for a wavelength to thickness ratio  $L/H$  of 16.5 and a viscosity contrast  $R$  of  $10^{-2}$ . For the same values, three time steps are performed with the finite element code. The initial amplitude to thickness ratio of the layer  $A_0/H$  is set to  $10^{-4}$ . The fold growth rate is calculated according to:

$$q_{numeric} = \frac{1}{dt} \log_{10} \left( \frac{A_3}{A_2} \right) - 1 \quad (19)$$

where  $dt$  is the time increment and  $A_3$  and  $A_2$  are the amplitudes after 3 and 2 time steps.

In figure 2 the error between the analytical and the numerical fold growth rate clearly decreases with increasing resolution in the finite element code. Figure 3 shows the converging numerical results for the fold growth rate with increasing resolution.

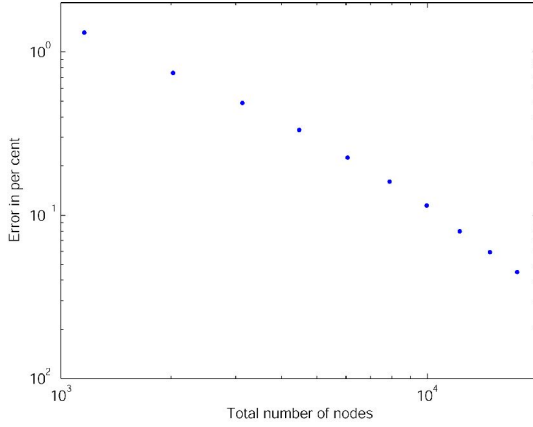


**Fig. 2:** Double logarithmic plot of the error of the numerical fold growth rate with respect to the analytical solution by Fletcher, 1977 vs. the total number of nodes used in the finite element code. The numerical solution clearly converges towards the analytical solution with increasing resolution. Geometrical and numerical details are described in the text.

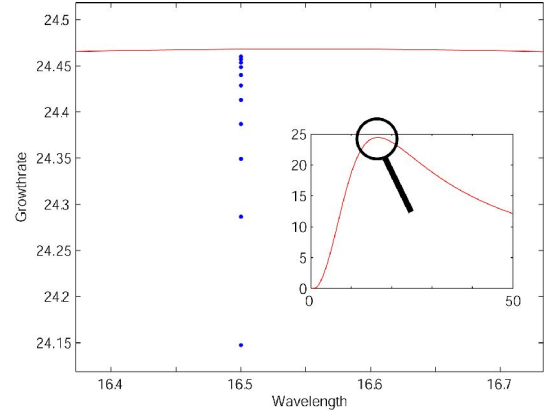


**Fig. 3:** Zoom to the growth rate vs. wavelength curve (inlay) at a wavelength to thickness ratio of 16.5. The blue dots (numerically calculated growth rate) converge towards the analytical growth rate (red line) with increasing resolution of the finite element code.

### 2.6.2. Pressure field around a rigid inclusion

Schmid, 2005 provides a fully two dimensional analytical solution for the pressure  $p$  at any point around a rigid inclusion surrounded by a linear viscous media compressed in pure shear conditions.

$$p = -4\mu\dot{\epsilon}\Re\left(\frac{\xi^2(2me^{-2i\phi} - 2e^{2i\phi})}{(1-m^2)(3m\xi^4-1)}\right) \quad (20)$$

where  $\mu$  is the viscosity of the matrix around the inclusion and  $\dot{\epsilon}$  the far-field pure shear strain rate.  $\Re$  denotes the real part of the expression in brackets.  $\zeta$  is the complex coordinate in the image plane which is mapped to the physical plane. The variable  $m$  for a perfectly circular inclusion is equal to zero and  $\phi$  defines the inclination of the inclusion with respect to the far-field flow which is indistinguishable for the case of a circular object. For further details see Schmid, 2005.

In the finite element program the pressure is one of the outputs of the Uzawa iteration loop described in chapter 2.3. This numerically calculated pressure field is compared with the analytical solution at every integration point after one time step. The far-field pure shear strain rate  $\dot{\epsilon}$  is equal to 0.5 and the viscosity in the surrounding matrix is 100 (dimensionless).

In figure 4 the error averaged over the whole numerical domain is plotted versus the resolution of the finite element code. It is obvious that the error decreases with increasing resolution. Figure 5 shows the difference between the numerical and the analytical pressure field calculated with the highest resolution of figure 4 which is 50904 nodes, whereas some of them lie outside the plotted domain.

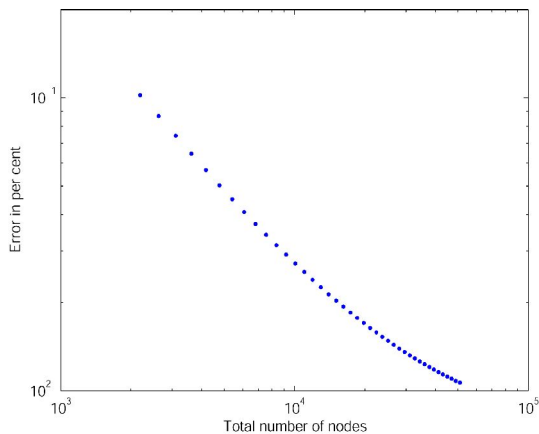


**Fig. 4:** Double logarithmic plot of the averaged error of the numerical pressure field with respect to the analytical solution by Schmid, 2005 vs. the total number of nodes used in the finite element code. The numerical solution clearly converges towards the analytical solution with increasing resolution. The spatial distribution of the error at the highest resolution is presented in figure 5.

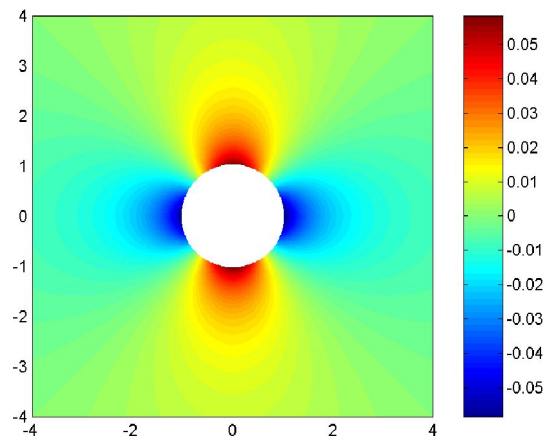


**Fig. 5:** Spatial distribution of the error of the numerical pressure field with respect to the analytical around a perfectly circular rigid inclusion. In the directions of the far-field strain axes and at the very boundary of the inclusion the error reaches the highest values. 50904 nodes are used for the numerical solution.

Both benchmarks, fold growth rate and pressure field around a rigid inclusion, clearly show a convergence of the numerical towards the analytical solution with increasing resolution of the numerical simulation. In both cases this converging trend is continuous. This demonstrates the accuracy of the finite element code used in this study.

## Chapter 3

# Finite strain-evolution and visualization in single and double layer systems

### 3.1. Introduction

In nearly all papers or text books on structural geology the two-dimensional finite strain in rocks is described by an ellipse (e.g. Ramsay and Huber, 1989). It is assumed that before the deformation, this ellipse was a circle that deformed passively. Although this concept is long-established, most authors still draw strain ellipses by hand and do not calculate them. This chapter now presents a new visualization technique that calculates the finite strain ellipse at any point in the material.

### 3.2. Exact finite strain ellipse

For every time step the incremental velocity gradient tensor can be calculated at any integration point according to

$$\left. \frac{\partial v_i}{\partial x_j} \right|_{\text{integration point}} = \tilde{\mathbf{B}}_{\text{velgrad}} \vec{v} \quad (21)$$

where  $\tilde{\mathbf{B}}_{\text{velgrad}}$  is a suitable organized matrix containing the spatial derivatives of the velocity shape functions at the integration point.

Assuming homogeneous strain around the integration point the velocity gradient tensor can be used to calculate the coordinates of an arbitrary point  $P$  after the deformation increment  $(x',y')$ , knowing the coordinates before the deformation  $(x,y)$ . The interlinking tensor is called the incremental deformation gradient tensor  $\mathbf{DG}_i$ .

$$\begin{Bmatrix} x' \\ y' \end{Bmatrix}_P = \underbrace{\left( \delta_{ij} + \Delta t \frac{\partial v_i}{\partial x_j} \right)}_{\mathbf{DG}_i} \begin{Bmatrix} x \\ y \end{Bmatrix}_P = \underbrace{\left( \delta_{ij} + \frac{\partial u_i}{\partial x_j} \right)}_{\mathbf{DG}_i} \begin{Bmatrix} x \\ y \end{Bmatrix}_P \quad (22)$$

where  $u_x$  and  $u_y$  are the incremental displacement components in x- and y-direction, respectively and  $\delta_{ij}$  is the Kronecker delta. After a second deformation increment the coordinates of the same point  $P$  are

$$\begin{Bmatrix} x'' \\ y'' \end{Bmatrix}_P = \mathbf{DG}_{i2} \begin{Bmatrix} x' \\ y' \end{Bmatrix}_P = \mathbf{DG}_{i2} \mathbf{DG}_{i1} \begin{Bmatrix} x \\ y \end{Bmatrix}_P \quad (23)$$

This way the coordinates of the point  $P$  after any number of deformation increments can be directly calculated, provided that initial coordinates are known. The multiplication of all incremental deformation gradient tensors leads to the finite deformation gradient tensor  $\mathbf{DG}_f$ . Point  $P$  may be an arbitrary point on a circle around the integration point. Assuming homogeneous deformation around the integration point during all deformation steps, the coordinates of this passively deformed circle can also be calculated directly. This process is illustrated in figure 6.

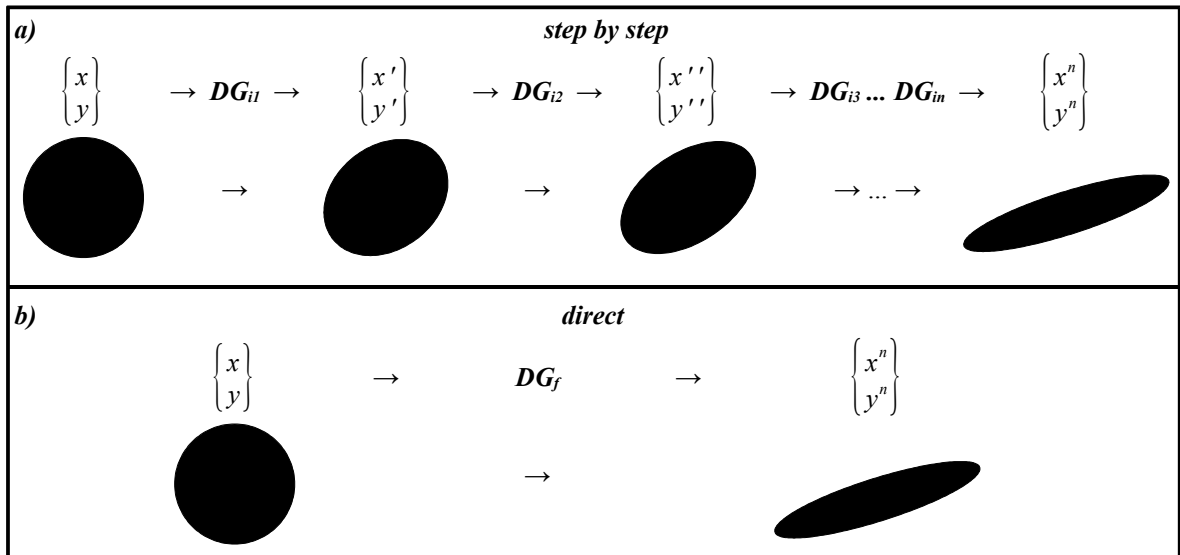


**Fig. 6:** **a)** Progressive deformation of a strain ellipse which initially was a circle. To calculate the coordinates of the ellipse after any deformation increment equation (22) is applied to the coordinates of the ellipse before the increment. **b)** Direct calculation of the coordinates of the finite strain ellipse using equation (23). The finite deformation gradient tensor  $\mathbf{DG}_f$  has to be calculated stepwise beforehand.

The finite deformation gradient tensor is calculated for every integration point within the numerical domain and is updated during every time step. It can be averaged over an area or interpolated to every point, like every other quantity. Therefore the finite strain ellipses can be drawn everywhere and in every size using a size factor. However, in general, a strain ellipse with a finite size always overlaps an area which has been heterogeneously deformed and it only represents the stepwise homogeneous strain at its very center. Making the finite strain ellipse bigger only means making it visible.

### 3.3. Coloring of the finite strain ellipse

In natural deformation processes, it is possible that a circle is compressed before being extended in the same direction. The resulting finite strain ellipse is again a circle and the experienced deformation is invisible. The same happens if deformation consists of rotation only. Two possibilities are presented here to avoid this problem and to distinguish between undeformed circles and deformed circular finite strain ellipses.

The incremental displacement gradient tensor can be split into two parts, the incremental strain tensor  $\epsilon$  and the incremental rotation tensor  $\omega$ .

$$\frac{\partial u_i}{\partial x_j} = \underbrace{\frac{1}{2} \left( \frac{\partial u_i}{\partial x_j} + \frac{\partial u_j}{\partial x_i} \right)}_{\epsilon} + \underbrace{\frac{1}{2} \left( \frac{\partial u_i}{\partial x_j} - \frac{\partial u_j}{\partial x_i} \right)}_{\omega} \quad (24)$$

The incremental strain tensor  $\epsilon$  is symmetric and the incremental rotation tensor  $\omega$  antisymmetric. These two tensors can be used to define two scalar quantities:

$$\text{incremental von Mises equivalent strain:} \quad \epsilon_{eqv} = \sqrt{\frac{2}{3} (\epsilon_{xx}^2 + \epsilon_{yy}^2 + 2\epsilon_{xy}^2)} \quad (25)$$

$$\text{incremental rotation angle:} \quad \alpha = \arctan(\omega_{yx}) \quad (26)$$

The sense of rotation is defined positive counterclockwise. Therefore  $\omega_{yx}$  is used in equation (26) instead of  $\omega_{xy}$ . The von Mises equivalent strain is a measure for the change of shape and is always positive. Both quantities are scalar and can be summed up over all deformation steps, leading to a value for the shape change history and the total rotation angle, respectively. The summation of the absolute values of the incremental rotation angle leads to a value for the rotation history. The described values can be used to color the finite strain ellipses.

### 3.4. Finite strain in single layer folds

The geometrical and numerical setup for the experiments described in this section are summarized in table 2. Normalization rules are given in chapter 2.5.

<i>Setup for experiments on single layer folds</i>			
<i>Viscosity of the layer</i>	$\mu_l = 100$		
<i>Viscosity of the matrix</i>	$\mu_m = 1$		
<i>Initial layer thickness</i>	$H_0 = 5$		
<i>Type of initial perturbation</i>	<i>Half cosine. Same perturbation for upper and lower interface of layer</i>		
<i>Amplitude of initial perturbation</i>	$\frac{A_0}{H_0} = \frac{1}{100}$		
<i>Initial thickness of matrix above and below layer</i>	$H_{m0} = 15$		
<i>Width of domain</i>	$L_x = 40$ ( <i>half wavelength for a viscosity contrast of 100</i> )		
<i>Time increment</i>	$\Delta t = 10^3$		
<i>Horizontal resolution</i>	301 nodes		
<i>Vertical resolution over layer</i>	31 nodes	<i>Total vertical</i>	Total resolution 27391 nodes
<i>Vertical resolution over matrix</i>	31 nodes	91 nodes	

**Table 2:** Fundamental definitions for the experiments on single layer folds.

#### 3.4.1. Finite strain-evolution during progressive folding

With the new visualization technique one may readily observe the strain-evolution in a fold (figures 7a-h). The color of the finite strain ellipses depends on the accumulated von Mises equivalent strain  $\Sigma \varepsilon_{eqv}$  in the upper pictures and the finite rotation angle  $\Sigma \alpha$  in the lower ones, respectively. The reference colors are given in the two color-bars on every page. Note that only one half of the pictures is calculated and then mirrored to get a better view of the situation. Therefore the finite rotation angles on the left-hand side of the pictures 7b, d, f and h have the wrong sense of rotation. After 10% shortening (figures 7a and b) almost no buckling occurred. Only a very slight undulation of the layer is visible. The strain ellipses show a vertical major strain axis over the whole domain due to the far-field shortening. No visible difference between individual strain ellipses, neither in shape nor in color, expresses homogeneous strain. The layer and the matrix are indistinguishable in terms of strain and rotation. After 25% shortening (figures 7c and d) the buckling process started. The fold limbs are rotated and so is the near-layer matrix, but with opposite sense. While rotation in the fold limbs is due to rigid body rotation (greenish color in figure 7d), rotation in the matrix is due to shearing (red to orange color in figure 7d). This tendency is even stronger after 40% shortening (figures 7e and f).

While rigid body rotation is dominant in the stiff layer, strain is dominant in the matrix (darker blue colors in the stiff layer, yellow to green in the matrix in figure 7e). Besides the region near the outer arc of the fold, the matrix is more distorted than the layer and therefore has more elongated strain ellipses. Near the outer arc, the push of the growing fold and the overall compression are opposed, though far-field compression is stronger (vertical major strain axes). Near the inner arc, the pull of the growing fold and far-field compression work together and the ellipses are more elongated. At 50% shortening (figures 7g and h) fold limbs are not much distorted but strongly rotated. The opposite takes place in the matrix near the fold limbs. The strain ellipses are heavily distorted (dark red in figure 7g) but rotated only by a few degrees. The strong rotation of these ellipses is almost entirely due to high shear strain. Generally, the accumulated strain from the first 10% of shortening does not change much during further deformation. In the matrix it is the rigid body rotation that little changes.

To get a better understanding of the evolution of the finite strain in figure 7 it is also possible to pick single vertical beams out of the simulation. This is done in figure 8 with two vertical beams within the stiff layer, one in the hinge zone and one on the fold limb. The beams are chosen in a way that their subdivisions are quadratic at the initial stage. While the beam at the hinge does not rotate, the one on the fold limb obviously rotates with increasing shortening. The accumulated strain shows a different pattern. In the limb, the beam rotates with increasing shortening but finite strain is about the same over the whole beam. In the first 25% of shortening the accumulated strain changes much more than from 25% to 50%. On the contrary the accumulated strain in the hinge-beam varies strongly from top to bottom. There the bending of the layer influences the strain distribution.

**Fig. 7 (pages 16 to 19):** Growing single layer fold with a viscosity contrast of 100 at different stages of far-field shortening. Strain ellipses in the upper pictures are colored with von Mises equivalent strain. The corresponding color-bars are given on every page. The ones at the bottom are colored with finite rotation angle. a) and b) 10% shortening, c) and d) 25% shortening, e) and f) 40% shortening, g and h) 50% shortening. For more information see text.

10% shortening

figure 7a)

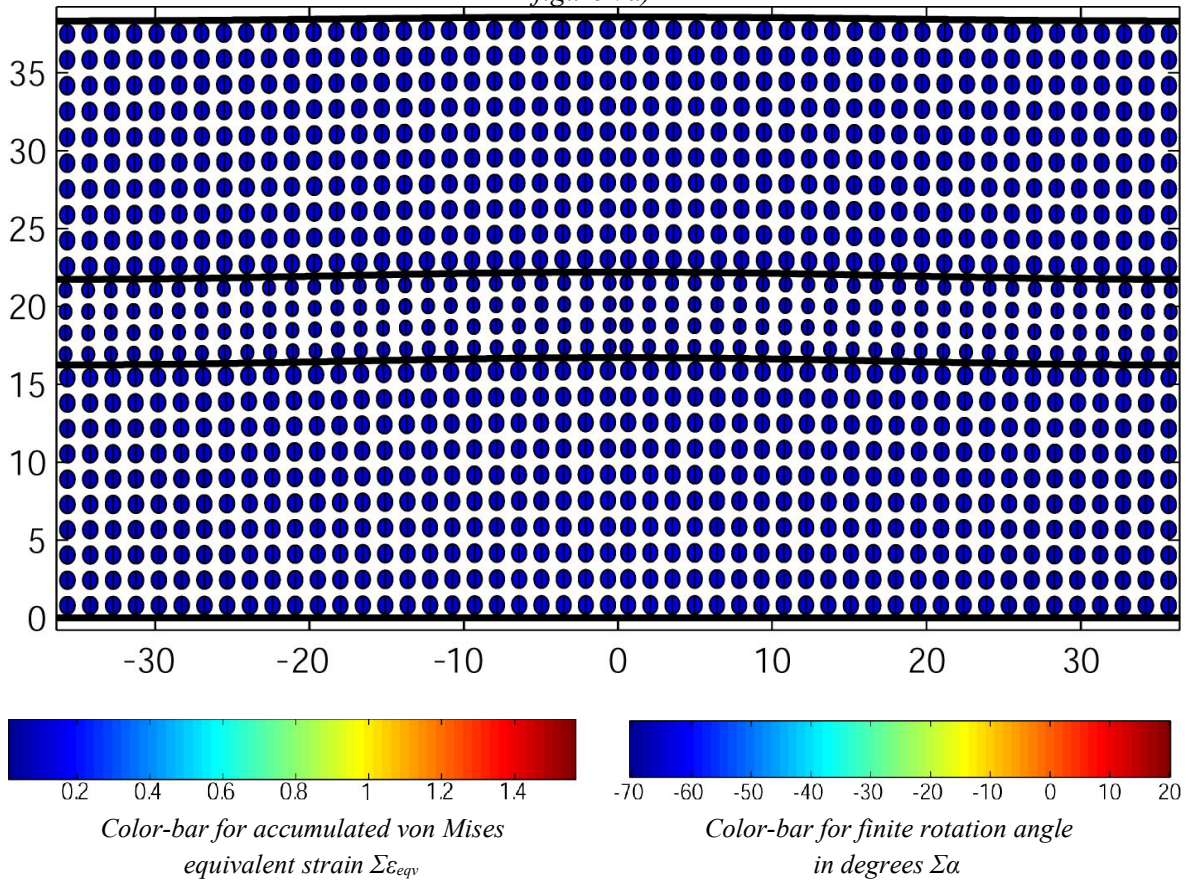
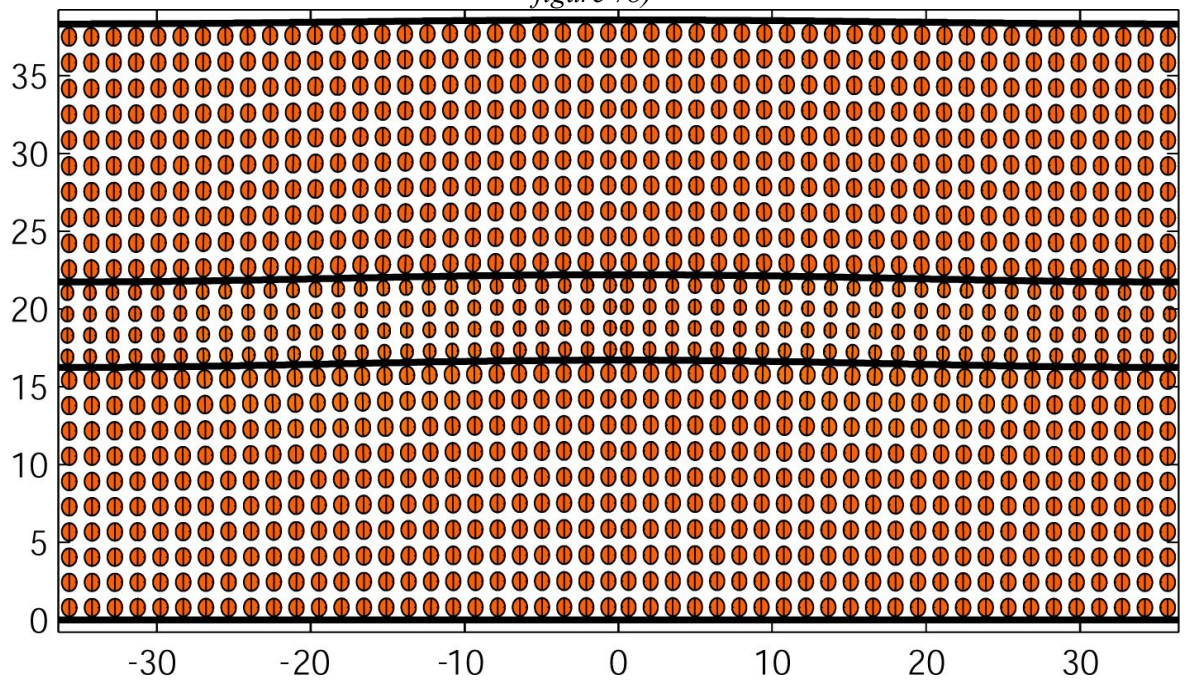
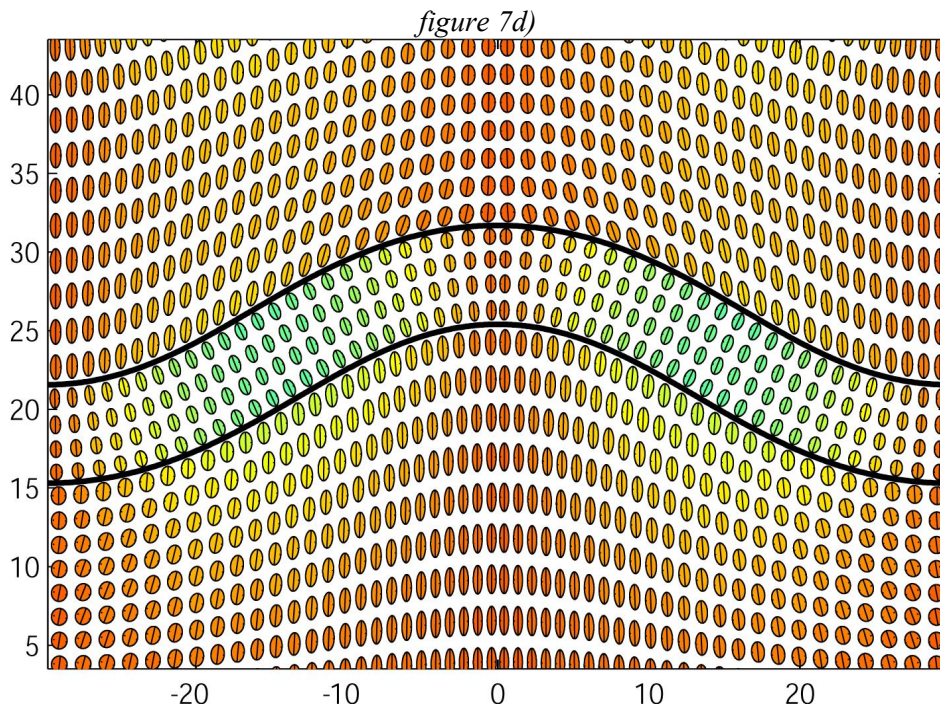
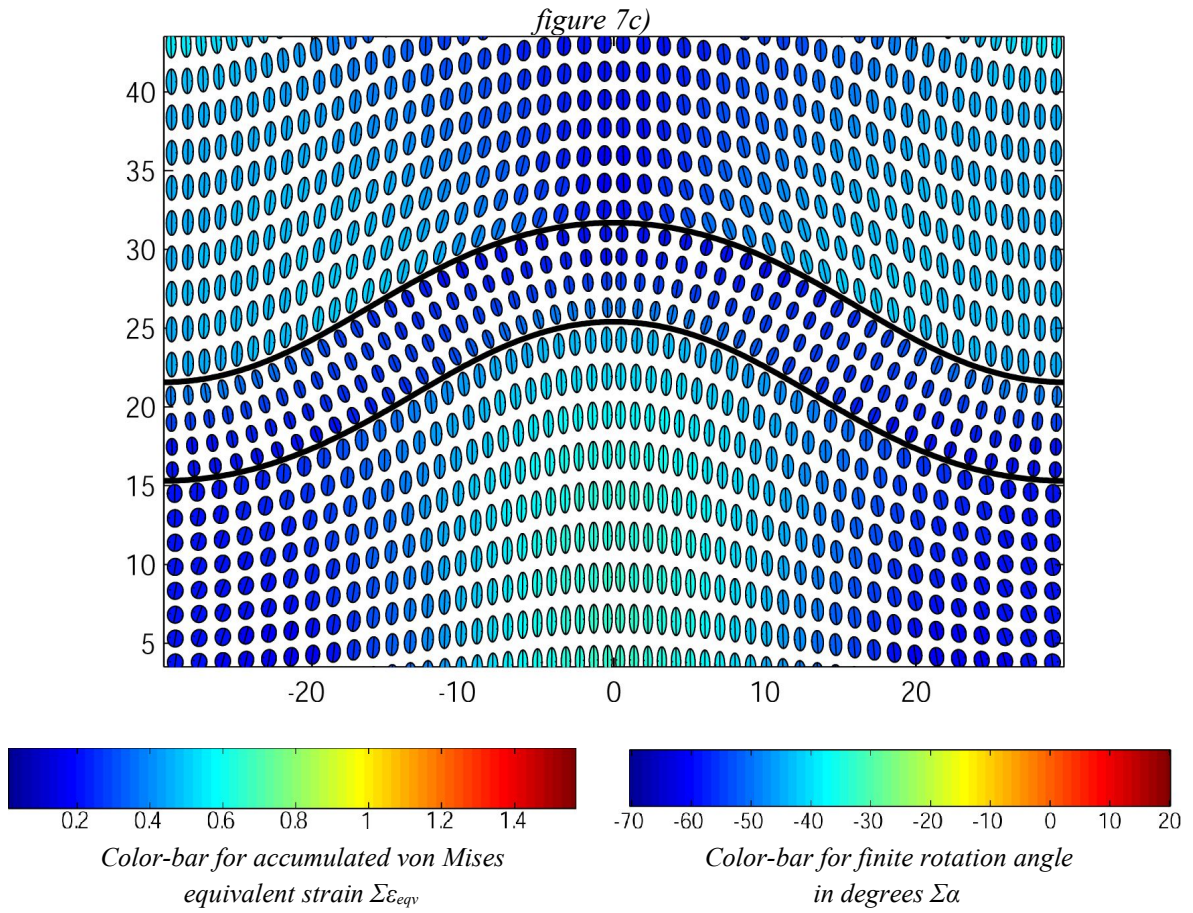


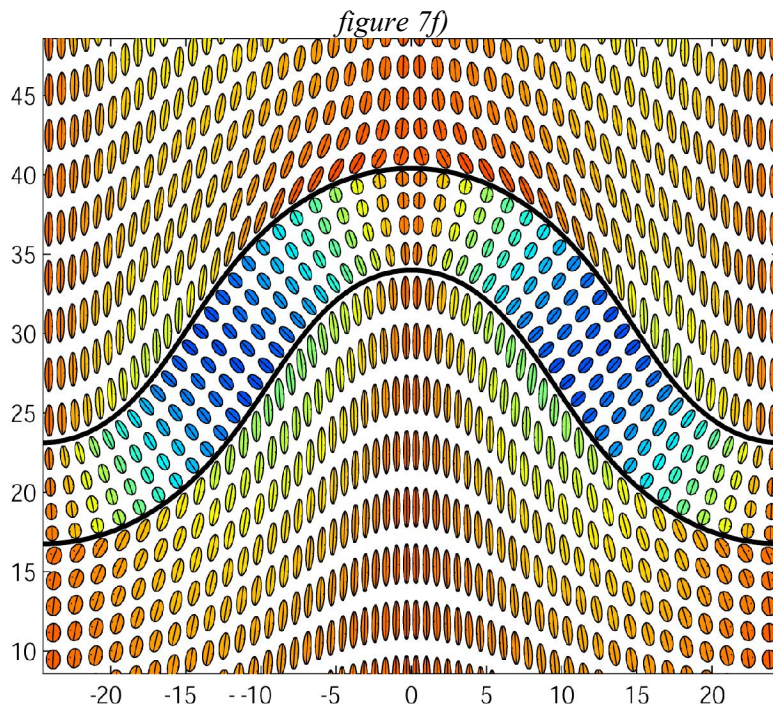
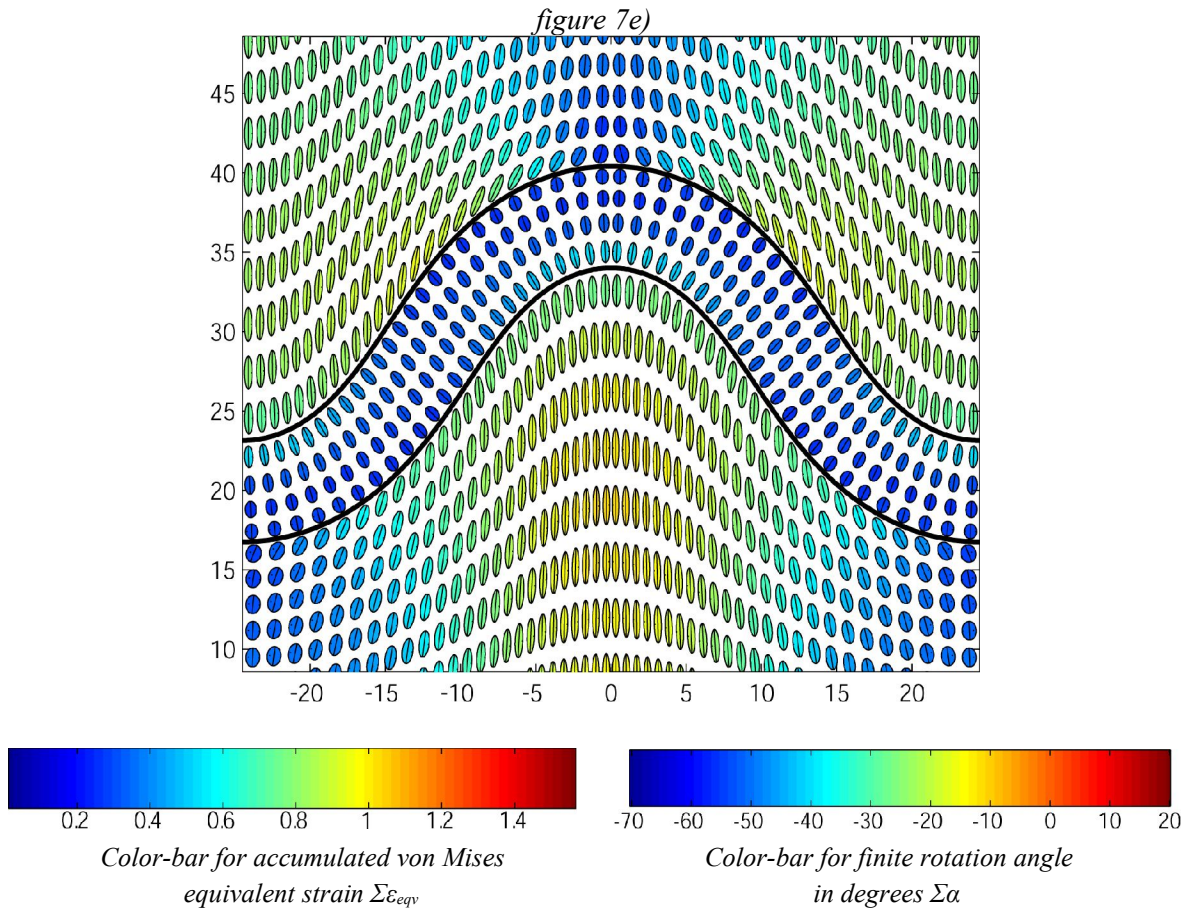
figure 7b)



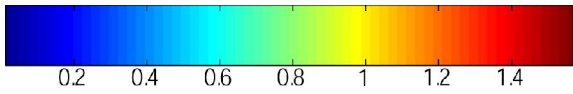
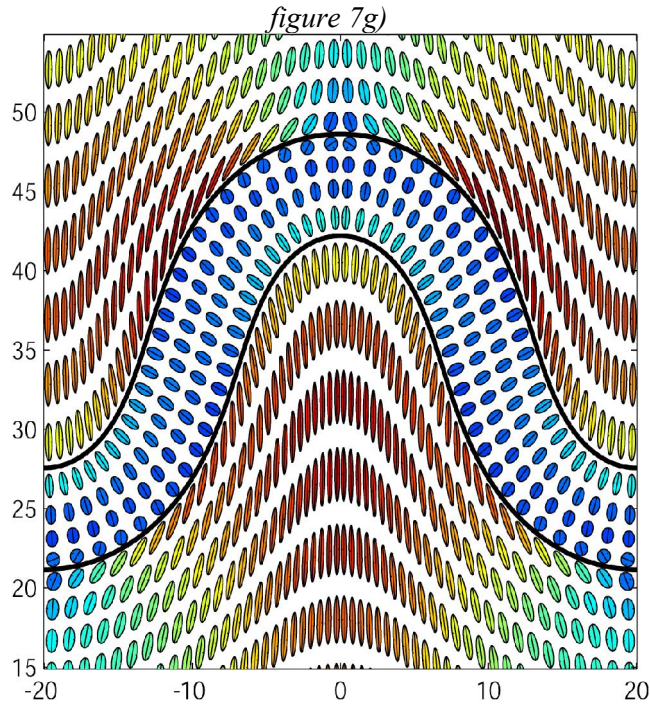
25% shortening



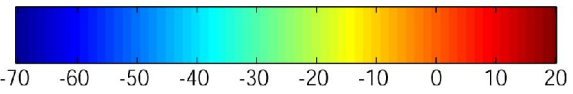
40% shortening



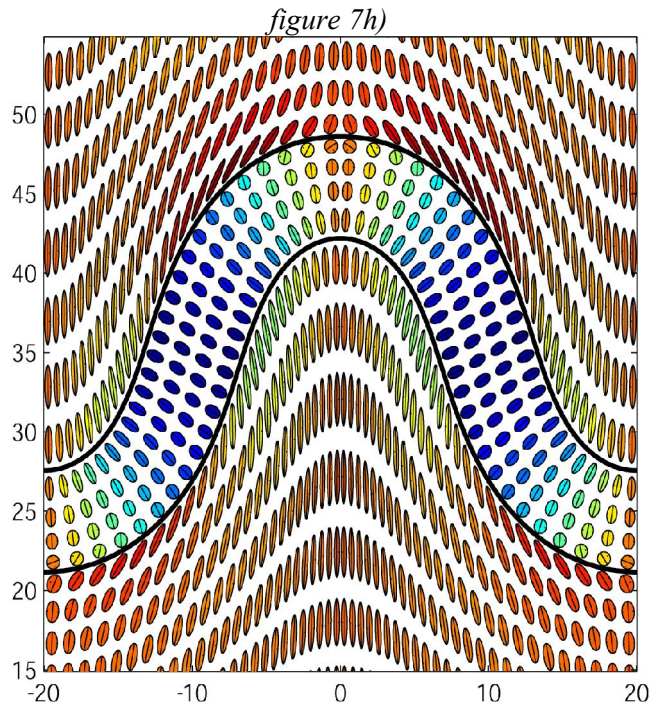
50% shortening



Color-bar for accumulated von Mises  
equivalent strain  $\Sigma \epsilon_{eqv}$



Color-bar for finite rotation angle  
in degrees  $\Sigma \alpha$



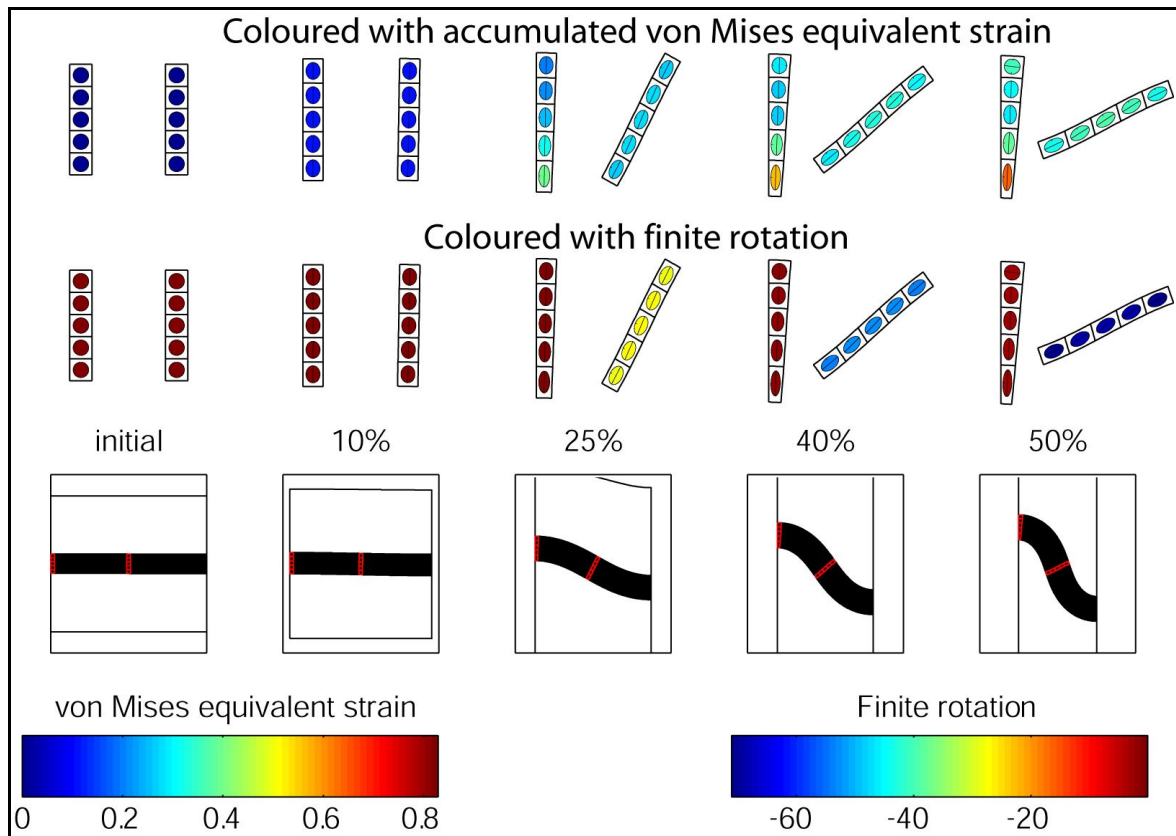


**Fig. 8:** Strain-evolution of a single vertical beam in the hinge zone and on the fold limb, respectively. The beams are indicated in the lower most big scale figures. The strain ellipses in the upper most figures are colored with the accumulated von Mises strain, while the ellipses in the figures in the middle are colored with the finite rotation angle.

### 3.4.2. Finite and incremental strain distribution, the neutral line

Many authors working on folds (e.g. Ramsay and Huber, 1989) propose the existence of a neutral line along which there is zero strain between domains of layer-parallel shortening and layer-parallel extension in the stiff layer. Figure 9 shows that a strict difference has to be made between the finite neutral line and the incremental neutral line. The initial layer-parallel shortening in the hinge region leads to strongly elongated ellipses before buckling starts (figure 8 at 10%). As soon as the fold begins growing, bending of the hinge leads to incremental extension in the outer arc and to incremental compression in the inner arc. In the inner arc this additional compression intensifies the far-field compression and the ellipses become even more elongated. In the outer arc, however, bending-related extension weakens the far-field compression and the finite strain ellipses return to circular or even to horizontally elongated shapes. The transition from horizontally to vertically elongated ellipses is referred to as the finite neutral line, whereas the transition from bending-related, incremental, layer-parallel extension to compression is referred to as the incremental neutral line.

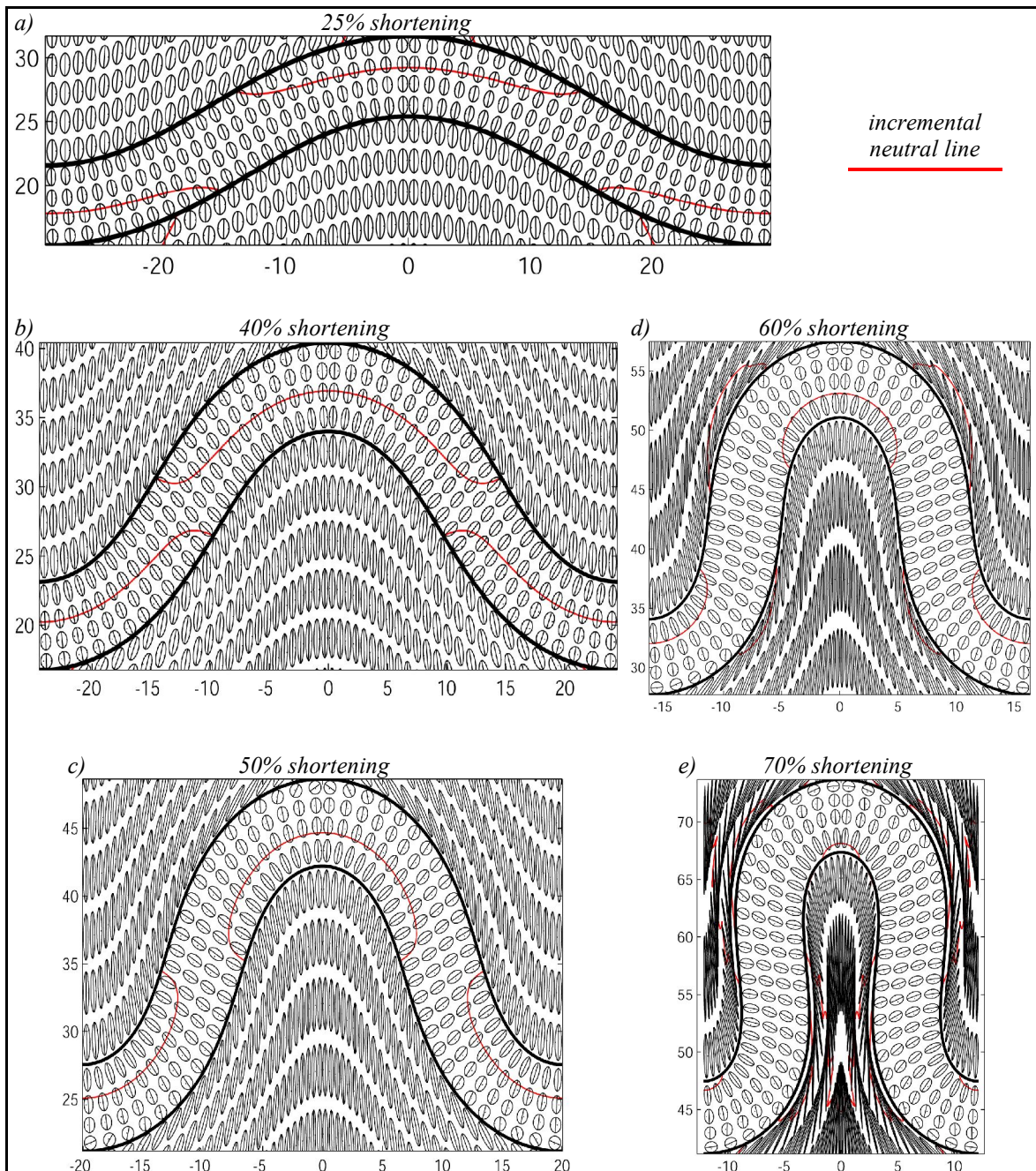


**Fig. 9:** Fold shapes of a single layer fold with a viscosity contrast of 100 at different stages of shortening. The finite strain ellipses are drawn over the whole domain even though they are hardly recognizable in the matrix at higher stages. The incremental neutral line is drawn in red as the zero-contour of the layer-parallel strain rate. The finite neutral line has to be imagined between layer-parallel elongated finite strain ellipses and the ones elongated normal to the layer. A more detailed view of the hinge region is given in figure 10.

Since the finite rotation angle is known at every integration point according to equation (26) the strain rate tensor in the  $(x,y)$ -coordinate system can be transformed into a  $(x',y')$ -coordinate system with  $x'$  parallel and  $y'$  orthogonal to the layer. The incremental neutral line in figure 9 (red line) is then calculated as the zero-contour of this layer-parallel strain rate. The finite strain ellipses are drawn to visualize the position of the finite neutral line. Figure 10 shows a detailed view of the hinge region with a single beam, but with ten strain ellipses instead of four. The beam is indicated in red in the lower pictures. At each deformation stage the finite strain ellipses are shown in the left beam, the incremental strain ellipses in the right beam. Since the shape of the beam is the result of the finite deformation, the incremental strain ellipses do not fit into the subdivisions of the beam. The incremental neutral line is indicated in red as in figure 9. The finite neutral line in blue is placed between the strain ellipses by hand.

Both neutral lines move through the fold from outer to inner arc. The initial layer-parallel shortening elongates the finite strain ellipses vertically. Because in the outer arc this shape first has to go back to circular, the finite neutral line moves much later than the incremental neutral line through the fold. This indicates that layer-parallel shortening, during the early history of deformation, has a high influence on the distribution of the finite strain.

In figure 9 the zero-contour of the layer-parallel strain rate and the finite strain ellipses are drawn both in the layer and in the matrix. The discussion above only considers the situation within the stiff layer. Since the strain ellipses in the matrix are hardly recognizable for higher stages of shortening, they are not considered extensively. The same applies for the zero-contour drawn in the matrix, since it makes no sense to speak of a layer-parallel strain rate in this matrix.

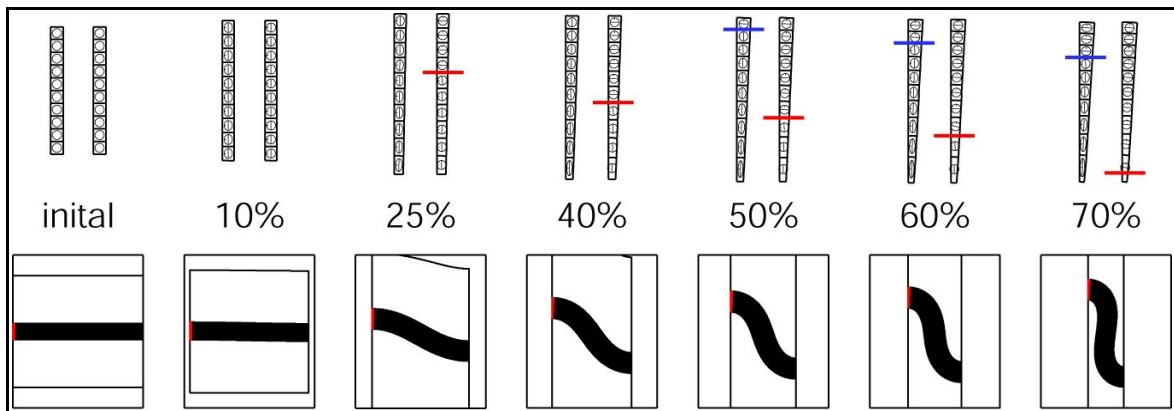


**Fig. 10:** Finite (left beams) and incremental strain ellipses at the fold hinge at different stages of shortening for a single layer fold with a viscosity contrast of 100. The incremental neutral line (red) moves much earlier through the fold than the finite neutral line (blue).

During this study the investigation of single layer folds also involved experiments on exactly the same geometries as described above but with different viscosity contrasts. The results of these experiments are presented in appendix E. The conclusion is that with decreasing viscosity contrast both the incremental and the finite neutral line move later and slower through the fold, respectively. This means that the layer-parallel shortening during early deformation has a higher influence on the distribution of finite strain if the viscosity contrast is low. In other words, layers with a low viscosity contrast amplify slower and later and the ratio of layer-parallel shortening to amplification is higher. In addition, the difference in both the accumulated von Mises equivalent strain and the finite rotation angle between the layer and the matrix decreases with decreasing viscosity contrast. The fold limbs rotate less but deform more and therefore become more and more similar to the matrix. This is straightforward since there is no difference between layer and matrix for a viscosity contrast of one.

### 3.5. Finite strain in double layer folds

The multilayer systems simulated in chapter 4 are always situated between two much thicker layers but with the same viscosity as the stiff layers ( $\mu = 100$ ) of the multilayer system. Therefore, the strain distribution and deformation history of a simple double layer system is investigated prior to the real multilayer system. These simulations pay special attention to the matrix between the two stiff layers. The geometrical and numerical setup used is given in table 3.

<i>Setup for experiments on double layer folds</i>	
<i>Viscosity of both layers</i>	$\mu_l = 100$
<i>Viscosity of the matrix</i>	$\mu_m = 1$
<i>Initial layer thickness of both stiff layers</i>	$H_0 = 5$
<i>Type of initial perturbation for both stiff layers</i>	<i>Half cosine. Same perturbation for upper and lower interface of both layers.</i>
<i>Amplitude of initial perturbation</i>	$\frac{A_0}{H_0} = \frac{1}{100}$ for both layers
<i>Initial thickness of matrix above and below layer</i>	$H_{outer\ 0} = 15$
<i>Initial thickness of matrix between layers</i>	$H_{inner\ 0} = 5$ (equal to thickness of thick layers)
<i>Width of domain</i>	$L_x = 40$ (half wavelength for a single layer for a viscosity contrast of 100)
<i>Time increment</i>	$\Delta t = 10^{-3}$
<i>Horizontal resolution</i>	301 nodes
<i>Vertical resolution over layers</i>	31 nodes
<i>Vertical resolution over matrix</i>	31 nodes
	Total vertical resolution 45451 nodes
	151 nodes

**Table 3:** Fundamental definitions for the experiments on double layer folds.

### 3.5.1. Three phases of progressive deformation

For a first investigation concerning double layer systems, the matrix thickness between the two stiff layers is chosen equal to the layer thickness. The geometries at different stages in the folding history of such a system are shown in figure 11 together with the finite strain ellipses colored with the accumulated von Mises equivalent strain (upper pictures) and the finite rotation angle, respectively. As in figure 7, only the right half of each picture is calculated and then mirrored to have a whole wavelength to study. Therefore, the finite rotation angles in the left halves of the lower pictures indicate the wrong sense of rotation. The two color-bars on every page give the color scheme for each picture.

After 10% shortening (figure 11a and b) only a very slight bending of the two layers is noticeable. Buckling is not initiated and no difference between the matrix between the layers, the matrix surrounding it and the layers themselves is visible in terms of finite rotation angle and accumulated strain. The situation is roughly the same as in figures 7a and b. The orientations of the finite strain axes is vertical and constant over the whole domain.

After 20% shortening (figures 11c and d) the buckling process is initiated and the fold limbs of the two stiff layers start to rotate (light blue in figure 11d) and the finite strain ellipses in the matrix between the two stiff layers start to rotate in the opposite direction. In terms of accumulated strain there is still no big difference between the stiff layers and the matrix in between. But note that the color scheme extends to much higher values for both the accumulated strain and the finite rotation angle than in figure 7. Therefore the differences are more difficult to distinguish. In addition, the orientations of the finite strain ellipses in the surrounding matrix near the outer arc of the fold is different for the anticline and the syncline. This is due to different conditions at the upper and lower boundaries. While the upper boundary is a free surface the lower has a free slip condition which essentially means that it has a zero vertical velocity. The matrix above the anticline is pushed upwards from the growing fold and can move away because the boundary is deformable. The matrix below the syncline is pushed downwards but is blocked by the lower boundary. Therefore the matrix experiences a strong vertical compression and the finite strain ellipses rotate to be horizontally elongated. If the matrix surrounding the fold was the main subject of this chapter the boundaries would have to be much further away from the fold. But since the attention lays on the matrix between the two stiff layers this phenomenon is ignored.

At 30% shortening (figures 11e and f) the phenomena described above are more developed and the matrix between the layers clearly differs from the layers. The accumulated strain reaches much higher values than in the surrounding matrix and the absolute value of the finite rotation angle already reaches about the same values as in the fold limbs of the stiff layers, although the sense of rotation is different (orange color in the matrix, blue in the layers in figure 11f). Both the accumulated von Mises strain and the finite rotation due to rigid body rotation do not reach the highest values in the middle of the matrix at the inflexion point as one could expect, but between the inflexion point and the fold hinge right at the boundary to the convex curved stiff layer. The thickness of the matrix between the two stiff layers changes from hinge to inflexion point. Measured orthogonal to the layer boundary, the hinge becomes thicker and the limbs thinner. At the same time, the two stiff layers tend to form parallel folds (the orthogonal layer thickness is constant over the whole wavelength).

After 40% shortening (figures 11g and h) the highest values of the accumulated von Mises equivalent strain and the finite rotation angle are reached for this deformation sequence and all the phenomena described above are fully developed and clearly visible. It is now obvious that the stiff layer at the inner arc is bent more than at the outer arc. The matrix between the two layers is strongly rotated (red colors in figure 11h) and deformed (red colors in figure 11g). The existence of a strong rotation and a strong shape-change at the same time indicates that the main part of the deformation is a layer-parallel shear deformation. This deformation type contains both properties. A second part of the deformation is the flattening of the matrix normal to the layer surfaces which squeezes the matrix from the limbs towards the hinges.

**Fig. 11 (pages 26 to 29):** Growing double layer fold with a viscosity contrast of 100 at different stages of far-field shortening. Strain ellipses in the upper pictures are colored with von Mises equivalent strain. The ones at the bottom are colored with finite rotation angle. The corresponding color-bars are given on every page. a) and b) 10% shortening, c) and d) 20% shortening, e) and f) 30% shortening, g) and h) 40% shortening. For more information see text.

10% shortening

figure 11a)

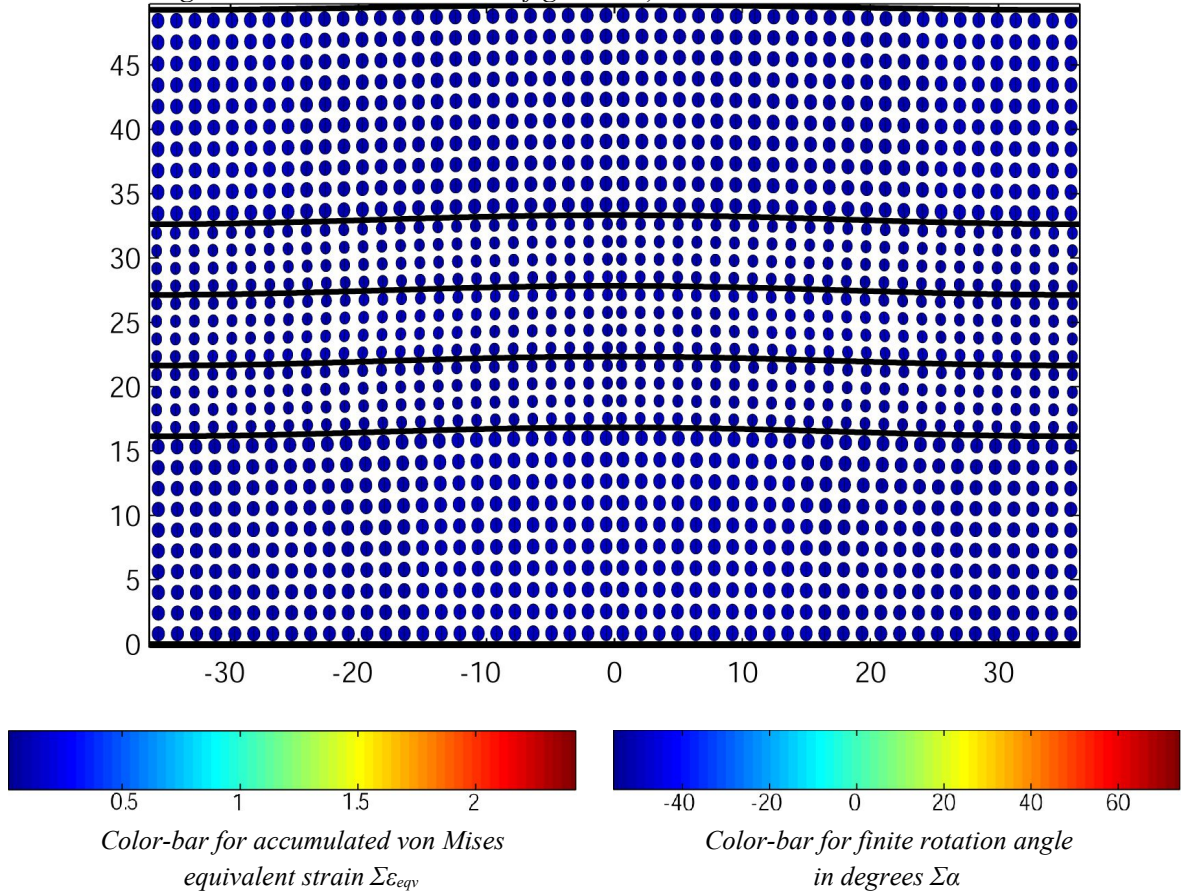
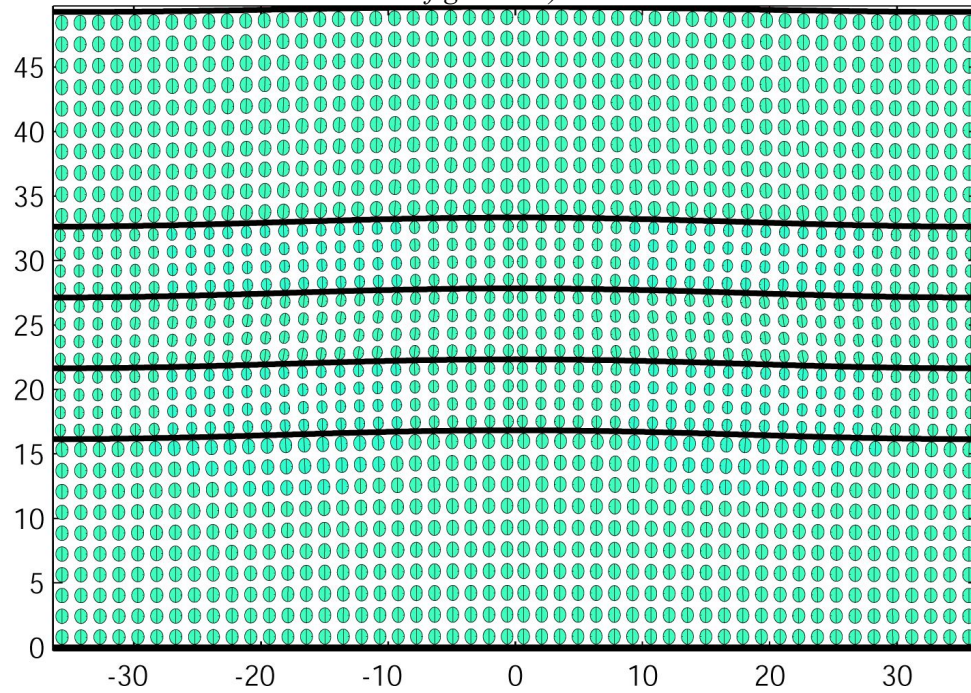
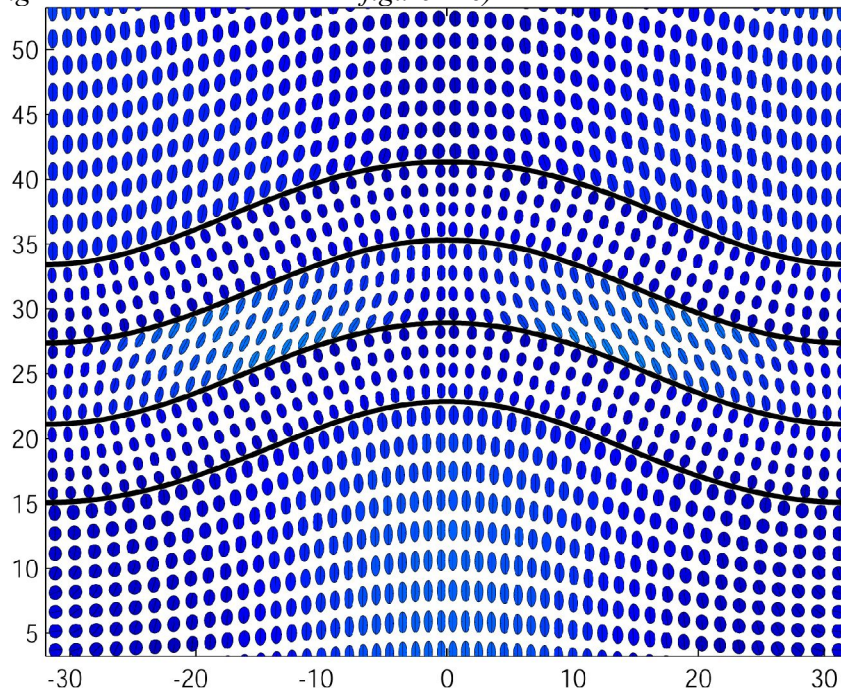


figure 11b)

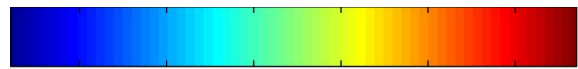


20% shortening

figure 11c)

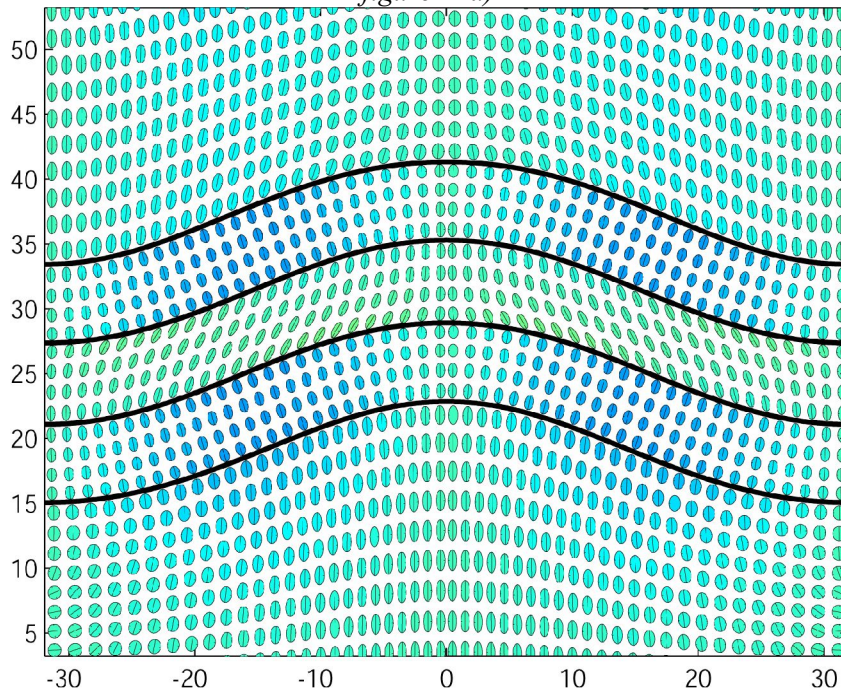


Color-bar for accumulated von Mises  
equivalent strain  $\Sigma \epsilon_{eqv}$



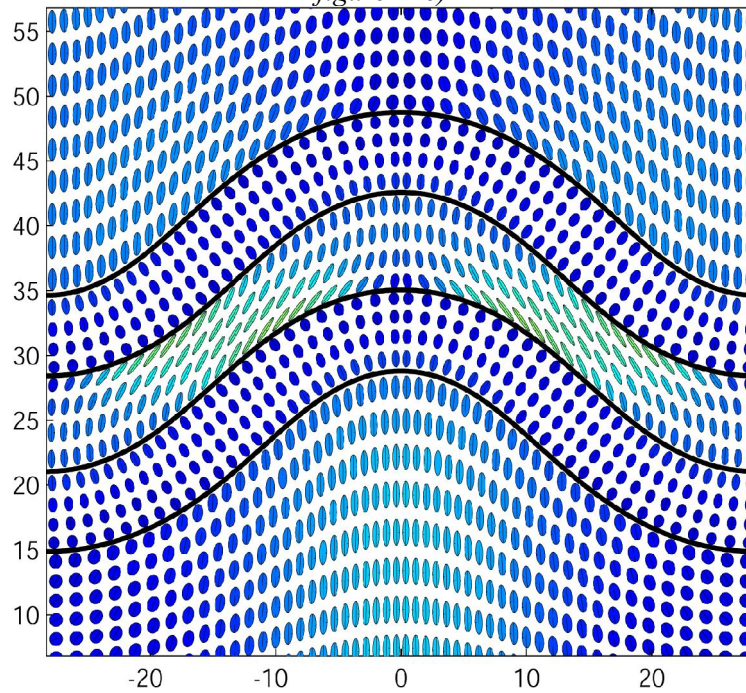
Color-bar for finite rotation angle  
in degrees  $\Sigma \alpha$

figure 11d)



30% shortening

figure 11e)

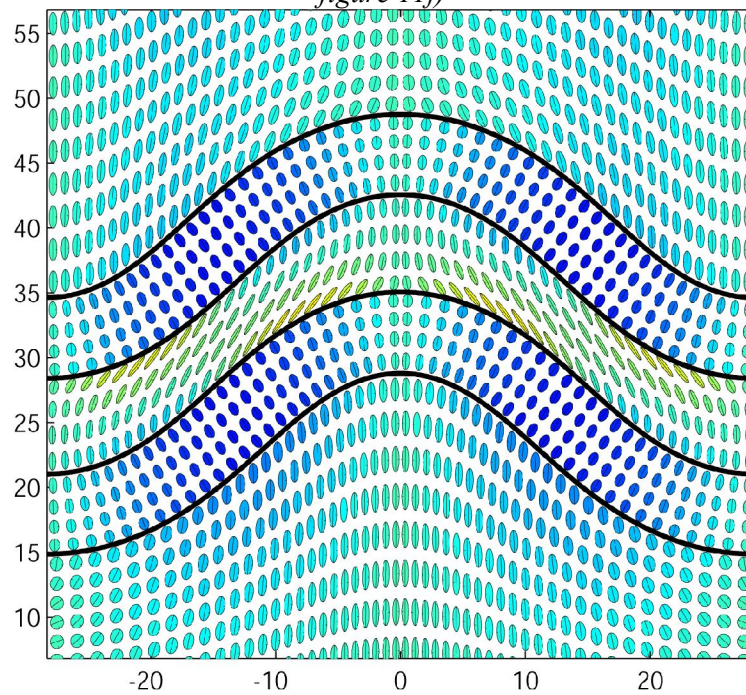


Color-bar for accumulated von Mises  
equivalent strain  $\Sigma \epsilon_{eqv}$



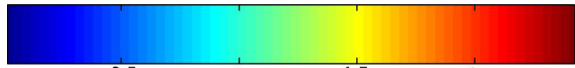
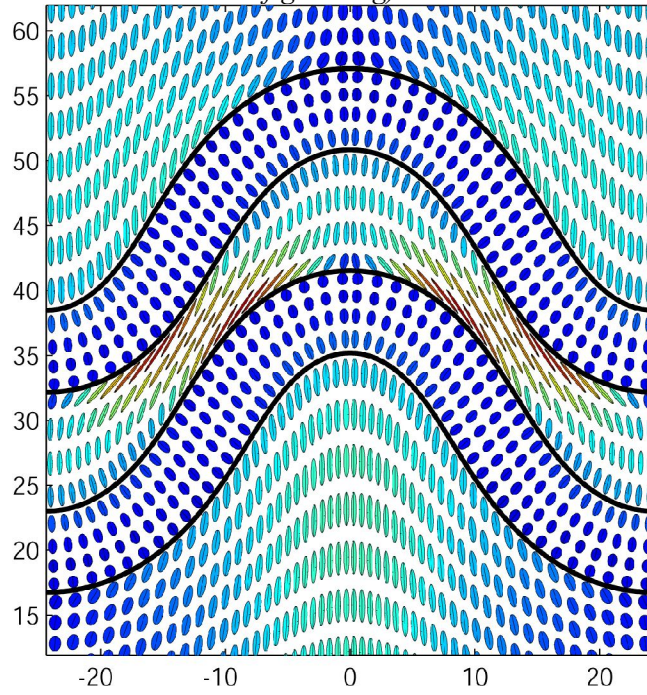
Color-bar for finite rotation angle  
in degrees  $\Sigma \alpha$

figure 11f)

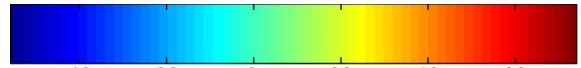


40% shortening

figure 11g)

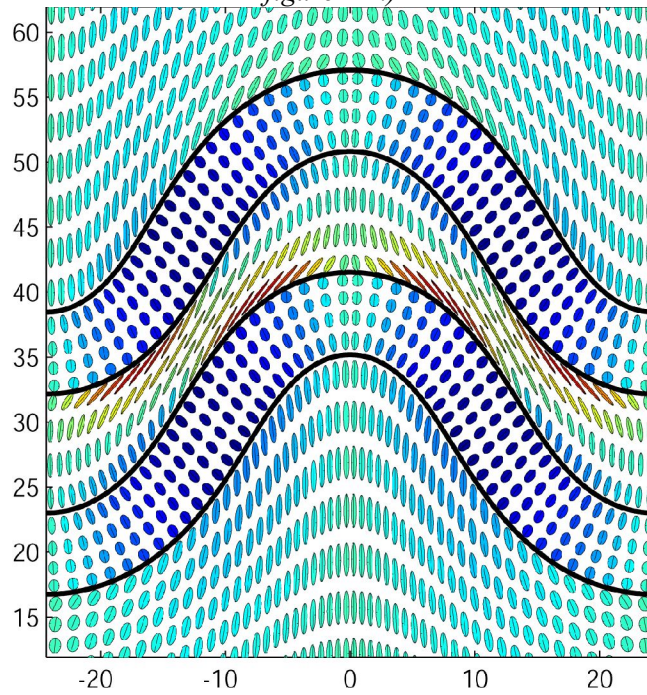


Color-bar for accumulated von Mises  
equivalent strain  $\Sigma \varepsilon_{eqv}$



Color-bar for finite rotation angle  
in degrees  $\Sigma \alpha$

figure 11h)



The deformation history of the matrix between the two stiff layers near the inflexion point can be summarized in three phases:

- 1) The neighboring stiff layers have not started to buckle and the dominant deformation in the whole system is a layer-parallel compression. The matrix in the middle is nearly indistinguishable from the layers in terms of accumulated strain and finite rotation.
- 2) The stiff layers start to buckle and a layer-parallel shear deformation is active in the matrix in-between. This leads to a strong shape-change and rigid body rotation, stronger than in the stiff layers or in the surrounding matrix.
- 3) Strong buckling and closure of the two folded stiff layers leads to a compression normal to the layer surfaces. The matrix is squeezed out of the limb region towards the hinge.

The three phases are not strictly separated. Layer-parallel shear, for instance, is still prominent in phase 3. However, these three deformation phases in the matrix between two stiff layers have a major impact on the development of multilayered parasitic folds described in chapter 4.

Further insights into the deformation history of a double layer fold system are provided in figure 12. Nine originally vertical beams are passively deformed with the growing folds and plotted with the corresponding finite strain ellipses. The beams are initiated in a way that their subdivisions are quadratic at the initial stage. In the sequence of figure 12 the three deformation phases described above are clearly observable. After 10% shortening (figure 12b) the matrix between the two layers is almost only compressed horizontally and hardly any shear deformation occurred. After 25% (figure 12c) shearing is stronger near the convex interface and strongest between the inflexion point and the hinge. This is clear in the middle beam of the matrix which deforms asymmetrically with a very strong deformation near the convex interface and a weaker deformation near the concave interface. The beam at the inflexion point of the matrix, however, deforms symmetrically. The shearing of the beam as a whole is about the same as in the middle beam but it is more uniformly distributed and contains no such maxima as in the middle beam. This effect is even stronger after 40% and 50% shortening (figures 12d and e). The middle beam develops a tail-shape with a very strong deformed tail at the convex interface. This tail extends between the two stiff layers into the zone influenced by the compression normal to the layers, which developed late in the deformation sequence because of the strong amplification of the stiff layers. Therefore, the tail of the middle beam is not only sheared but also compressed, which intensifies the strongly elongated shape of the finite strain ellipses. The same shearing-flattening-combination takes place in the center of the beam at the inflexion point, while the two ends lie outside this zone of very strong deformation. As a consequence the beam at the inflexion point develops a S-shape. Both the tail-shape of the middle beam and the S-shape of the beam at the inflexion point are also recognizable from the arrangement of the finite strain ellipses in figure 11.

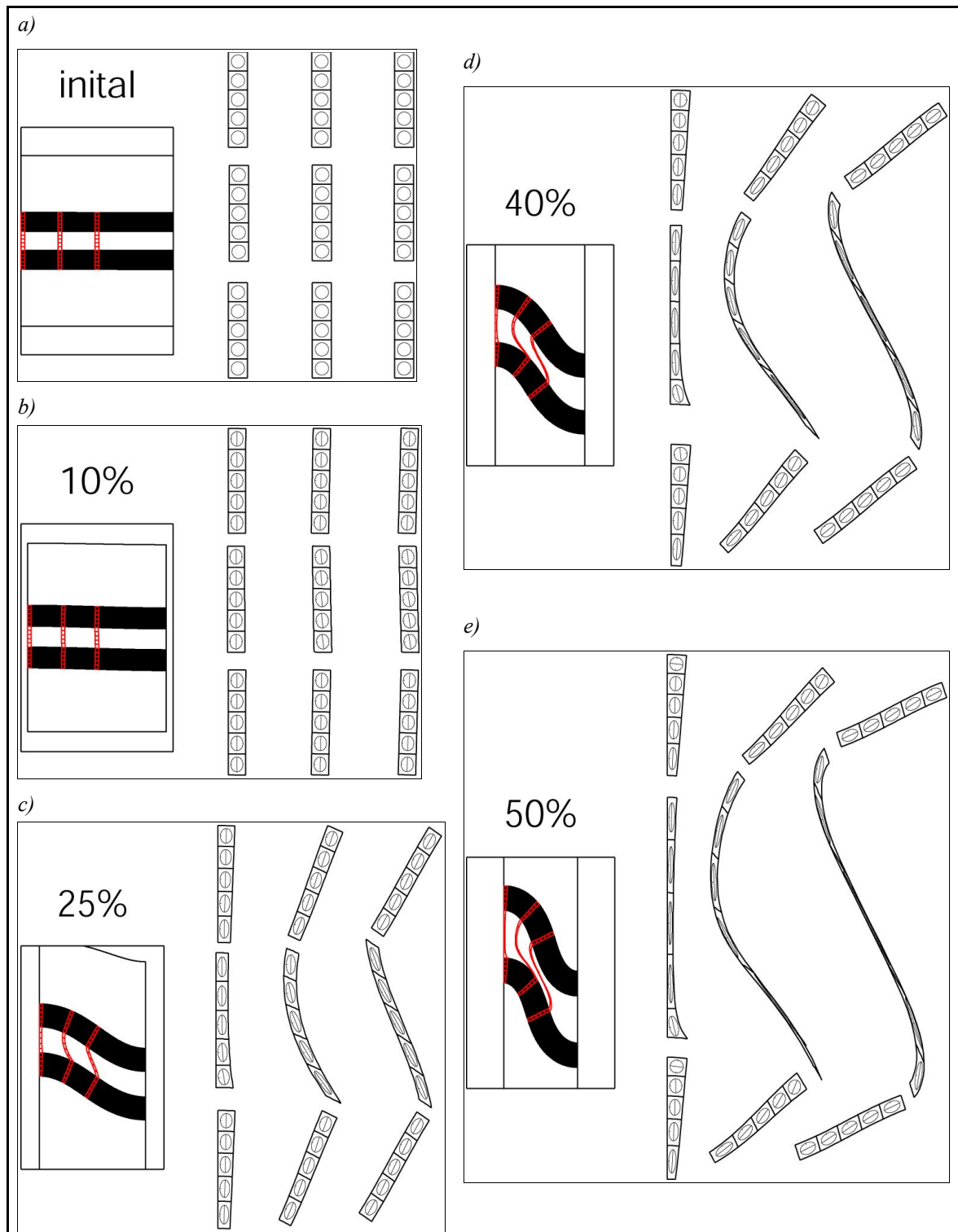


**Fig. 12:** Finite strain-evolution in a double layer fold with a viscosity contrast of 100 and a layer spacing equal to the layer thickness. Illustrated are nine beams, six in the stiff layers and three in the matrix in between. The arrangement of the nine beams is the same as in the big scale figures on the left side of each deformation stage.

### 3.5.2. Three regions of deformation in the matrix between the stiff layers

In chapter 3.5.1. it is foreshadowed that the three phases of progressive deformation do not apply in the whole matrix between the two stiff layers and that this matrix has to be divided into different regions. These different regions undergo different paths of progressive deformation. The three described phases of chapter 3.5.1. apply only in the region near the inflexion point.

The three deformation regions are:

- 1) Near the inflexion point. This region is characterized by the three phases of progressive deformation described in chapter 3.5.1. Layer-parallel shortening is followed by shearing and some flattening normal to the layer.
- 2) Near the fold hinge of the matrix. This region is characterized by layer-parallel compression during the whole deformation history, which can be approximated with a pure shear regime.
- 3) A transition zone between regions 1 and 2. The two different deformation paths of regions 1 and 2 overlap and a complicated deformation mechanism characterizes this region. Shearing and flattening are less distinct compared to region 1 but strong enough so that a pure shear approximation is inappropriate.

These three regions are difficult to distinguish but nevertheless this is tried in figures 13 to 15. In figure 13 the layer-parallel strain rate between the two stiff layers is shown for the same deformation stages as in figure 11. Negative values (blue) indicate layer-parallel compression while positive values (green to red) indicate layer-parallel extension. Where possible, the transition from these two regimes are pointed out with a black line where the layer-parallel strain rate is equal to zero. This zero contour is referred to as the incremental neutral line in the matrix. The same observations as in figure 11 can be made in figure 13. After 10% shortening only layer-parallel compression takes place. After 20%, 30% and 40% shortening, flattening normal to the layer increases. It is clear from figure 13 that the matrix between the two layers needs to be divided in terms of deformation history. The region 2, near the hinge, never experiences layer-parallel extension while the region 1, near the inflexion point, is firstly compressed and later extended. Together with a diffuse transition zone, region 3, this supports the idea of a tripartition of the matrix.

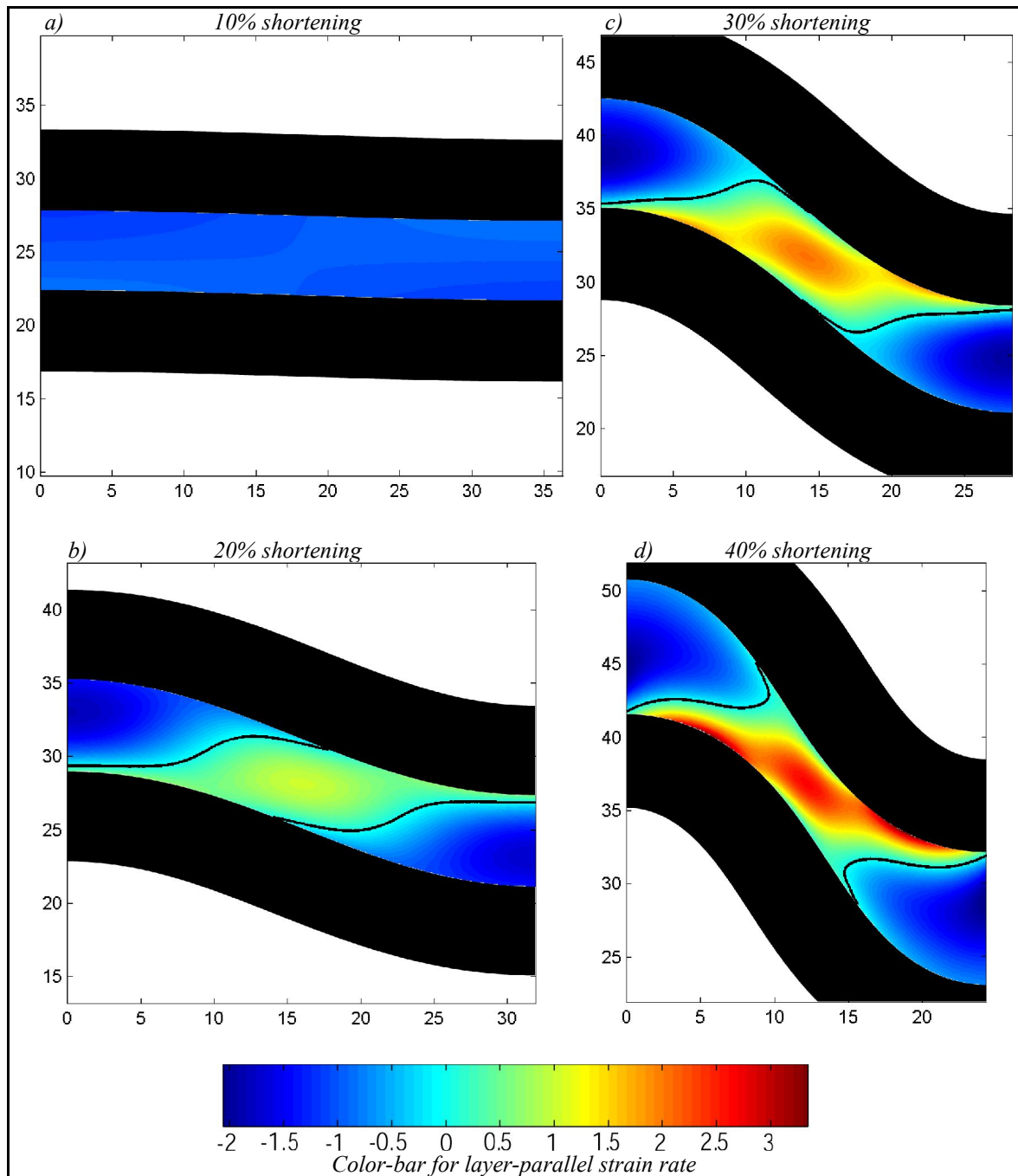


**Fig. 13:** Layer-parallel strain rate in the matrix between two stiff layers of viscosity contrast of 100. The color-bar at the bottom of the figure applies to all pictures. The initial distance between the two layers is equal to the layer thickness. The incremental neutral line in black is defined as the transition between layer-parallel compression and extension.

In contrast to figure 13 the strain can also be looked at as an accumulated finite quantity. This is done in figure 14. As a measure for the finite strain the distance between every point of both interfaces bounding the matrix is calculated and compared with the initial distance between the two layers. The area where this distance is shortened is colored in red, which means that a finite flattening normal to the layer takes place. In figure 14 only the 30% and the 40% shortening stages are shown because this red area does not develop earlier. It is clear that the area of finite flattening broadens with increasing shortening. The boundaries of this red area are referred to as the finite neutral line.

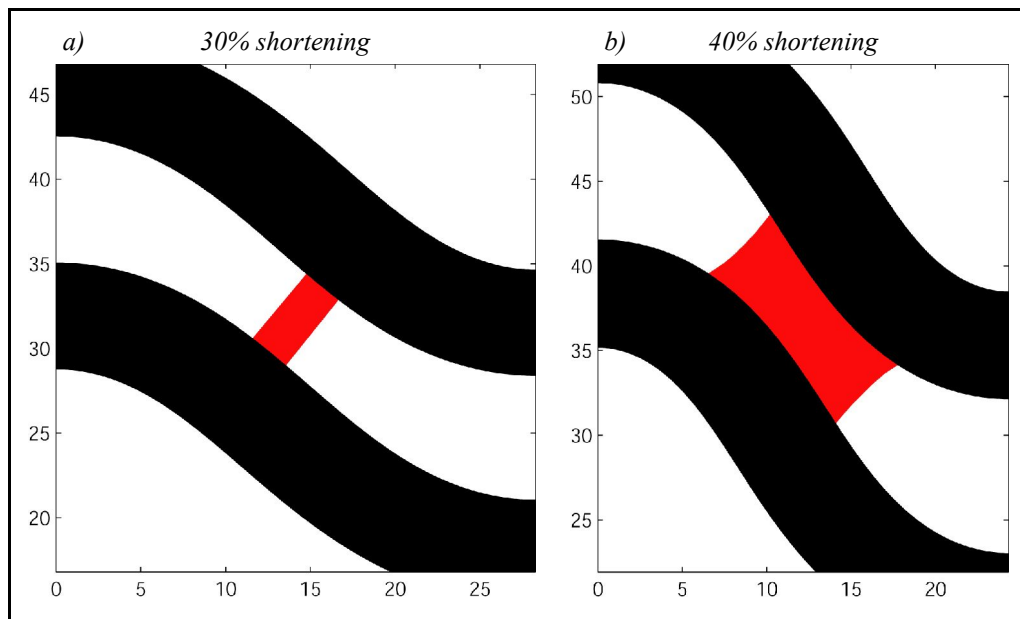


**Fig. 14:** Area in the matrix of finite flattening between the two layers. In the red area the distance between the two layers is shorter than in the undeformed stage. This area develops shortly before 30% background shortening and gets broader with increasing shortening.

The areas of incremental flattening (figure 13) and finite flattening (figure 14) are compared in figure 15a. The area of incremental flattening is defined as the area bounded by the two thick layers and the two zero contours of the layer-parallel strain rate. While the whole area of the matrix between the two stiff layers is equal to 100%, the blue dots give the percentage of the area of incremental flattening and the red dots give the percentage of the area of finite flattening. Although the geometry of the neutral line in the matrix is completely different than in the stiff layer (figure 9) similar conclusions can be drawn. The area of incremental flattening develops much earlier and moves earlier and faster through the material than the area of finite flattening. The outcome is that the area of finite flattening is always smaller than that of incremental flattening. Layer-parallel shortening (equal to extension normal to the layer) of early deformation first needs to be redone before finite flattening takes place. This is exactly the same mechanism as in the hinge region of the stiff layers described in chapter 3.4.2.

It is noteworthy that both the areas of finite and incremental flattening decrease after a certain amount of far-field compression, whereas it is earlier the case for the area of incremental flattening. This suggests that at a certain point the two fold limbs draw near to each other faster than the area of flattening broadens. However, this effect does not affect the relation between the area of incremental and finite flattening described above.

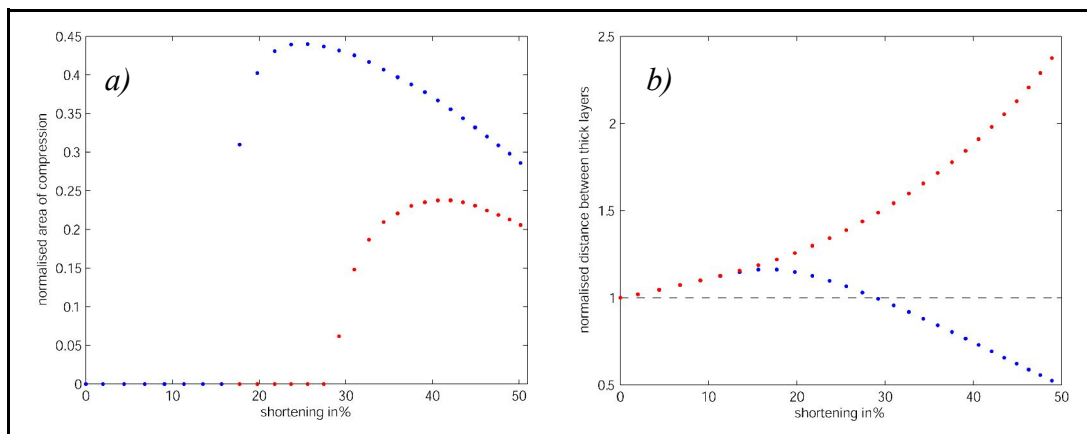


**Fig 15:** a) Blue: Area of incremental flattening normal to the layers; Red: Area of finite flattening normal to the layers. Incremental flattening occurs earlier in the deformation history and covers bigger areas. b) Blue: Minimal distance between the two layers. This minimal distance is situated near the inflexion point; Red: Maximal distance between the two layers measured normal to the layers at the fold hinge.

Figure 15b) shows another distinct difference between region of deformation 1 and 2. The minimal distance between the layers is situated near the inflexion point (region 1) while the maximal distance measured normal to the layers is situated in the hinge region. Both distances are normalized with the initial distance between the two stiff layers. These two distances evolve differently. Continuous layer-parallel compression in the hinge region leads to a steady increase of the distance between the layers (red dots). The region near the inflexion point (blue dots), however, is characterized by the three phases of deformation described in chapter 3.5.1. During layer-parallel compression, this region undergoes the same layer-parallel shortening as in the fold hinge and the blue dots lie behind the red ones. Deformation phase 2 is mainly characterized by shearing and the normalized distance between the layers stays constant for a short while. Later in the deformation history (phase 3), flattening normal to the layers leads to a decrease of the distance between the layers. This is the case as soon as approximately 17% shortening is reached, which is also the first appearance of the area of incremental flattening in figure 15a. The normalized minimal distance falls below one (the initial value) for a far-field shortening of about 28%. This is also the point where the area of finite flattening first occurs in figure 15a.

## **Chapter 4**

# **Asymmetric parasitic fold development in multilayer systems**

### **4.1. Introduction**

The multilayer systems investigated in this chapter are always situated between two much thicker layers like those described in chapter 3.5. The insights into double layer systems can be used to investigate the multilayers set in between. The boundary conditions are the same as described in chapter 2.5., horizontal compression with a free slip boundary at the bottom and an open surface at the top. Although this simple set of boundary conditions is used, the presence of the two thicker layers induces a complicated strain field in between. This chapter shows that under certain circumstances, it is possible to get asymmetric parasitic folds. The model produces folds on two scales, the primary folds and the parasitic folds. This feature is important because it is often observed in nature.

The geometrical and numerical setup of the models presented in this chapter, which are the same for every model is given in table 4. Further information is given in the text where the different models are described.

<b>Setup for experiments on multilayer folds</b>	
Viscosity of stiff layers	$\mu_l = 100$
Viscosity of the matrix	$\mu_m = 1$
Initial layer thickness of both thicker layers	$H_{thick 0} = 5$
Initial layer thickness of layers of the multilayer stack	$H_{thin 0} = 0.1$
Initial thickness of the matrix between the layers of the multilayer stack	$H_m = 0.3$
Initial thickness of matrix above and below thick layers	$H_{outer 0} = 20$
Type of initial perturbation for both thicker layers	Half cosine. Same perturbation for upper and lower interface of both layers.
Type of initial perturbation for layers of the multilayer stack	Random white noise. Same perturbation for upper and lower interface of each layers but different perturbation for every layer.
Width of domain	$L_x = 40$ (half wavelength for a single layer with an initial thickness of 5)
Time increment	$\Delta t = 10^{-3}$
Horizontal resolution	251 nodes

**Table 4:** Fundamental definitions for the experiments on multilayer folds.

## 4.2. Influence of the amplitude of the initial perturbation

Without an initial perturbation of the layer interfaces, all layers would stay horizontal and only layer-parallel shortening and thickening would occur. To study the influence of this initial perturbation a multilayer system is used with the setup given in table 5.

<b>Setup for experiments on multilayer folds with 15 thin layers</b>			
Amplitude of initial perturbation of the thicker layers	$\frac{A_{thick 0}}{H_{thick 0}} = \frac{1}{1000}, \frac{1}{5000}$ and $\frac{1}{10000}$ , respectively		
Amplitude of initial perturbation of layers of the multilayer stack	$\frac{A_{thin 0}}{H_{thin 0}} = \frac{1}{10}$ for all layers		
Vertical resolution over thick layers	9 nodes	Total vertical 313 nodes	Total resolution 78563 nodes
Vertical resolution over thin layers	9 nodes		
Vertical resolution over matrix between layers	9 nodes		
Vertical resolution over matrix outside layers	25 nodes		

**Table 5:** Geometrical and numerical setup for models with 15 thin layers in the multilayer stack. This table is complemented by table 4.

Figure 16 shows the deformed multilayer sequence after 50% shortening for initial amplitude to thickness ratios of  $10^{-3}$ ,  $5 \cdot 10^{-3}$  and  $10 \cdot 10^{-3}$  for both thick layers. The initial amplitude of the thin layers is constant for all three models. In the first case of a ratio of  $10^{-3}$  (figure 16a) there are only real parasitic folds in the hinge region. Near the inflexion point the thin layers are straight and only small parasitic folds are developed in the transition zone. The major part of parasitic folds are approximately symmetric. Only those in the transition zone are slightly asymmetric. In the third case of a ratio of  $10 \cdot 10^{-3}$  (figure 16c) the parasitic folds are strongly developed in the whole domain but they are not asymmetric. The intermediate case of initial amplitude to thickness ratio of the thick layers of  $5 \cdot 10^{-3}$  (figure 16b) develops parasitic folds throughout the whole domain. Additionally the parasitic folds near the inflexion point are clearly asymmetric.

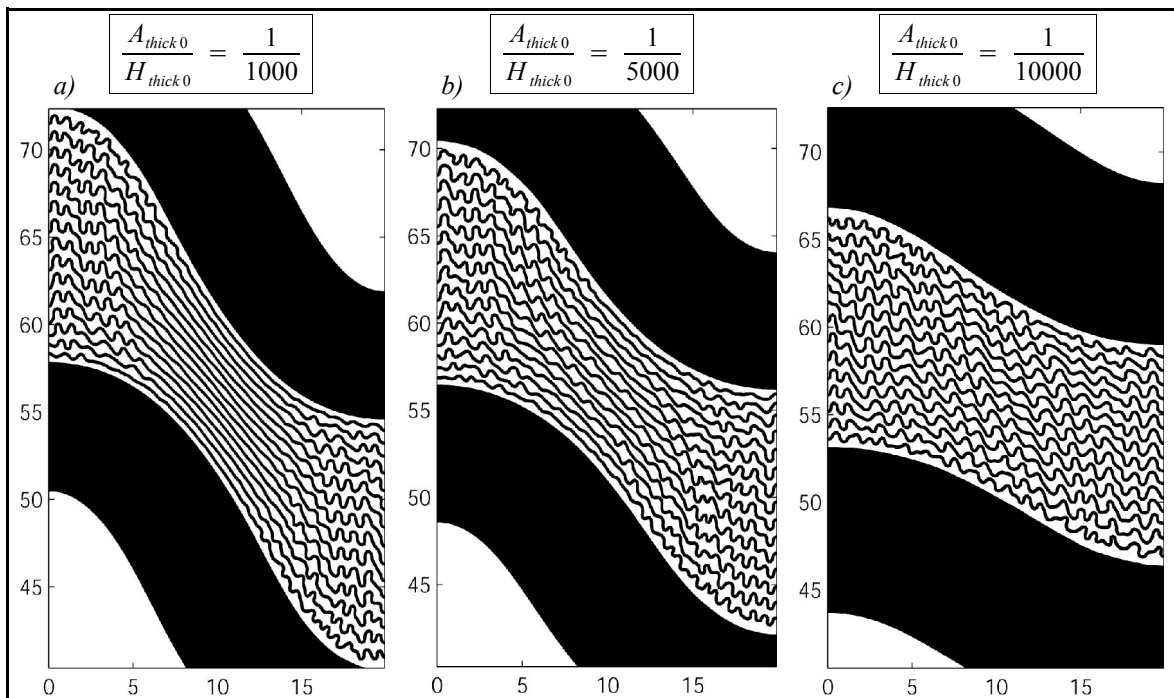


**Fig. 16:** Deformed multilayer sequence between two much thicker layers after 50% of far-field shortening. Three different models are shown with a different initial ratio of amplitude to layer thickness for the thick layers. a)  $10^{-3}$ , b)  $5 \cdot 10^{-3}$  and c)  $10 \cdot 10^{-3}$

The amplitude of the initial perturbation of the thick layers strongly controls on the development of folds in the multilayer stack. The smaller this initial perturbation is, the later and the slower the thick layers amplify. In other words, a small initial amplitude extends the phase of layer-parallel compression before amplification and rotation of the thick layers start. This extended phase of layer-parallel compression for small initial amplitudes allows the thin layers to reach higher amplitudes before buckling of the thick layers starts.

This is illustrated in figure 17 for the two cases of an initial amplitude to thickness ratio of the thick layers of  $10^{-3}$  and  $10 \cdot 10^{-3}$ . The averaged amplitude of the two thick layers is in blue and the averaged amplitude of the thin layers in the hinge region in red. Both amplitudes are normalized with their corresponding initial layer thickness. The red and blue columns, which are set by eye, indicate the initiation of buckling of the thin and the thick layers, respectively. In both cases the initiation of buckling of the thin layers is approximately at 9% shortening because in both models the initial amplitude to thickness ratio of the thin layers is the same. Buckling of the thick layers influences the calculation of the averaged amplitude of the thin layers. Therefore the normalized amplitudes of the thin layers to the right of the blue columns are not to be considered here.

The main difference between the two models is the start of buckling of the thick layers. With an initial amplitude to thickness ratio of  $10^{-3}$  (figure 17a) this happens at around 17% far-field shortening while for the case of the higher ratio of  $10 \cdot 10^{-3}$  (figure 17b) this happens at around 32% shortening. The normalized averaged thickness of the thin layers in the first case reaches a value of about 2 when the thick layers start to buckle. In the second case, the thin layers have more time to amplify and reach a value of 4.5. The intermediate case with initial amplitude to thickness ratio of the thick layers of  $5 \cdot 10^{-3}$  is not shown here but would lie between the two. Figure 16 suggests that for this thesis, this is the most desired case and, for further investigations, initial amplitude to thickness ratio of the thick layers of  $5 \cdot 10^{-3}$  is used.

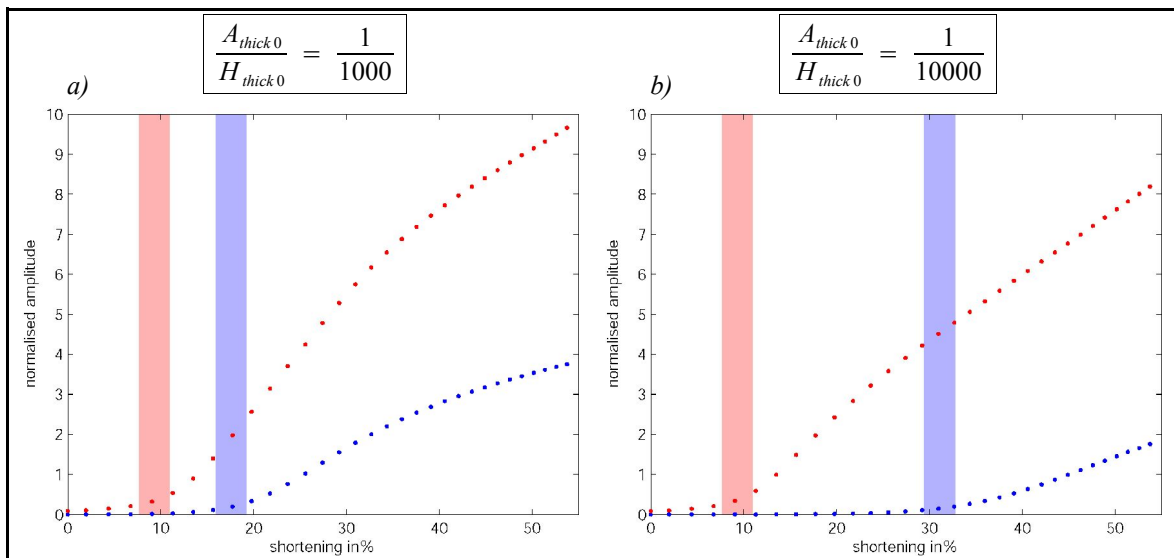


**Fig. 17:** Red: Averaged amplitude of the thin layers in the hinge region normalized with the initial layer thickness of the thin layers; Blue: Averaged amplitude of the two thick layers normalized with the initial layer thickness of the thick layers. The two beams, which are set by eye, indicate the initiation of buckling for the thin layers (red) and the thick layer (blue), respectively. The two subplots are modeled with a different initial ratio of amplitude to layer thickness for the thick layers. The ratio for the thin layers is the same for both subplots.

The fact that buckling of the thick layers is initiated later for small initial amplitudes is also observable in figure 18, which shows the normalized distance between the two thick layers in the hinge region (red dots) and the minimal distance at the inflexion point (blue dots). For both initial amplitude to thickness ratios, of the thick layers the distance at the fold hinge increases with time. This increase is roughly the same in both cases and it indicates a layer-parallel shortening of the hinge region. At the inflexion point the two thick layers draw nearer after a certain amount of far-field shortening, but this happens much earlier for the first case of an initial amplitude to thickness ratio of  $1/1000$  (figure 18a) than for the second case of an initial ratio of  $10/1000$  (figure 18b).

Near the inflexion point the phase of shearing without flattening (zero slope of the blue points) lasts longer in the second case (figure 18b) and more layer-parallel shortening is accumulated at this point, which is expressed as the maximum value of the blue dots. This leads to the higher amplitudes of the multilayer stack between the thick layers observed in figure 17. The short period of shearing in the first case is followed by a strong flattening phase (high negative slope of the blue dots in figure 18a) which even shortens the minimal distance at the inflexion point below the initial distance. In other words the first model of initial amplitude to thickness ratio of  $10 \cdot 10^{-3}$  for the thick layers reaches a state with finite flattening between the two thick layers.

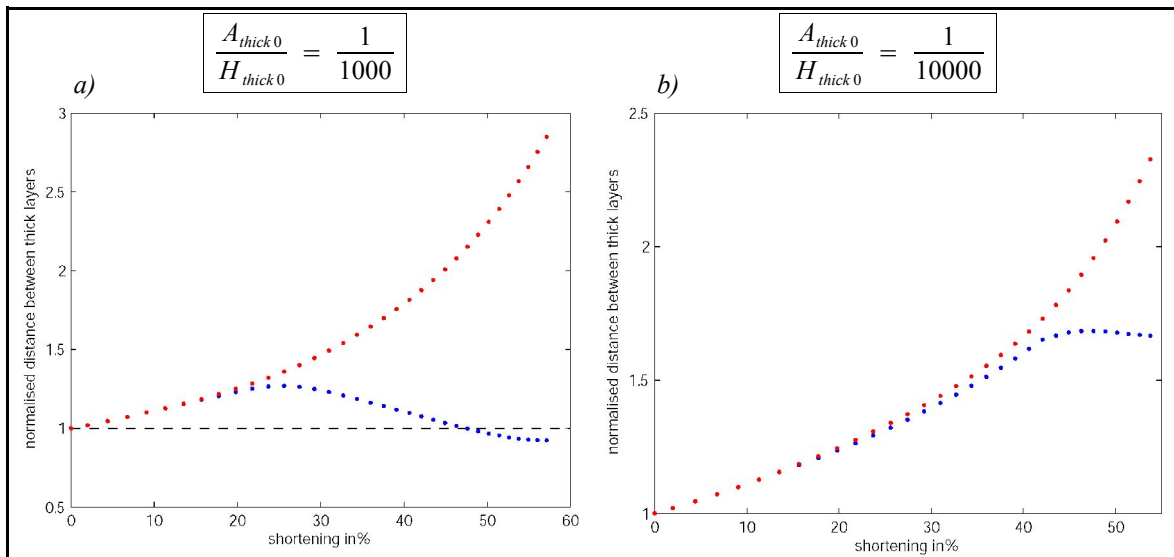


**Fig. 18:** Blue: Minimal distance between the two thick layers. This minimal distance is situated near the inflexion point; Red: Maximal distance between the two thick layers measured normal to the layers at the fold hinge. Between the two thick layers a multilayer stack with 15 layers is situated. a) and b) represent two models with a different initial amplitude to thickness ratio of the thick layers.

### 4.3. Number of layers in the multilayer stack

For the following investigation of the influence of the number of layers in a multilayer stack on the development of asymmetric parasitic folds the setup summarized in table 6 is used.

<i>Setup for experiments on multilayer folds</i>						
<i>Amplitude of initial perturbation of the thicker layers</i>			$\frac{A_{thick0}}{H_{thick0}} = \frac{1}{5000}$ for both layers			
<i>Amplitude of initial perturbation of layers of the multilayer stack</i>			$\frac{A_{thin0}}{H_{thin0}} = \frac{1}{10}$ for all layers			
		<i>Thick layers</i>	<i>Thin layers</i>	<i>Matrix between layers</i>	<i>Matrix outside layers</i>	<i>Total resolution</i>
<i>Vertical resolution</i>	<i>1 layer system</i>	<i>17 nodes</i>	<i>17 nodes</i>	<i>17 nodes</i>	<i>41 nodes</i>	<i>40411 nodes</i>
	<i>5 layer system</i>	<i>11 nodes</i>	<i>11 nodes</i>	<i>11 nodes</i>	<i>25 nodes</i>	<i>43139 nodes</i>
	<i>10 layer system</i>	<i>9 nodes</i>	<i>9 nodes</i>	<i>9 nodes</i>	<i>25 nodes</i>	<i>58483 nodes</i>
	<i>15 layer system</i>	<i>9 nodes</i>	<i>9 nodes</i>	<i>9 nodes</i>	<i>25 nodes</i>	<i>78563 nodes</i>
	<i>20 layer system</i>	<i>9 nodes</i>	<i>9 nodes</i>	<i>9 nodes</i>	<i>25 nodes</i>	<i>98643 nodes</i>

**Table 6:** Geometrical and numerical setup for models with a different number of layers in the multilayer stack. This table is complemented by table 4.

Figure 19 shows the results after 50% far-field shortening of five models with a different number of thin layers. The parasitic folds evolve differently in the different models. For one and five thin layers (figures 19a and b) the parasitic folds mainly develop in the hinge region of the primary fold where they are approximately symmetric. Between the limbs of the thick layers the thin layers are almost straight. The transition zone between the hinge region and the fold limb contains only minor parasitic folds that show a slight asymmetry. The ten-layer-model (figure 19c) shows higher amplitude symmetric folds in the hinge region compared to the previous two models. The amplitudes of the parasitic folds decrease thereby from hinge to inflexion point. The parasitic folds near the inflexion point are well developed and clearly asymmetric (S-shaped for the displayed part of the fold).

Models with 15 and 20 thin layers (figures 19d and e, respectively) show even more distinct asymmetric parasitic folds between the fold limbs of the two thick layers. They have very well developed S-shapes with relatively high amplitude. As in the previous models, the amplitudes increase towards the primary fold hinge, where the parasitic folds are symmetric. Note that figure 19d is the same as figure 16b.

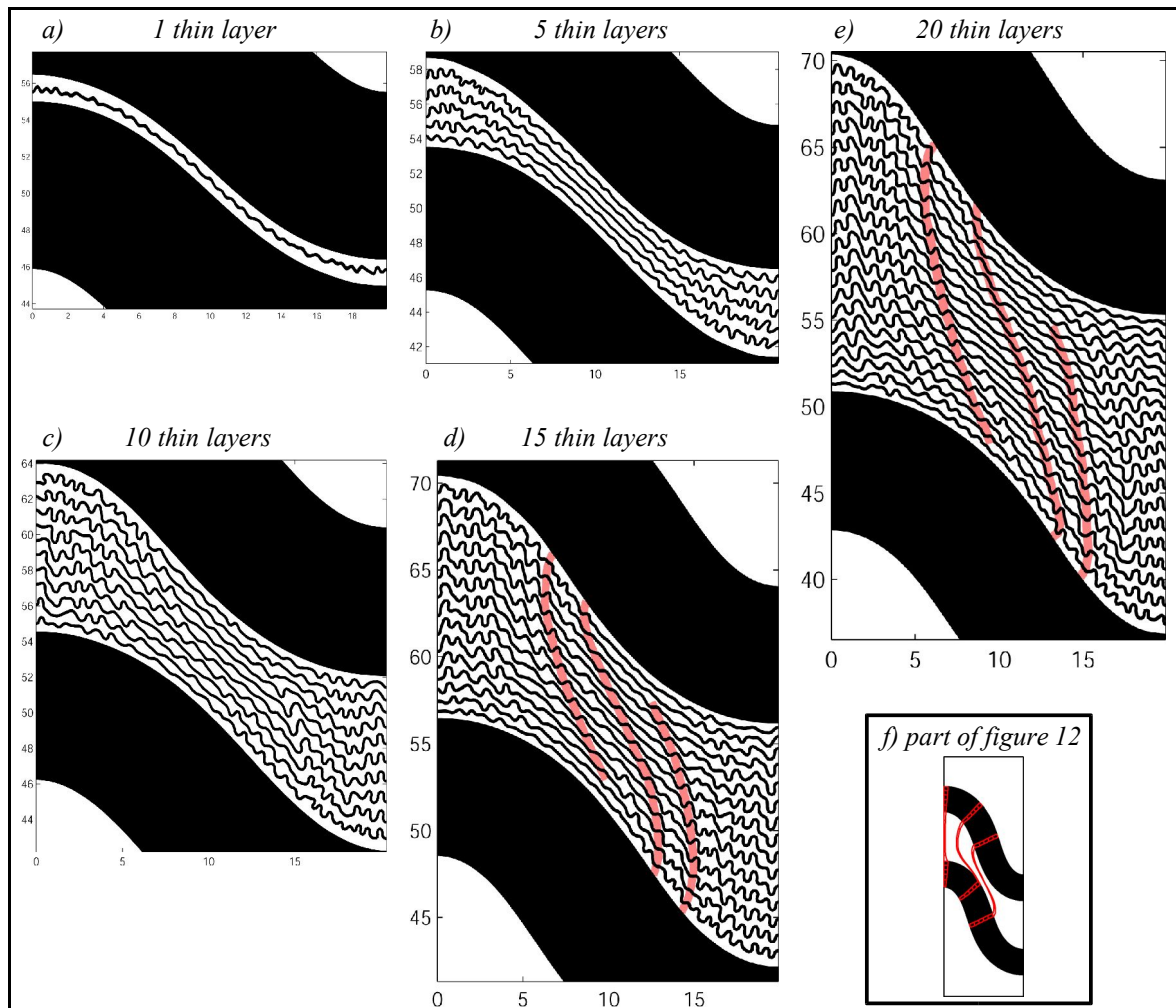


**Fig. 19:** a) – e): Geometry of five different multilayer models after 50% far-field shortening. The different models are built of a different number of thin layers (1, 5, 10, 15 and 20) between two thick layers. f) Intern geometry between the two layers of a double layer system after 50% shortening. Picture taken from figure 12. See chapter 3.5.1 for further information.

A special feature of models with 15 and 20 layers is to be noted. The asymmetric parasitic folds of the multilayer stack lying upon each other are arranged in a way that reproduces the internal geometry between a deformed double layer system shown in figure 19f. The S-shape near the inflexion point and the tail-shape in the transition zone of the originally vertical beams described in chapter 3.5.1. are clear in the multilayer sequence indicated in light red. This special geometry is better developed in the model with 20 thin layers but is still identifiable with 15 layers. The model with a ten-layers stack slightly displays this feature. The much higher amplitudes of the two layers in the inlay of figure 19 compared to the five presented multilayer models is due to the higher amplitude of the initial cosine perturbation of the double layer system. The described geometry between the two thick layers is therefore even more obvious, but it has nothing to do with the presence or absence of the thin layers in between.

For further investigation of the effect of the number of layers on the development of asymmetric parasitic folds figure 20 is considered. It shows the evolution of the averaged amplitude of the thin layers in the hinge region (red dots) as well as the averaged amplitude of the thick layers (blue dots) for three different models built up of 5, 10 and 15 thin layers, respectively. All amplitudes are normalized with their corresponding initial layer thickness. For both the thin and the thick layers the point of initiation of buckling indicated with the red and the blue beam, respectively, is approximately identical for all three models. It is at about 9% shortening for the thin layers and at about 24% for the thick layers. Also the amplification of the thick layers is approximately the same for all three models.

The main difference is the amplification of the thin layers of the multilayer stack. The more layers a multilayer stack is made of, the faster the individual thin layers amplify. For a model with a high number of layers, this leads to bigger amplitude of the thin layers at the initiation of buckling of the thick layers. This difference is not very big between the three models but still it is recognizable. Especially the thin layers in the model with five layers (figure 20a) have noticeable lower amplitude at the point of buckling initiation of the thick layers than the two other models.

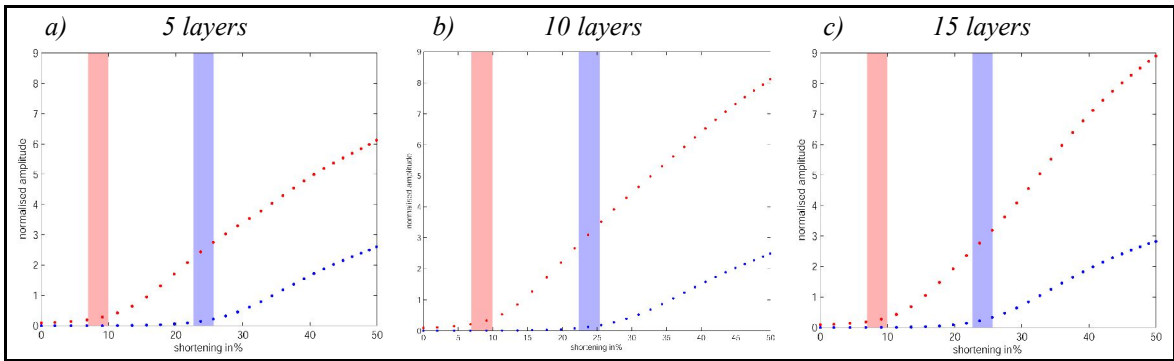


**Fig. 20:** Red: Averaged amplitude of the thin layers in the hinge region normalized with the initial layer thickness of the thin layers; Blue: Averaged amplitude of the two thick layers normalized with the initial layer thickness of the thick layers. The two beams indicate the initiation of buckling for the thin layers (red) and the thick layer (blue), respectively. The three subplots are modeled with a different number of thin layers.

For the three models with 5, 10 and 15 thin layers, respectively, the distance between the two thick layers is shown in figure 21. The red dots represent the distance measured normal to the folds in the hinge region while the blue dots show the minimal distance between the two layers, which is situated at the inflexion point. In all models the two distances evolve similarly up to a certain amount of far-field shortening. After this first phase of deformation the two lines separate. The distance in the hinge region increases steadily while the distance at the inflexion point increases slower and slower until it reaches a maximum value and decreases again. The far-field shortening at which the blue dots reach their maximum, is roughly the same for the three models, at 34%.

The main difference between the three models is the amount of shortening necessary to see a difference between the blue and the red dots. This separation takes place earlier for smaller numbers of thin layers. For the model with 15 thin layers (figure 21c) this separation takes place immediately before the distance at the inflexion point reaches its maximum and then decreases. On the contrary, the two lines in the model with five thin layers (figure 21a) separate at about 18% shortening and it needs another 16% before the maximum distance at the inflexion point is reached. This results in a much shallower gradient of the blue line between the separation and the maximum point, which means a slower increase of the distance between the two thick layers at the inflexion point compared to the models with more thin layers. With the knowledge of the initiation of buckling of the thick layers (figure 20) this leads to the following conclusion.

In a multilayer stack comprising of a small number of thin layers, shortly after the thick layers start to buckle the distance between the thick layers at the inflexion point evolve differently than in the hinge region. The distance at the inflexion point increases slowly. This slow increase decelerates in a relatively long phase and transforms to a fast reduction of the distance at the inflexion point. In a multilayer stack of many thin layers, the distance between the two thick layers increases as fast as the distance in the hinge region even after buckling of the thick layers has started. The distance at the inflexion point abruptly stops to increase and the two layers start to draw closer slowly. This abrupt change from an increasing to a decreasing distance at the inflexion point suggests a very short phase of shearing without flattening, while this phase lasts much longer in the case of a small number of thin layers. In all models the distance between the two thick layers at the inflexion point does not reach the initial value after 50% shortening, although the model with only five thin layers almost does, since the decrease of the distance is faster than in the models with more thin layers.

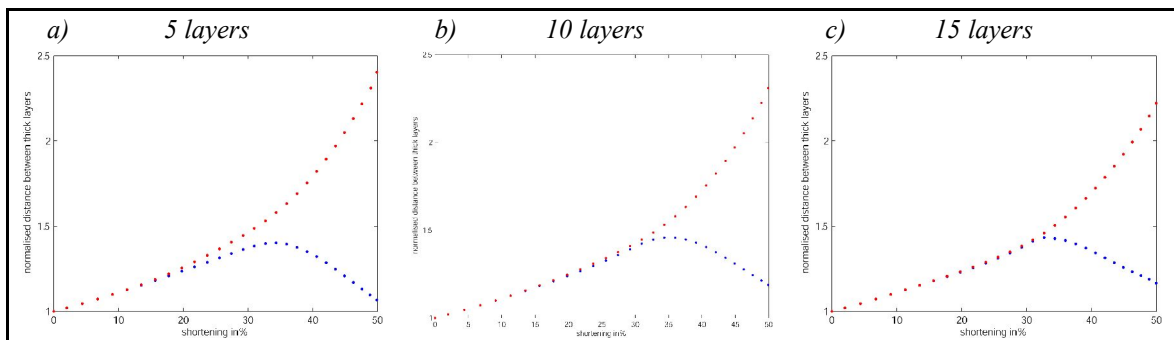


**Fig. 21:** Blue: Minimal distance between the two thick layers. This minimal distance is situated near the inflexion point; Red: Maximal distance between the two thick layers measured normal to the layers at the fold hinge. The three subplots are modeled with a different number of thin layers situated between the two thick layers.

## Chapter 5

# Discussion

### 5.1. Conditions for the occurrence of asymmetric parasitic folds

The insights into the strain distribution between two thick layers from chapter 3.5. can be used to understand the occurrence or absence of asymmetric parasitic folds in a multilayer stack situated between two thick layers. Figures 17 and 20 show that both the initial amplitude of the thick layers and the number of thin layers in between cause a change of the amplitude of the thin layers at the point of buckling initiation of the thick layers.

Schmid and Podladchikov, 2005 showed that the layers of a multilayer stack amplify faster than an isolated single layer and that the growth rate increases with an increasing number of layers. They derived an analytical solution for the growth rate of a multilayer stack, but this solution cannot be applied to the models of this study because their constraint of the number of layers is not fulfilled here. Nevertheless this multilayer effect on the growth rate is clear in figure 20. The second effect, the initial perturbation of the thick layers, can easily be understood assuming that the amplification of the two thick layers can be approximated with the amplification law of a single layer (equation 18). It is obvious that a smaller initial amplitude leads to a later initiation of buckling and a slower amplification.

Summarizing the amplitude of the thin layers at the point of buckling initiation of the thick layers increases with a higher number of thin layers as well as with a smaller initial perturbation of the thick layers. For the occurrence of asymmetric parasitic folds near the inflexion point, it seems to be necessary that the thin layers reach a sufficient amplitude before the thick layers start to buckle.

The three phases of deformation of a double layer system described in chapter 3.5.1. need to be reformulated for a multilayer stack between two layers.

- 1) The two thick layers have not started to buckle. The dominant deformation mechanism in the multilayer stack is layer-parallel compression. Due to the much higher initial amplitude the thin layers start to buckle and build symmetric folds.
- 2) The thick layers start to buckle which initiates a shear deformation in the multilayer stack with a shearing plane parallel to the thick layers. Shearing rotates the folds of the thin layers and produces their asymmetry.
- 3) The increasing amplification and closing of the thick layers leads to flattening of the multilayer stack in between with a flattening direction perpendicular to the thick layers. This flattening reduces the amplitudes of the thin layers. Shearing is still active during this deformation phase.

As already stated in chapter 3.5.2., these three phases of deformation only apply to the region near the inflexion point of the big-scale fold, and they can be tracked in figure 22. The figure is calculated with a multilayer stack with 15 thin layers and an initial amplitude of  $5 \cdot 10^{-3}$  for the two thick layers (see tables 4 and 6 for specifications). The final geometry of figure 22f is the same as shown in figures 16b and 19d. Subplot 22a visualizes the normalized distance between the two thick layers in the hinge region normal to the layers in red and the minimal normalized distance between the thick layers, situated at the inflexion point in blue. The normalized averaged amplitude of the thick layers is shown in blue in subplot 22b while the normalized averaged amplitude of the thin layers in the hinge region is shown in red. The vertical red lines indicate which amount of shortening the four geometries (subplots 22c to f) are drawn at.

Buckling of the thick layers starts at about 24% shortening, so subplot 22c at 20% shortening shows the geometry before the buckling initiation. The thin layers are already strongly amplified while the thick layers are still flat. This state represents the first phase of deformation. Subplot 22d at 30% shortening is drawn at the transition from the deformation phase 1 to 2. Buckling of the thick layers is initiated though the amplitude is still very low. The deformation mechanism in the multilayer stack is a combination of layer-parallel compression, which further amplifies the thin layers, and shearing due to buckling of the thick layers, which makes the existing parasitic folds asymmetric. Subplot 22e at 40% shortening shows the transition from the deformation phase 2 to 3. The thin layers of the multilayer stack do not amplify anymore but experience flattening normal to the thick layers, although flattening is not visible. The amplitude of the two thick layers increased and induced more shearing in the multilayer stack. The folds of the thin layers are obviously asymmetric now.

After 50% shortening in subplot 22f the deformation phase 3 is reached. Flattening of the multilayer stack near the inflexion point further decreases the folds of the thin layers and some of them even disappear. Those that survive become very asymmetric with a very long limb on the right side and a very short one on the left.

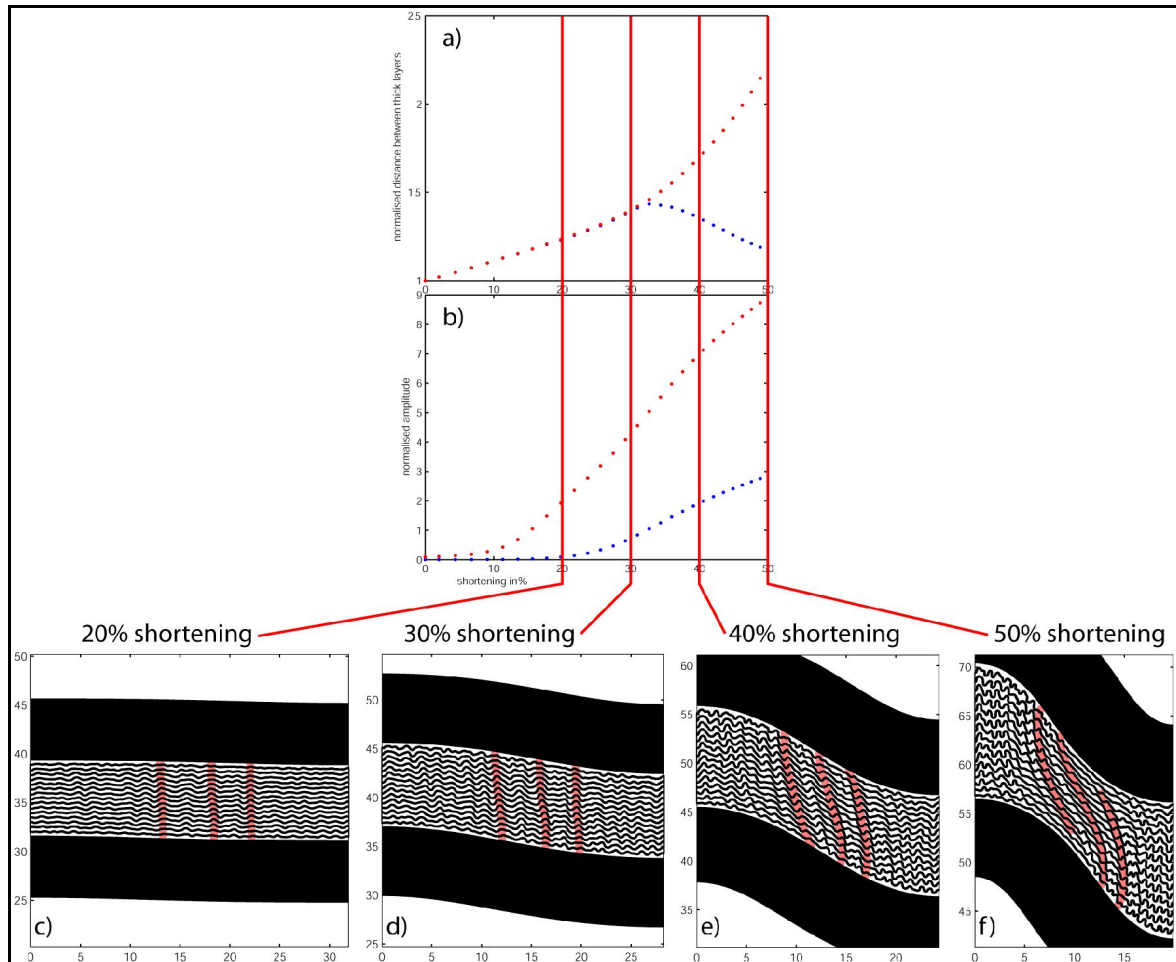


**Fig. 22:** Four stages of deformation in a multilayer stack with 15 thin layers. For numerical and geometrical specifications see table 4 and 6. a) Distance between the two thick layers normalized with the initial thickness of the thick layers. Red: Distance at the fold hinge normal to the layer boundary; Blue: Minimal distance, situated near the inflexion point. b) Red: Averaged amplitude of the thin layers near the fold hinge normalized with the initial thickness of the thin layers. Blue: averaged amplitude of the thick layers normalized with the initial thickness of the thick layers. c) – f) Geometries of the multilayer system at different amount of far-field shortening indicated with red lines in a) and b). Three initially vertical fold stacks are indicated in light red. For more information see text.

This evolution of the asymmetric parasitic folds as well as the investigations in chapter 4 suggest that the thin layers necessarily need to develop some amplitude before the thick layers start to buckle. It is the initial layer-parallel compression that produces symmetric folds and superimposed shearing that makes them asymmetric. In other words two sequential processes are necessary to produce asymmetric parasitic folds in a multilayer stack, although these two processes are both induced by constant far-field boundary conditions. The folds of the multilayer stack that amplified too little at the point of buckling initiation of the thick layers disappear during the third deformation phase when flattening normal to the thick layers decreases the amplitudes of the thin layers.

The selection of the folds that outlast the flattening phase is mostly due to the amplitude at the point of buckling initiation on the thick layers. Interestingly, the high amplitude folds at this point lie on top of each other and virtually build a vertical beam. Three of them are indicated in light red in figure 22c. The surrounding of such fold stacks is made up of layers with lower amplitudes and the folds disappear during the third deformation phase. The fold stack itself outlasts the deformation and deforms in the same way as the matrix between a double layer system without a multilayer stack in between (figures 22d–f and figure 12).

This behavior suggests that the deformation and the strain distribution between the two thick layers is approximately the same with and without a multilayer stack in between. This proposition is supported by figure 23 which shows the same multilayer sequence as in figure 22f with a double layer overlain in transparent light green. The double layer system is calculated with an identical setup as the multilayer system, only that no thin layers are set in between. After 50% shortening the thick layers of the two different systems are almost deformed identically. Since the multilayer stack does not influence the behavior of the thick layers, it is the strain distribution of the double layer system that controls the arrangement of the asymmetric parasitic fold stacks. Once these fold stacks are initiated in the first deformation phase they behave like passive beams during the second and the third phase.

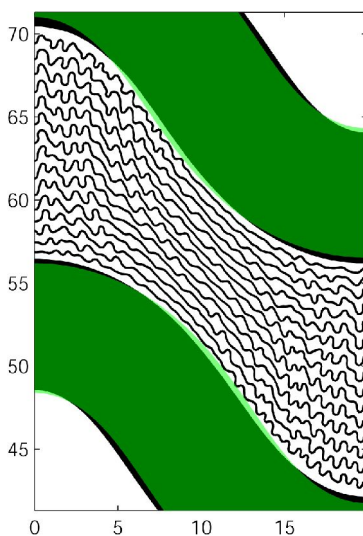


**Fig. 23:** Black: multilayer system with 15 thin layers situated between two thick layers after 50% shortening. For numerical and geometrical specifications see table 4 and 6. Transparent green: double layer system with exactly the same setup as the multilayer system but without the thin layers.

## 5.2. Model assumptions compared with a natural example

The amplitudes of the initial perturbation for the thin and the thick layers found in chapter 4.2. to produce the most suitable multilayer folds for this study need some more consideration and comparison with examples occurring in nature. The initial amplitudes are always defined as values normalized with the corresponding initial layer thickness and can be converted into absolute values.

$$\text{Initial amplitude of thin layers} \quad A_{thin, absolute} = A_{thin, normalised} \cdot H_{thin} = \frac{1}{10} \cdot 0.1 = 0.01 \quad (27)$$

$$\text{Initial amplitude of thick layers} \quad A_{thick, absolute} = A_{thick, normalised} \cdot H_{thick} = \frac{1}{5000} \cdot 5 = 0.001 \quad (28)$$

It is questionable whether absolute amplitude for the thick layers of one order of magnitude smaller than for the thin layers makes sense in nature. One could think of a turbidite sequence with many small events, representing the equally spaced multilayer stack, and a few mega events, representing the thicker layers, like the one shown in figure 24. The initial perturbation before folding of such a sequence is mostly due to deposition, e.g. ripple marks or groove casts. The thick layers are expected to have bigger perturbations, since the flow velocity of such a deposition is higher and therefore produces bigger ripples or other sole marks. From this point of view the used initial perturbations of the modeled multilayer stack are ill chosen. Nevertheless, this set of initial perturbations produces the best parasitic folds.



**Fig. 24:** Dr. Guy Simpson sitting in front of a turbidite sequence in the Makran area, south-eastern Iran. The sequence is composed of many approximately equally spaced thin layers and few thicker layers like the one to the right of Guy Simpson.

Not only the amplitude but also the type of the initial perturbation is to be considered. While on the thick layers a half cosine wave is imposed the thin layers are perturbed randomly. This half cosine wave is chosen in a way that the perturbation has the dominant wavelength of the thick layer for the single layer case. At the same time, the thin layers first need to establish the dominant wavelength out of the random perturbation before the real amplification begins. This process takes some time that the thick layers do not need. The high initial perturbation for the thin layers and the low initial perturbation for the thick layers reduce this time with respect to the buckle initiation of the thick layers. Using these initial perturbations allows the thin layers to buckle, which is desired. From this point of view the amplitudes of the initial perturbations do not need to be nature-like.

The described problem could be solved with a model, which does not only spans over a half wavelength but over three or four full wavelengths. In the current model the half cosine wave needs to be imposed on the thick layers. In a much broader model the initial perturbation of the thick layers could be random with an amplitude equal to or higher than for the thin layers. Such a model would be much more realistic but a new problem would appear. If the resolution should be the same as for the current model, a much higher number of nodes in the horizontal direction is needed. 1506 nodes would be needed for a model spanning over three full wavelengths resulting in a total number of 591858 nodes for a model with 20 thin layers. This amount of nodes cannot be handled with a standard personal computer and more sophisticated computer setups and programming tools are needed.

Considering a turbidite sequence, the assumption of initially parallel disturbed layers, meaning that the same perturbation is used for both the upper and the lower interface of each layer, is a simplification. Bigger perturbations are expected to be at the bottom of a stiff layer due to the higher flow velocity. The decreasing flow velocity during deposition also decreases the height of the perturbations. For a more accurate initial perturbation a lower and upper amplitude for both the thin and the thick layers is needed, whereas the upper amplitude is smaller. The effect of such reduced initial amplitude at the upper interfaces on the buckling process would be very little, since the buckling is controlled by the stronger perturbation of a layer, which is at the lower interface.

The thicker layers bounding the multilayer stack are not necessarily individual layers. As Schmid and Podladchikov, 2005 showed, thicker layers can also be multilayer stacks with much smaller interlayers, which effectively behave as single layers. One can imagine a turbidite sequence, which does not change in thickness of individual layers but in spacing between layers. Also many other geological settings than the discussed turbidite sequence can be build as a multilayer stack. Multilayers can occur from microscopic scale like the individual mica layers of a schist up to km-scale like the folds in a mountain belt.

## Chapter 6

# Conclusions and prospects

### 6.1. Conclusions

The investigation of a multilayer stack bounded by two much thicker layers and a double layer system built up of the two thick layers only, reveals that the deformation of the two bounding layers is not influenced by the presence of the multilayer stack in between. Thereby all layers and the matrix between and around them are linear viscous. The deformation history between the two thick layers can be divided into three phases:

- 1) Layer-parallel compression without buckling of the thick layers. The thin layers buckle since their initial amplitude is higher. They build symmetric folds
- 2) Buckling of the thick layers causes shearing in between. The thin layers become asymmetric.
- 3) High amplification of the thick layers causes flattening between and normal to the thick layers. The amplitudes of the thin layers decrease and only the biggest asymmetric folds survive.

Whether a fold of a thin layer outlasts the third deformation phase or not mainly depends on its amplitude when buckling of the two thick layers initiates. The higher this amplitude is, the less likely the fold is flattened. On one hand this obviously depends on the amplitude of the initial perturbations of the thin and the thick layers. On the other hand the number of thin layers influences the amplification of the multilayer stack. The more layers the stack contains, the faster they amplify. Therefore, a multilayer stack with a high number of thin layers and a high initial perturbation is most likely to develop asymmetric parasitic folds.

The asymmetric folds that survive the third deformation phase are vertically stacked at the point of buckling initiation of the thick layers. This vertical fold stack deforms almost like a passive beam during the second and third deformation phase while the smaller surrounding folds disappear.

The numerical approach of this study allows the calculation of finite strain ellipses and their coloring either with the accumulated von Mises equivalent strain or with the finite rotation angle due to rigid body rotation. This visualization technique applied to linear viscous single layer folds shows that the deformation mechanism in the layer clearly differs from the surrounding matrix. The layer is dominated by rigid body rotation without much shape change while the opposite applies for the matrix. In the amplifying layer two different kinds of neutral lines move from the outer to the inner side of the layer. The incremental neutral line, which moves earlier through the fold, is defined as the position where the layer-parallel strain rate is equal to zero. The finite neutral line moves later through the growing fold and is defined as the boundary between finite layer-parallel extension and compression. The movement of these two neutral lines show that the outer arc of a growing fold can easily be under a state of layer-parallel extension although the finite strain is still compressive.

## 6.2. Prospects

Now that the calculation and visualization of the finite strain ellipses is developed, many different problems are waiting to be visualized properly. Although many problems are numerically solved and the visualization does not seem to be a major scientific challenge, it would help to understand the solutions better, especially for field geologists, analogue modelers and students who are used to these ellipses.

Going on with the multilayer system used in this study the next step would be the investigation of the spacing between the thin layers and its influence on the development of parasitic folds. According to Schmid and Podladchikov, 2005 one would expect that narrowly spaced thin layers amplify slower. Therefore the chance to develop asymmetric parasitic folds near the inflexion point of the big scale fold is smaller.

In this study a basic model is used to investigate a multilayer system. This model could be changed or expanded in many ways, like:

- Different viscosity contrasts between the matrix and the thin and the thick layers, respectively
- Different initial perturbations which are closer to nature (problems with this, see chapter 5.2.)
- New geometrical setups, e.g. only one thick layer with a multilayer stack on top
- More sophisticated rheologies like power-law viscosity or visco-elasticity
- Heterogeneities in all possible parameters

These changes of the model are manifold and a huge amount of parameters are to be investigated. Therefore a basic model was chosen for this study and further changes should be considered wisely before done, since not all of them have a significant effect on the development of parasitic folds. Especially the refinement of the rheology would be interesting to know whether it has a big effect or not, since this modification is the most time-consuming.

# Acknowledgments

First and most of all I would like to thank Dr. Stefan Schmalholz, the Supervisor of this diploma project. You always motivated me to work hard, to go into detail and to try to really understand the physical meaning behind the problems. The endless discussions in your office and also during the coffee breaks made this learning process more pleasant and helped me a lot to understand both the physics and the numerics. Talking to you is better than any text book will ever be. I am really looking forward to my PhD project with you as my Supervisor. Stefan did not really need to motivate me because my motivation for numerical simulations grew during the outstanding lectures of Dr. Guy Simpson and Dr. Taras Gerya. You two introduced me to the finite difference and the finite element method in a very understandable way. I wish that more students could hear lectures like yours. I thank Prof. Jean-Pierre Burg for the possibility to join the field trip to the Makran region in Iran where the idea of this project arose together with Stefan and Guy. We had a great time and I will forever remember our smoky evenings. You also provided the infrastructure (computer) necessary for this project. Thomas Kocher, I thank you for your time that you took when I did not dare to go to Stefan's office because I thought that I had already taxed his patience too much. For the final review and orthographic corrections I thank Neil Allen. I hope my English was not too bloodcurdling.

Further, I want to thank the people in the Earth Science Department of ETH. Thank you for many talks and chats during the coffee breaks and at the Friday beer. A very big thank you goes to my fellow students, Felix Sager (thank you for your brownies, but please add nuts the next time, and do not burn them), Konrad Zeltner (I will miss your unhurried face on the other side of my computer), André Seiler (always ambrüf, never ambrii), Gaudenz Deplazes, Stefan Bucher, Cecile Matter, Marc Rierola, Michela Carradori, Flavio Matter, Bettina Baitsch-Ghirardello, Stephan Niggli, Pascal Spaar and everyone I forgot. You always made sure that I eat my lunch and did not stay behind my computer. We really had a great time here in Zurich and I hope to see many of you again after we have finished. ...and... Our Geofest was the best Geofest ever!

I want to thank my father who always let me decide which way I want to go and always stood behind my decisions. Without your support (not to forget financial as well) my studies would never have been possible. Last, but definitely not least, I want to thank you, Yolanda. Sharing the hard time of finishing the project with you made it so much easier, I hope for both of us. The time with you gave me the badly needed balance and helped me to think clearly afterwards. Your love supported me more than I can express.

# References

- Biot, M.A., 1961: Theory of folding of stratified viscoelastic media and its implications in tectonics and orogenesis; *Geol. Soc. Am. Bull.* **72**, 1595-1620
- Casey, M. and Butler, R.W.H., 2004: Modelling approaches to understanding fold development: implications for hydrocarbon reservoirs; *Marine and Petroleum Geology* **21**, 933-946
- Fletcher, R.C., 1977: Folding of a single viscous layer: Exact infinitesimal-amplitude solution; *Tectonophysics* **39**, 593-606
- Hughes, T.J.R., 2000: *The finite element method: Linear static and dynamic finite element analysis*; Dover Publications, Mineola; ISBN 0-486-41181-8
- Hughes, T.J.R., Liu, W.K. and Brooks, A., 1979: Finite element analysis of incompressible viscous flows by the penalty function formulation; *J. Computational Physics* **30**, 1-60
- Pelletier, D., Fortin, A. and Camarero, R., 1989: Are fem solutions of incompressible flows really incompressible? (Or how simple flows can cause headaches!); *Int. J. for numerical methods in fluids* **9**, 99-112
- Ramsay, J.G. and Huber, M.I., 1989: *The techniques of modern structural geology, Vol. 1: Strain analysis, 4th edition*; Academic Press, London; ISBN 0-12-576921-0
- Schmalholz, S.M., Podladchikov, Y.Y. and Jamtveit, B., 2005: Structural softening of the lithosphere; *Terra Nova* **17**, 66-72
- Schmid, D. and Podladchikov, Y.Y., 2005: Fold amplification rates and dominant wavelength selection in multilayer stacks; *Philosophical Magazine* ,
- Schmid, D.W., 2005: Rigid polygons in shear; *High-Strain Zones: Structure and Physical Properties. Geol. Soc. London Special Publications* **245**, 421-431
- Smith, J.V. and Marshall, B., 1993: Implications of discrete strain compatibility in multilayer folding; *Tectonophysics* **222**, 107-117
- Thomasset, F., 1981: *Implementation of finite element methods for Navier-Stokes equations*; Springer-Verlag, New York; ISBN 0-387-10771-1
- Williams, J.R., 1980: Similar and chevron folds in multilayers using finite-element and geometric models; *Tectonophysics* **65**, 323-338
- Zienkiewicz, O.C. and Taylor, R.L., 1994: *The finite element method, Vol. 1: Basic formulation and linear problems, 4th edition*; McGraw-Hill Book Company, Maidenhead; ISBN 0-07-084174-8

## Appendix A

# Mechanical equations and their discretization with the finite element method

### A1. Derivation of the governing equations

The equations governing the two-dimensional displacement in an incompressible viscous solid are derived by combining the following four relations:

$$\begin{aligned} 1) \quad \text{Force balance} \quad & \frac{\partial \sigma_{xx}}{\partial x} + \frac{\partial \sigma_{xy}}{\partial y} = 0 \\ & \frac{\partial \sigma_{xy}}{\partial x} + \frac{\partial \sigma_{yy}}{\partial y} = 0 \end{aligned} \tag{A1}$$

where  $\sigma_{xx}$  and  $\sigma_{yy}$  are normal stresses in the x- and y-direction, respectively.  $\sigma_{xy}$  is the corresponding shear stress. Compressive stresses are negative. Note that gravity is ignored.

$$2) \quad \text{Conservation of mass} \quad \frac{\partial v_x}{\partial x} + \frac{\partial v_y}{\partial y} = 0 \tag{A2}$$

where  $v_x$  and  $v_y$  are the components of velocity in the x- and y-direction, respectively. The assumption of mass conservation implies that an incompressible medium is considered.

$$3) \text{ Rheological relation } \begin{Bmatrix} \sigma_{xx} \\ \sigma_{yy} \\ \sigma_{xy} \end{Bmatrix} = -p \begin{Bmatrix} 1 \\ 1 \\ 0 \end{Bmatrix} + \begin{bmatrix} 2\mu & 0 & 0 \\ 0 & 2\mu & 0 \\ 0 & 0 & \mu \end{bmatrix} \begin{Bmatrix} \dot{\epsilon}'_{xx} \\ \dot{\epsilon}'_{yy} \\ \dot{\gamma}'_{xy} \end{Bmatrix} \quad (\text{A3})$$

where  $p$  is the pressure in the rock and  $\mu$  is the viscosity.  $\dot{\epsilon}'_{xx}$  and  $\dot{\epsilon}'_{yy}$  are deviatoric strain rates in the x- and y-direction, respectively.  $\dot{\gamma}'_{xy}$  is the deviatoric rotation rate defined as twice the deviatoric shear strain rate  $\dot{\epsilon}_{xy}$ , which is not computed here. This rheological equation defines an incompressible pure viscous medium.

$$4) \text{ Kinematic equation } \begin{Bmatrix} \dot{\epsilon}_{xx} \\ \dot{\epsilon}_{yy} \\ \dot{\gamma}_{xy} \end{Bmatrix} = \begin{Bmatrix} \partial v_x / \partial x \\ \partial v_y / \partial y \\ \partial v_x / \partial y + \partial v_y / \partial x \end{Bmatrix} \quad (\text{A4})$$

This kinematic equation finally defines the relationship between the total strain rates ( $\dot{\epsilon}_{xx}$ ,  $\dot{\epsilon}_{yy}$ ) and the rotation rate  $\dot{\gamma}_{xy}$ , respectively and the velocity field.

Using matrix notation, these four equations can be written more compactly as

$$1) \text{ Force balance } \mathbf{B}^T \vec{\sigma} = 0 \quad (\text{A1})$$

$$2) \text{ Conservation of mass } \nabla^T \cdot \vec{v} = 0 \quad (\text{A2})$$

$$3) \text{ Rheological relation } \vec{\sigma} = -p \vec{m} + \tilde{\mathbf{D}} \vec{\epsilon}' \quad (\text{A3})$$

$$4) \text{ Kinematic equation } \vec{\epsilon} = \mathbf{B} \vec{v} \quad (\text{A4})$$

where

$$\mathbf{B} = \begin{bmatrix} \partial / \partial x & 0 \\ 0 & \partial / \partial y \\ \partial / \partial y & \partial / \partial x \end{bmatrix} \quad (\text{A5})$$

$$\vec{\sigma} = \begin{Bmatrix} \sigma_{xx} \\ \sigma_{yy} \\ \sigma_{xy} \end{Bmatrix} \quad (\text{A6})$$

$$\nabla = \begin{Bmatrix} \partial / \partial x \\ \partial / \partial y \end{Bmatrix} \quad (\text{A7})$$

$$\vec{v} = \begin{Bmatrix} v_x \\ v_y \end{Bmatrix} \quad (\text{A8})$$

$$\vec{m} = \begin{Bmatrix} 1 \\ 1 \\ 0 \end{Bmatrix} \quad (\text{A9})$$

$$\tilde{\mathbf{D}} = \begin{bmatrix} 2\mu & 0 & 0 \\ 0 & 2\mu & 0 \\ 0 & 0 & \mu \end{bmatrix} \quad (\text{A10})$$

$$\vec{\epsilon} = \begin{Bmatrix} \dot{\epsilon}_{xx} \\ \dot{\epsilon}_{yy} \\ \dot{\gamma}_{xy} \end{Bmatrix} \quad (\text{A11})$$

$$\vec{\epsilon}' = \begin{Bmatrix} \dot{\epsilon}'_{xx} \\ \dot{\epsilon}'_{yy} \\ \dot{\gamma}'_{xy} \end{Bmatrix} \quad (\text{A12})$$

With the definition of the deviatoric strain rates, which is

$$\vec{\epsilon}' = \vec{\epsilon} - 1/3(\dot{\epsilon}_{xx} + \dot{\epsilon}_{yy})\vec{m} \quad (\text{A13})$$

it is possible to rewrite equation (A3) in terms of total strain rates.

$$\vec{\sigma} = -p\vec{m} + \mathbf{D}\vec{\epsilon} \quad (\text{A14})$$

where the new rheological matrix  $\mathbf{D}$  is defined as

$$\mathbf{D} = \begin{bmatrix} 4/3\mu & -2/3\mu & 0 \\ -2/3\mu & 4/3\mu & 0 \\ 0 & 0 & \mu \end{bmatrix} \quad (\text{A15})$$

The four equations((A1), (A2), (A14) and (A4)) can be rearranged in a way that the stresses and strain rates are eliminated. First one substitutes equation (A14) into (A1) which gives

$$\mathbf{B}^T \mathbf{D} \vec{\epsilon} - \mathbf{B}^T \vec{m} p = 0 \quad (\text{A16})$$

Substitution of equation (A4) in (A16) leads to the desired elimination.

$$\mathbf{B}^T \mathbf{D} \mathbf{B} \vec{v} - \mathbf{B}^T \vec{m} p = 0 \quad (\text{A17})$$

The multiplication of  $\mathbf{B}^T$  and  $\vec{m}$  in the second term is equivalent to the Nabla operator.

Thus the governing equations are

$$\mathbf{B}^T \mathbf{D} \mathbf{B} \vec{v} - \nabla p = 0 \quad (\text{A18})$$

$$\nabla^T \cdot \vec{v} = 0 \quad (\text{A2})$$

which is a set of three equations for the three unknowns  $v_x$ ,  $v_y$  and  $p$ .

## A2. Incompressibility with the finite element method

The incompressibility described by equation (A2) is not implemented directly in the finite element code. It is necessary to assume a compressible medium and converge the solution towards incompressibility within an iteration loop. Therefore, a more general compressible formulation of the equation (A2) is necessary.

$$(A2) \text{ becomes} \quad \frac{\partial p}{\partial t} = -K (\nabla^T \cdot \vec{v}) \quad (A19)$$

where K is the incompressibility or the penalty parameter.

The two governing equations after all these steps have the following form:

$$\mathbf{B}^T \mathbf{D} \mathbf{B} \vec{v} - \nabla p = 0 \quad (A20)$$

$$\frac{\partial p}{\partial t} = -K (\nabla^T \cdot \vec{v}) \quad (A21)$$

## A3. Discretization of equation (A20)

In the next two sections the discretization of equations (A20) and (A21) is carried out. For this purpose two different sets of shape functions are needed, one for the velocities ( $N_v$ ) and one for the pressure ( $N_p$ ). The velocity shape functions are bi-quadratic and continuous over the element boundaries, while the pressure shape functions are linear and discontinuous over the element boundaries. The corresponding element is a nine-node quadrilateral element with nine integration points. For further details see Appendix B. The techniques used to discretise equation (A20) and (A21) are described in many textbooks (e.g. Zienkiewicz and Taylor, 1994; Hughes et al., 1979).

For a more intuitive representation during the subsequent steps the terms are fully written out. Equation (A20) then has the following form.

$$\begin{aligned} \frac{\partial}{\partial x} \left( \frac{4}{3} \mu \frac{\partial v_x}{\partial x} - \frac{2}{3} \mu \frac{\partial v_y}{\partial y} \right) + \frac{\partial}{\partial y} \left( \mu \frac{\partial v_x}{\partial y} + \mu \frac{\partial v_y}{\partial x} \right) - \frac{\partial p}{\partial x} &= 0 \\ \frac{\partial}{\partial y} \left( -\frac{2}{3} \mu \frac{\partial v_x}{\partial y} + \frac{4}{3} \mu \frac{\partial v_y}{\partial y} \right) + \frac{\partial}{\partial x} \left( \mu \frac{\partial v_x}{\partial y} + \mu \frac{\partial v_y}{\partial x} \right) - \frac{\partial p}{\partial y} &= 0 \end{aligned} \quad (A20)$$

The first step in the discretization algorithm of equation (A20) consists of applying the shape functions as weighting functions (Galerkin approach), which in this case are the velocity shape functions. At the same time the integration over the whole finite element is carried out to get the weighted residual formulation.

$$\begin{aligned} \iint N_v^T \left( \frac{\partial}{\partial x} \left( \frac{4}{3} \mu \frac{\partial v_x}{\partial x} - \frac{2}{3} \mu \frac{\partial v_y}{\partial y} \right) \right) dx dy + \iint N_v^T \left( \frac{\partial}{\partial y} \left( \mu \frac{\partial v_x}{\partial y} + \mu \frac{\partial v_y}{\partial x} \right) \right) dx dy - \iint N_v^T \frac{\partial p}{\partial x} dx dy = 0 \\ \iint N_v^T \left( \frac{\partial}{\partial y} \left( -\frac{2}{3} \mu \frac{\partial v_x}{\partial y} + \frac{4}{3} \mu \frac{\partial v_y}{\partial y} \right) \right) dx dy + \iint N_v^T \left( \frac{\partial}{\partial x} \left( \mu \frac{\partial v_x}{\partial y} + \mu \frac{\partial v_y}{\partial x} \right) \right) dx dy - \iint N_v^T \frac{\partial p}{\partial y} dx dy = 0 \end{aligned} \quad (\text{A21})$$

Integrating every term by parts moves the spatial derivatives to the Galerkin shape functions and the weak formulation of the weighted residuals results. The arising boundary terms in this operation are ignored thereby as well as the changing sign, since the sign changes in every term.

$$\begin{aligned} \iint \frac{\partial N_v^T}{\partial x} \left( \frac{4}{3} \mu \frac{\partial v_x}{\partial x} - \frac{2}{3} \mu \frac{\partial v_y}{\partial y} \right) dx dy + \iint \frac{\partial N_v^T}{\partial y} \left( \mu \frac{\partial v_x}{\partial y} + \mu \frac{\partial v_y}{\partial x} \right) dx dy - \iint \frac{\partial N_v^T}{\partial x} p dx dy = 0 \\ \iint \frac{\partial N_v^T}{\partial y} \left( -\frac{2}{3} \mu \frac{\partial v_x}{\partial y} + \frac{4}{3} \mu \frac{\partial v_y}{\partial y} \right) dx dy + \iint \frac{\partial N_v^T}{\partial x} \left( \mu \frac{\partial v_x}{\partial y} + \mu \frac{\partial v_y}{\partial x} \right) dx dy - \iint \frac{\partial N_v^T}{\partial y} p dx dy = 0 \end{aligned} \quad (\text{A22})$$

At this point the physical values  $v_x$ ,  $v_y$  and  $p$  are approximated within the finite element. The approximation of the velocities are realised with the property vector containing the velocities at each of the nine nodes and the corresponding shape functions.

$$v_x = [N_{v1} \ N_{v2} \ \dots \ N_{v9}] \begin{Bmatrix} v_{x1} \\ v_{x2} \\ \dots \\ v_{x9} \end{Bmatrix} = N_v \vec{v}_x \quad , \quad v_y = [N_{v1} \ N_{v2} \ \dots \ N_{v9}] \begin{Bmatrix} v_{y1} \\ v_{y2} \\ \dots \\ v_{y9} \end{Bmatrix} = N_v \vec{v}_y \quad (\text{A23})$$

The property vector for pressures only contain one pressure value for each element (first entry) and two entries for the slopes of the linear dependency on the position in the two dimensional space.

Therefore the approximation has the following form.

$$p = [N_{p1} \ N_{p2} \ N_{p3}] \begin{Bmatrix} p_1 \\ p_2 \\ p_3 \end{Bmatrix} = N_p \vec{p} \quad (\text{A24})$$

Equations (A23) and (A24) are substituted into equation (A22) whereas the property vectors  $\vec{v}_x$ ,  $\vec{v}_y$  and  $\vec{p}$  are not incorporated into the integration since they are independent on the x- and y-position.

$$\begin{aligned}
& \iint \frac{\partial N_v^T}{\partial x} \frac{4}{3} \mu \frac{\partial N_v}{\partial x} dx dy \vec{v}_x - \iint \frac{\partial N_v^T}{\partial x} \frac{2}{3} \mu \frac{\partial N_v}{\partial y} dx dy \vec{v}_y + \iint \frac{\partial N_v^T}{\partial y} \mu \frac{\partial N_v}{\partial y} dx dy \vec{v}_x \\
& \quad + \iint \frac{\partial N_v^T}{\partial y} \mu \frac{\partial N_v}{\partial x} dx dy \vec{v}_y - \iint \frac{\partial N_v^T}{\partial x} N_p dx dy \vec{p} = 0 \\
& - \iint \frac{\partial N_v^T}{\partial y} \frac{2}{3} \mu \frac{\partial N_v}{\partial y} dx dy \vec{v}_x + \iint \frac{\partial N_v^T}{\partial y} \frac{4}{3} \mu \frac{\partial N_v}{\partial y} dx dy \vec{v}_y + \iint \frac{\partial N_v^T}{\partial x} \mu \frac{\partial N_v}{\partial y} dx dy \vec{v}_x \\
& \quad + \iint \frac{\partial N_v^T}{\partial x} \mu \frac{\partial N_v}{\partial x} dx dy \vec{v}_y - \iint \frac{\partial N_v^T}{\partial y} N_p dx dy \vec{p} = 0
\end{aligned} \tag{A25}$$

An appropriate reorganization of the whole equation leads to a more concise formulation.

$$\begin{aligned}
& \left( \iint \frac{\partial N_v^T}{\partial x} \frac{4}{3} \mu \frac{\partial N_v}{\partial x} dx dy + \iint \frac{\partial N_v^T}{\partial y} \mu \frac{\partial N_v}{\partial y} dx dy \right) \vec{v}_x \\
& + \left( - \iint \frac{\partial N_v^T}{\partial x} \frac{2}{3} \mu \frac{\partial N_v}{\partial y} dx dy + \iint \frac{\partial N_v^T}{\partial y} \mu \frac{\partial N_v}{\partial x} dx dy \right) \vec{v}_y - \iint \frac{\partial N_v^T}{\partial x} N_p dx dy \vec{p} = 0 \\
& \left( - \iint \frac{\partial N_v^T}{\partial y} \frac{2}{3} \mu \frac{\partial N_v}{\partial y} dx dy + \iint \frac{\partial N_v^T}{\partial x} \mu \frac{\partial N_v}{\partial y} dx dy \right) \vec{v}_x \\
& + \left( \iint \frac{\partial N_v^T}{\partial y} \frac{4}{3} \mu \frac{\partial N_v}{\partial y} dx dy + \iint \frac{\partial N_v^T}{\partial x} \mu \frac{\partial N_v}{\partial x} dx dy \right) \vec{v}_y - \iint \frac{\partial N_v^T}{\partial y} N_p dx dy \vec{p} = 0
\end{aligned} \tag{A26}$$

These two equations can be written in a more compact matrix notation in the following way.

$$\mathbf{KM} \vec{v} + \mathbf{G} \vec{p} = 0 \tag{A26}$$

where

$$\mathbf{KM} = \iint \tilde{\mathbf{B}}^T \mathbf{D} \tilde{\mathbf{B}} dx dy \tag{A27}$$

$$\mathbf{G} = - \iint \mathbf{B}_G^T N_p dx dy \tag{A28}$$

$$\vec{v} = \begin{pmatrix} v_{x1} \\ v_{y1} \\ v_{x2} \\ v_{y2} \\ \dots \\ \dots \\ v_{x9} \\ v_{y9} \end{pmatrix} \tag{A29}$$

$$\tilde{\mathbf{B}} = \begin{bmatrix} \frac{\partial N_{v1}}{\partial x} & 0 & \frac{\partial N_{v2}}{\partial x} & 0 & \frac{\partial N_{v3}}{\partial x} & 0 & \dots & \frac{\partial N_{v9}}{\partial x} & 0 \\ 0 & \frac{\partial N_{v1}}{\partial y} & 0 & \frac{\partial N_{v2}}{\partial y} & 0 & \frac{\partial N_{v3}}{\partial y} & \dots & 0 & \frac{\partial N_{v9}}{\partial y} \\ \frac{\partial N_{v1}}{\partial y} & \frac{\partial N_{v1}}{\partial x} & \frac{\partial N_{v2}}{\partial y} & \frac{\partial N_{v2}}{\partial x} & \frac{\partial N_{v3}}{\partial y} & \frac{\partial N_{v3}}{\partial x} & \dots & \frac{\partial N_{v9}}{\partial y} & \frac{\partial N_{v9}}{\partial x} \end{bmatrix} \quad (\text{A30})$$

and

$$\mathbf{B}_G = \begin{bmatrix} \frac{\partial N_{v1}}{\partial x} & \frac{\partial N_{v1}}{\partial y} & \frac{\partial N_{v2}}{\partial x} & \frac{\partial N_{v2}}{\partial y} & \frac{\partial N_{v3}}{\partial x} & \frac{\partial N_{v3}}{\partial y} & \dots & \frac{\partial N_{v9}}{\partial x} & \frac{\partial N_{v9}}{\partial y} \end{bmatrix} \quad (\text{A31})$$

#### A4. Discretization of equation (A21)

Before the finite element discretization of equation (A21) is carried out, the time derivation of the left side is approximated with a finite difference approach.

$$\frac{p^{new} - p^{old}}{\Delta t} = -K \left( \frac{\partial v_x}{\partial x} + \frac{\partial v_y}{\partial y} \right), \quad p^{new} + K \Delta t \left( \frac{\partial v_x}{\partial x} + \frac{\partial v_y}{\partial y} \right) = p^{old} \quad (\text{A32})$$

But now the Galerkin shape functions are applied, which in this case are the pressure shape functions. Integration over the element is carried out at the same time.

$$\iint N_p^T p^{new} dx dy + K \Delta t \left( \iint N_p^T \frac{\partial v_x}{\partial x} dx dy + \iint N_p^T \frac{\partial v_y}{\partial y} dx dy \right) = \iint N_p^T p^{old} dx dy \quad (\text{A33})$$

To avoid spatial derivation of the pressure shape functions, no integration by parts is carried out at this state. Instead the physical properties  $v_x$ ,  $v_y$  and  $p$  are approximated directly in the same way described above using equations (A23) and (A24). Again the property vectors are not incorporated into the integration.

$$\iint N_p^T N_p dx dy \vec{p}^{new} + K \Delta t \left( \iint N_p^T \frac{\partial N_v}{\partial x} dx dy \vec{v}_x + \iint N_p^T \frac{\partial N_v}{\partial y} dx dy \vec{v}_y \right) = \iint N_p^T N_p dx dy \vec{p}^{old} \quad (\text{A34})$$

Equation (A34) can be written more compactly with a matrix notation.

$$\mathbf{M} \vec{p}^{new} - K \Delta t \mathbf{G}^T \vec{v} = \mathbf{M} \vec{p}^{old} \quad (\text{A34})$$

where

$$\mathbf{M} = \iint N_p^T N_p dx dy \quad (\text{A35})$$

## A5. Derivation of the final equation system

Equations (A26) and (A35) together build up a system of three discrete equations.

$$\begin{bmatrix} \mathbf{KM} & \mathbf{G} \\ -K \Delta t \mathbf{G}^T & \mathbf{M} \end{bmatrix} \begin{Bmatrix} \vec{v} \\ \overrightarrow{p^{new}} \end{Bmatrix} = \begin{Bmatrix} 0 \\ \mathbf{M} \overrightarrow{p^{old}} \end{Bmatrix} \quad (\text{A36})$$

Note that in the first equation the vector  $\vec{p}$  is replaced by  $\overrightarrow{p^{new}}$  which means that the whole system becomes implicit. Using the second part of (A36) as an expression for  $\overrightarrow{p^{new}}$  and substituting this into the first part (A36) leads to a new equation.

$$\mathbf{KM} \vec{v} + \mathbf{G} \left( \overrightarrow{p^{old}} + K \Delta t \mathbf{M}^{-1} \mathbf{G}^T \vec{v} \right) = 0 \quad (\text{A37})$$

After some reorganization one gets the final equation that can be solved with a computer code.

$$\left( \mathbf{KM} + K \Delta t \mathbf{G} \mathbf{M}^{-1} \mathbf{G}^T \right) \vec{v} = - \mathbf{G} \overrightarrow{p^{old}} \quad (\text{A38})$$

Using the new expression

$$\mathbf{KL} = \mathbf{KM} + K \Delta t \mathbf{G} \mathbf{M}^{-1} \mathbf{G}^T \quad (\text{A39})$$

equation (A38) can be simplified even more.

$$\mathbf{KL} \vec{v} = - \mathbf{G} \overrightarrow{p^{old}} \quad (\text{A40})$$

The solution of equation (A40) results in a velocity field defined by the two components  $\vec{v}_x$  and  $\vec{v}_y$ .

## A6. Incompressibility with the Uzawa algorithm

As stated in section A2, the whole derivation including the final equation (A40) considers a compressible medium which does not conserve mass within a single element. This problem can be solved with a type of the Uzawa iteration algorithm. Therefore the following steps are carried out within an iteration loop. Let  $n$  be the iteration step.

- 1) The first solution of equation (A40) is carried out with an arbitrary property vector  $\vec{p}_{old}$ . Mostly a zero value is chosen.
- 2) The divergence of the velocity field is calculated with equation (A2) to check how bad the incompressibility assumption is satisfied. For a perfect incompressible medium the divergence is zero at every point.
- 3) A new pressure property vector is calculated using a modified version of equation (A34).

$$\vec{p}_n = \vec{p}_{n-1} + K \Delta t \mathbf{M}^{-1} \mathbf{G}^T \vec{v} \quad (\text{A41})$$

- 4) Equation (A40) is solved again by using the new pressure property vector from step 3) as  $\vec{p}_{old}$ .
- 5) Repeating steps 2) to 4) decreases the divergence of the velocity field from one iteration step to another. The iteration loop ends as soon as the divergence reaches a certain minimum value.

This Uzawa algorithm is performed every time step after the matrices  $\mathbf{KM}$ ,  $\mathbf{G}$ ,  $\mathbf{M}$  and  $\mathbf{KL}$  are assembled. Besides the solution of equation (A40), the velocity field, the pressure field results from performing the Uzawa iteration loop as well. Setting the minimum value for the divergence small enough guarantees that the incompressibility assumption is satisfied with a high accuracy.

To optimize the Uzawa iteration the penalty parameter  $K$  in equation (A19) has to be chosen wisely. To illustrate this figure A1 shows two simulations with  $K = 10^{-10}$  and  $10^{-14}$ , respectively. In figure 1a) more iteration steps were necessary for the divergence to reach the exit criteria, but at the same time the error of the solution is much smaller than in b). The geometrical setup for both cases is the same as described in chapter 2.6.1. The resolution is very small since it does not affect the accuracy of the matrix division. In order to calculate the error of the matrix division the solution  $\vec{v}$  is set back into equation (A40) and the right-hand side is calculated this way. The error is given in percent.

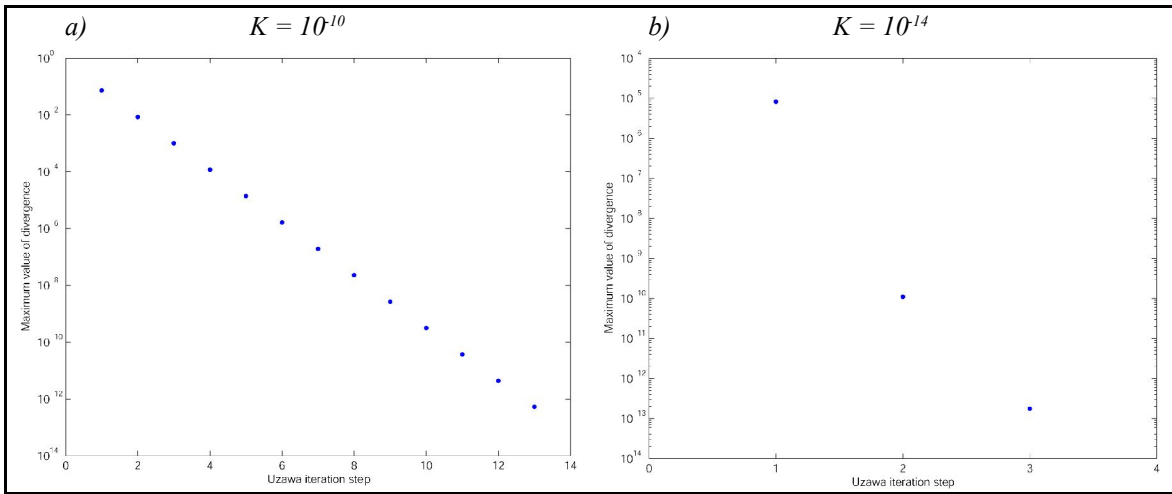


**Fig. A1:** Maximum value of the divergence of the velocity field versus the number of iteration steps. The divergence decreases faster in a) where  $K = 10^{-10}$  than in b) where  $K = 10^{-14}$ . The error of the matrix division in a) is always around  $10^{-10}$  and in b)  $10^{-6}$ .

## Appendix B

# Numerical integration and the use of local elements

### B1. Gauss-Legendre quadrature

The final equation (A40) in Appendix A is made up of various terms which contain integrals. For these integrals no analytical solution exists and they have to be evaluated numerically within the finite element program. For this purpose the so-called Gauss-Legendre quadrature is applied. This approach uses a local coordinate system  $(\zeta, \eta)$  and a quadratic reference element with a side length of 2 and its center in the zero point.

$$\int_{-1}^1 \int_{-1}^1 f(\xi, \eta) d\xi d\eta \simeq \sum_{i=1}^{nx} \sum_{j=1}^{ny} f(\xi_i, \eta_j) w_i w_j = \sum_{n=1}^{nip} f(\xi_n, \eta_n) w_n \quad (\text{B1})$$

where  $nx$ ,  $ny$  and  $nip$  are the number of integration points in x- and y-direction, respectively, and the total number of integration points per element.  $(\zeta_i, \eta_j)$  and  $(\zeta_n, \eta_n)$ , respectively are the local spatial coordinates of the integration points and  $w_i, w_j$  and  $w_n$ , respectively are the weights.

All terms in equation (A40) are expressed in terms of the global coordinates  $(x, y)$  while the numerical integration with equation (B1) requires a formulation in the local coordinate system. Therefore two transformations have to be made.

- 1) The local element is the same for every global element and does not change its shape, while the global system can deform heavily. For this practical reason the shape functions and their derivatives are defined in terms of local coordinates. To satisfy equation (A30) and (A31) the spatial derivatives have to be reformulated to global coordinates. The shape functions themselves do not need to be converted from local to global coordinates since a special isoparametric local element is chosen whose geometry is defined by the same shape functions. The transformation of the spatial derivatives is defined in the following way.

$$\begin{pmatrix} \frac{\partial}{\partial \xi} \\ \frac{\partial}{\partial \eta} \end{pmatrix} = \begin{bmatrix} \frac{\partial x}{\partial \xi} & \frac{\partial y}{\partial \xi} \\ \frac{\partial x}{\partial \eta} & \frac{\partial y}{\partial \eta} \end{bmatrix} \begin{pmatrix} \frac{\partial}{\partial x} \\ \frac{\partial}{\partial y} \end{pmatrix} = \mathbf{J} \begin{pmatrix} \frac{\partial}{\partial x} \\ \frac{\partial}{\partial y} \end{pmatrix} \quad (\text{B2})$$

where  $\mathbf{J}$  is the Jacobian matrix. This matrix can be found by differentiating the global coordinates with respect to the local coordinates. This is also done by multiplying the spatial derivatives of the shape functions with respect to local coordinates and the global coordinates of a particular element.

$$\mathbf{J} = \begin{bmatrix} \frac{\partial N_{v1}}{\partial \xi} & \frac{\partial N_{v2}}{\partial \xi} & \frac{\partial N_{v3}}{\partial \xi} & \dots & \frac{\partial N_{v9}}{\partial \xi} \\ \frac{\partial N_{v1}}{\partial \eta} & \frac{\partial N_{v2}}{\partial \eta} & \frac{\partial N_{v3}}{\partial \eta} & \dots & \frac{\partial N_{v9}}{\partial \eta} \end{bmatrix} \begin{bmatrix} x_1 & y_1 \\ x_2 & y_2 \\ x_3 & y_3 \\ \dots & \dots \\ x_9 & y_9 \end{bmatrix} \quad (\text{B3})$$

where  $x_l$  and  $y_l$  are the global coordinates of node number 1, etc. Given this, equation, the derivatives of the shape functions in terms of global coordinates can be found.

$$\begin{pmatrix} \frac{\partial}{\partial x} \\ \frac{\partial}{\partial y} \end{pmatrix} = \mathbf{J}^{-1} \begin{pmatrix} \frac{\partial}{\partial \xi} \\ \frac{\partial}{\partial \eta} \end{pmatrix} \quad (\text{B4})$$

- 2) In equation (A40) the area over which the integration has to be carried out is defined in terms of global coordinates. However, equation (B1) requires a formulation in the local system. The use of the determinant of the Jacobian matrix transforms the integration in the following way.

$$\iint f(x, y) dx dy = \int_{-1}^1 \int_{-1}^1 f(\xi, \eta) \det|\mathbf{J}| d\xi d\eta \quad (\text{B5})$$

Applying all these steps to equation A40 leads to the final summation which is done in the finite element code within a loop over all integration points of one element. Starting with the derivatives of the shape functions

$$\nabla_{\xi,\eta} \mathbf{N} = \begin{pmatrix} \frac{\partial N_1}{\partial \xi} & \frac{\partial N_2}{\partial \xi} & \frac{\partial N_3}{\partial \xi} & \cdots & \frac{\partial N_9}{\partial \xi} \\ \frac{\partial N_1}{\partial \eta} & \frac{\partial N_2}{\partial \eta} & \frac{\partial N_3}{\partial \eta} & \cdots & \frac{\partial N_9}{\partial \eta} \end{pmatrix} \quad (\text{B6})$$

one first applies equation (B4) and gets

$$\nabla_{x,y} \mathbf{N} = \mathbf{J}^{-1} \nabla_{\xi,\eta} \mathbf{N} = \begin{pmatrix} \frac{\partial N_1}{\partial x} & \frac{\partial N_2}{\partial x} & \frac{\partial N_3}{\partial x} & \cdots & \frac{\partial N_9}{\partial x} \\ \frac{\partial N_1}{\partial y} & \frac{\partial N_2}{\partial y} & \frac{\partial N_3}{\partial y} & \cdots & \frac{\partial N_9}{\partial y} \end{pmatrix} \quad (\text{B7})$$

This expression can now be used for creating the terms in equations (A27) and (A28), which can be written in a much more general way.

$$\iint f(\nabla_{x,y} \mathbf{N}) dx dy = \iint \mathbf{J}^{-1} f(\nabla_{\xi,\eta} \mathbf{N}) dx dy \quad (\text{B8})$$

Using equation (B5) converts the integration to the local coordinate system.

$$\iint \mathbf{J}^{-1} f(\nabla_{\xi,\eta} \mathbf{N}) dx dy = \int_{-1}^1 \int_{-1}^1 \mathbf{J}^{-1} f(\nabla_{\xi,\eta} \mathbf{N}) \det|\mathbf{J}| d\xi d\eta \quad (\text{B9})$$

Note that the shape functions themselves do not change during this transformation from global to local coordinates.

Applying the Gauss-Legendre quadrature leads to the desired summation formula.

$$\int_{-1}^1 \int_{-1}^1 \mathbf{J}^{-1} f(\nabla_{\xi,\eta} \mathbf{N}) \det|\mathbf{J}| d\xi d\eta = \sum_{n=1}^{nip} \mathbf{J}^{-1} f(\nabla_{\xi,\eta} \mathbf{N}) \det|\mathbf{J}| w_n \quad (\text{B10})$$

This summation can now be carried out for every element in the spatial domain.

**B2. The Q9/3 element**

Figure B1 shows the local reference elements used in the finite element code, which consist of nine nodes, one at each corner, one in the middle of each side and one in the very middle of the element. Inside the element there are nine integration points. The element is quadratic with a side length of 2 and its center lies in the zero point.

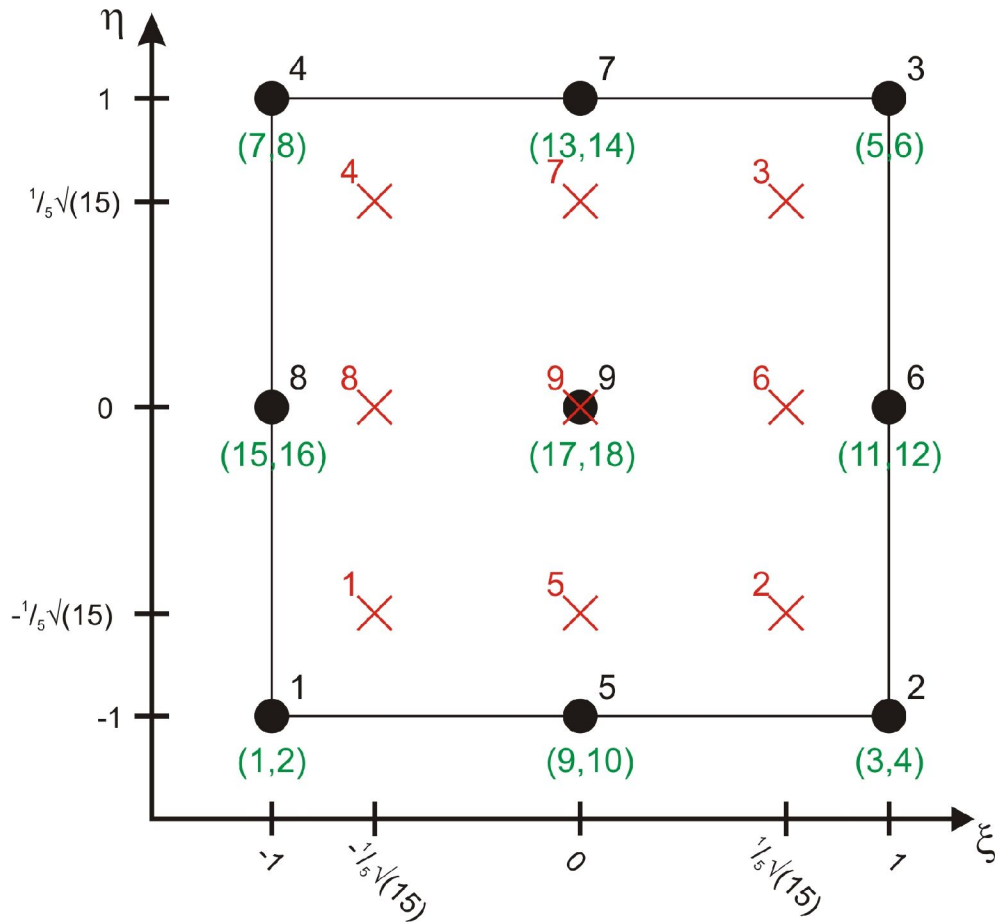


**Fig. B1:** Local reference element with nine nodes and nine integration points. Black are the nodes with their local numbers, green the corresponding degrees of freedom ( $v_x$  and  $v_y$ ) at each node and red the nine integration points. Note that the center of the element lies in the zero point.

For this type of element there are nine bi-quadratic shape functions which interpolate the unknown velocity function. The sum of all nine velocity shape functions is equal to one at every point within the element. Each function is equal to one at its corresponding node.

$$\begin{aligned}
N_{v1} &= \frac{1}{4}(\xi^2 - \xi)(\eta^2 - \eta) \\
N_{v2} &= \frac{1}{4}(\xi^2 + \xi)(\eta^2 - \eta) \\
N_{v3} &= \frac{1}{4}(\xi^2 + \xi)(\eta^2 + \eta) \\
N_{v4} &= \frac{1}{4}(\xi^2 - \xi)(\eta^2 + \eta) \\
N_{v5} &= -\frac{1}{2}(\xi^2 - 1)(\eta^2 - \eta) \\
N_{v6} &= -\frac{1}{2}(\xi^2 + \xi)(\eta^2 - 1) \\
N_{v7} &= -\frac{1}{2}(\xi^2 - 1)(\eta^2 + \eta) \\
N_{v8} &= -\frac{1}{2}(\xi^2 - \xi)(\eta^2 - 1) \\
N_{v9} &= (\xi^2 - 1)(\eta^2 - 1)
\end{aligned} \tag{B11}$$

The weights for the numerical integration are defined as follows.

$$\begin{pmatrix} w_1 \\ w_2 \\ w_3 \\ w_4 \\ w_5 \\ w_6 \\ w_7 \\ w_8 \\ w_9 \end{pmatrix} = \frac{1}{81} \begin{pmatrix} 25 \\ 25 \\ 25 \\ 25 \\ 40 \\ 40 \\ 40 \\ 40 \\ 64 \end{pmatrix} \tag{B12}$$

While the velocity shape functions are continuous over the element boundaries, the set of shape functions used to interpolate the pressure is discontinuous and linear within an element.

As stated in Appendix A, section A3 the property vector for the pressure contains one pressure value in the middle of each element and two slopes for the linear spatial dependency. Therefore the sum of all pressure shape functions is not equal to one, except for the zero point.

$$\begin{aligned}
N_{p1} &= 1 \\
N_{p2} &= \xi \\
N_{p3} &= \eta
\end{aligned} \tag{B13}$$

Figure B2 shows a simplified distorted global element-domain. Every element must be mapped to the local element. If the numerical integration was carried out on the global elements, the formulation would be different for each element.

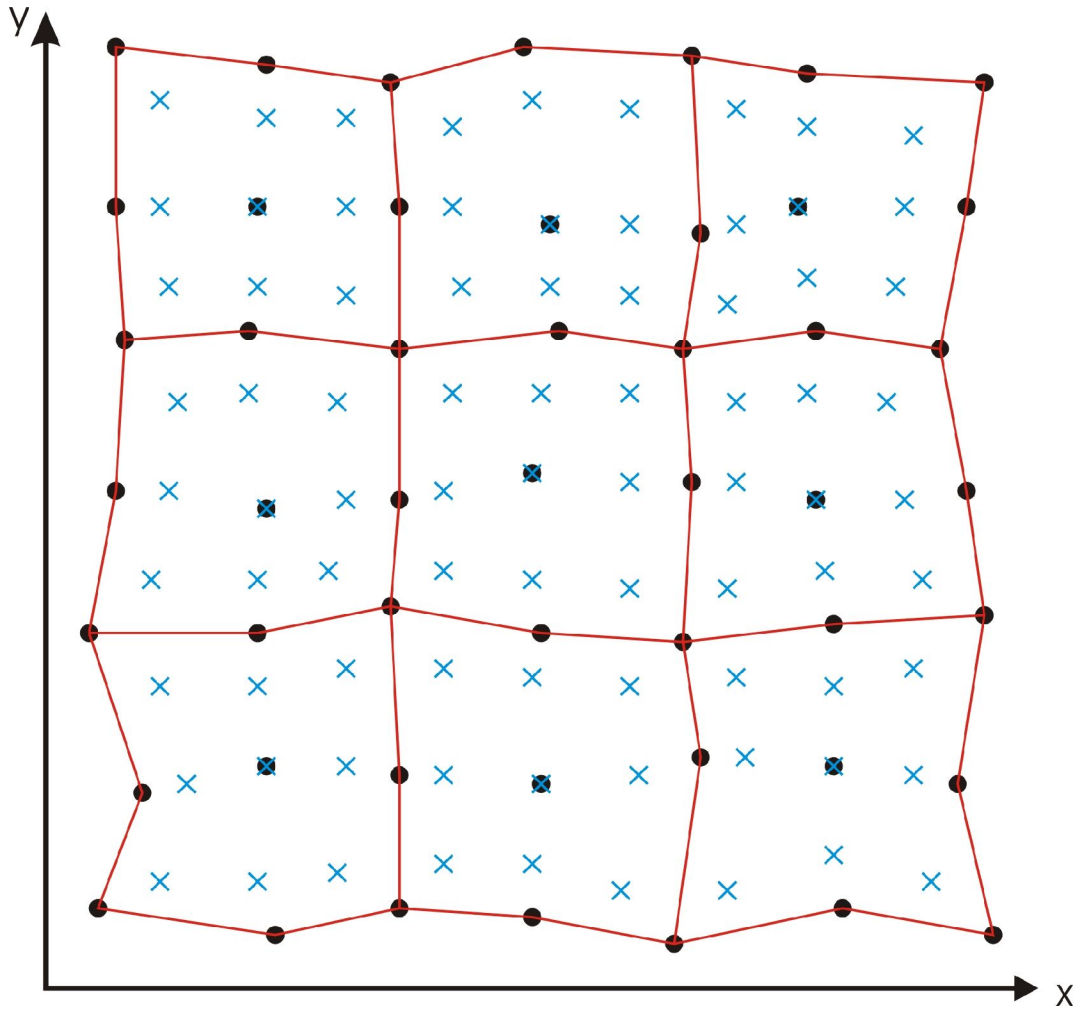
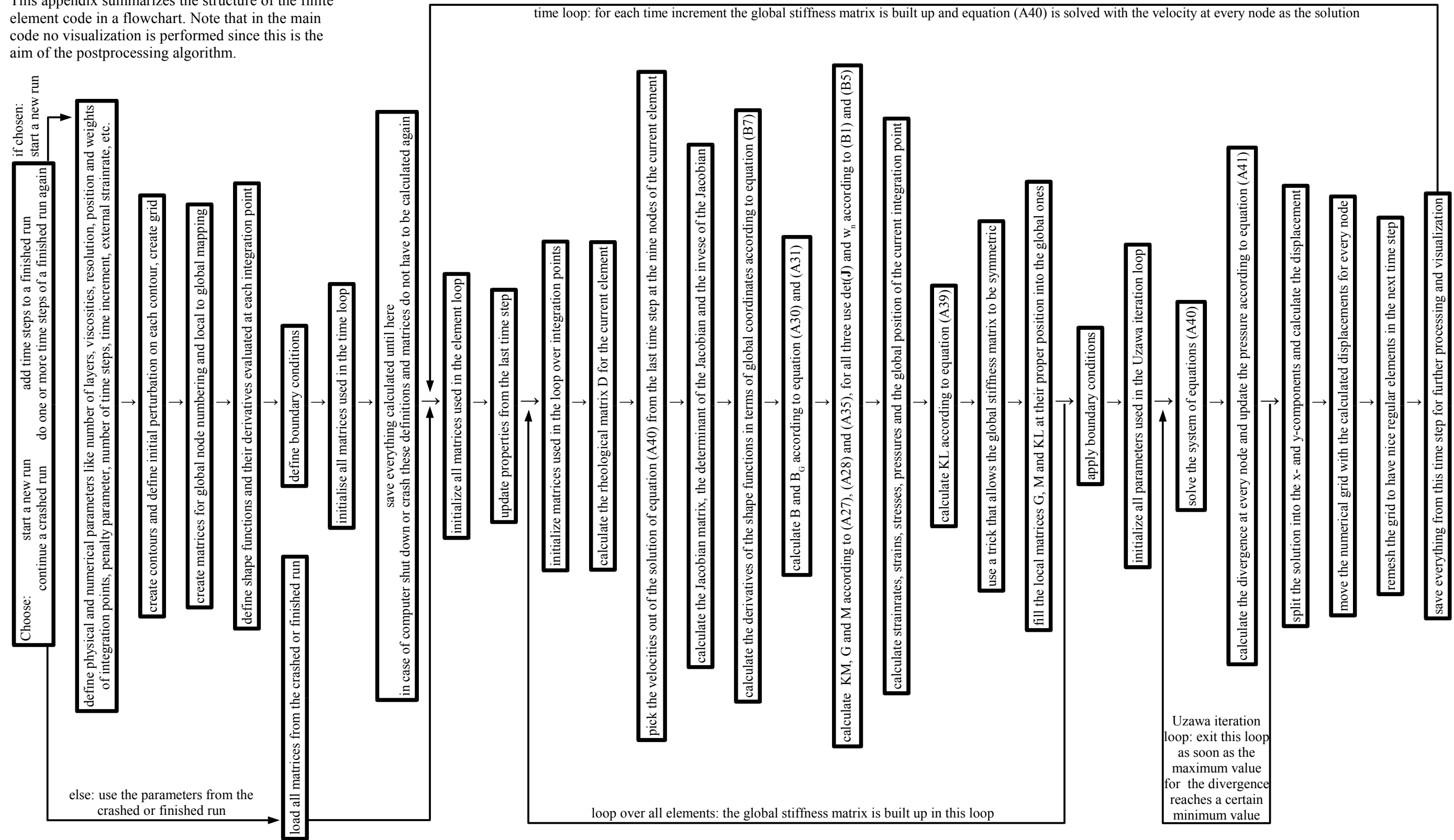


**Fig. B2:** Schematic distorted global elements. Every element has to be mapped to the quadratic and undistorted local element of Figure B1.

### Appendix C: Flowchart of the finite element code

This appendix summarizes the structure of the finite element code in a flowchart. Note that in the main code no visualization is performed since this is the aim of the postprocessing algorithm.



## Appendix D

### Dimensionless formulation

In geological systems the orders of magnitude of different properties are so different (e.g. timescale vs. strain rate) that the matrices in the finite element code become ill conditioned. Therefore three characteristic values are defined and all physical properties are normalized using these characteristic values.

<i>Property</i>	<i>Symbol</i>	<i>Unit</i>	<i>Used value</i>
<i>Characteristic length scale</i>	$L_c$	$[m]$	$1$
<i>Characteristic time scale</i>	$t_c$	$[s]$	$1$
<i>Characteristic viscosity</i>	$\mu_c$	$[Pa\ s]$	$1$

**Table D1:** Characteristic properties used in the finite element code for the normalization of all other properties

During this study all physical parameters are normalized using the three characteristic values in table D1. This normalization leads to dimensionless quantities. The physical value for each quantity can be derived by redoing the normalization. All normalizations are given in table D2.

<b>Quantity</b>	<b>Symbol</b>		<b>Normalization</b>
<i>Length</i>	$L$	=	$L_{physical} / L_c$
<i>Time</i>	$t$	=	$t_{physical} / t_c$
<i>Viscosity</i>	$\mu$	=	$\mu_{physical} / \mu_c$
<i>Velocity</i>	$v$	=	$v_{physical} / L_c \cdot t_c$
<i>Displacement</i>	$u$	=	$u_{physical} / L_c$
<i>Strain rate</i>	$\dot{\epsilon}$	=	$\dot{\epsilon}_{physical} \cdot t_c$
<i>Strain</i>	$\epsilon$	=	<i>no normalization</i>
<i>Rotation rate</i>	$\dot{\omega}$	=	$\dot{\omega}_{physical} \cdot t_c$
<i>Rotation</i>	$\omega$	=	<i>No normalization</i>
<i>Rotation angle</i>	$\theta$	=	<i>No normalization</i>
<i>Stress</i>	$\sigma$	=	$\sigma_{physical} / \mu_c \cdot t_c$
<i>Pressure</i>	$p$	=	$p_{physical} / \mu_c \cdot t_c$
<i>Incompressibility</i>	$K$	=	$K_{physical} / \mu_c \cdot t_c$

**Table D2:** Normalization for different quantities in the finite element code. This normalization leads to dimensionless formulations.

## Appendix E

# Strain distribution in single layer folds with different viscosity contrasts

In chapter 3.4. the finite and incremental strain distribution in a single layer fold with a viscosity contrast of 100 is analyzed. Appendix E expands this investigation to single layer folds with lower viscosity contrasts. For this reason three more experiments were performed with exactly the same geometrical and numerical setup as described in table 2 in chapter 3.4., but with viscosity contrasts of 10, 25 and 50, respectively. The visualization of these three runs is given in figure E1, whereas every picture is built up of two parts. While on the left-hand side the finite strain ellipses are colored with the accumulated von Mises equivalent strain, the coloring on the right-hand side is due to the finite rotation angle. The coloring schemes are the same for all pictures and the corresponding color-bars are given on every page. In three pictures (viscosity contrast 25, 50% shortening; viscosity contrast 50, 40% and 50% shortening) the incremental neutral line is positioned behind the finite strain ellipses as a thick red line. In all other pictures the incremental neutral line does not exist.

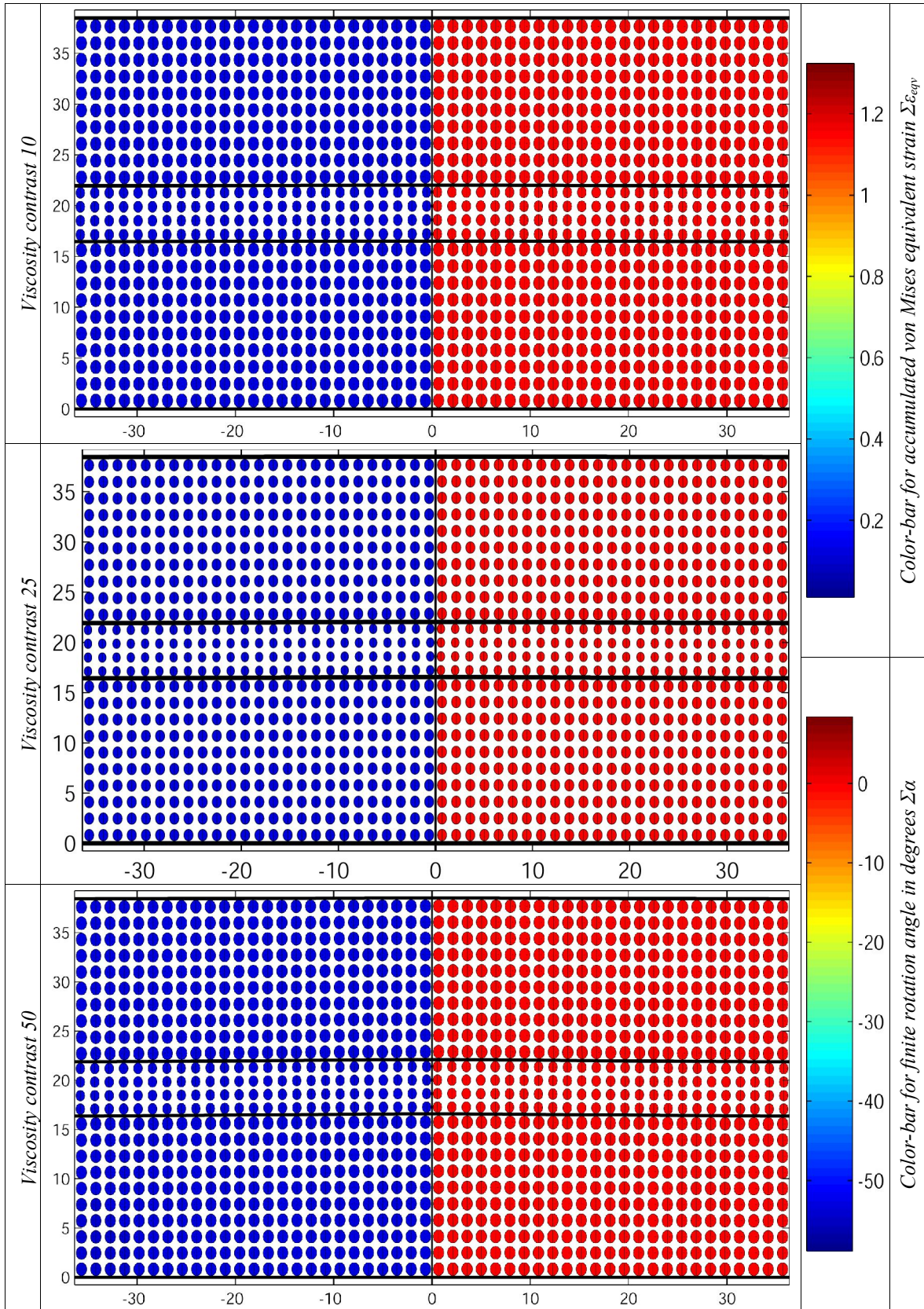
Figure E1 clearly shows that the amplification decreases with decreasing viscosity contrast. While the layer with viscosity 50 shows a nice amplification history, the layer with viscosity 10 hardly amplifies, even at 50% shortening. This difference in amplification has a major impact on the strain distribution and the neutral line. In all cases the rigid body rotation is dominant in the layer while the accumulated von Mises strain dominates the matrix. But both the accumulated von Mises equivalent strain and the finite rotation angle due to rigid body rotation differ much less between the layer and the matrix in the case of viscosity contrast of 10. For a viscosity contrast of 50 both quantities evolve differently in the layer and in the matrix from early deformation stages onward.

Not only the difference between layer and matrix, but also the difference within the matrix and within the layer, change with the viscosity contrast. This is mostly due to the different amplification of the folds. Since the layer with a viscosity contrast of 10 hardly evolves into a fold, the matrix surrounding it experiences an almost homogeneous strain rate at the layer boundary. On the contrary, the strain rate at the boundary between the layer with a viscosity of 50 and the surrounding matrix is far from homogeneous. The vertical strain rate at this interface is equal to the sum of the far-field vertical strain rate and the strain rate induced by the growing fold. Therefore the matrix near the inner arc of the fold is vertically much more extended than the matrix near the outer arc.

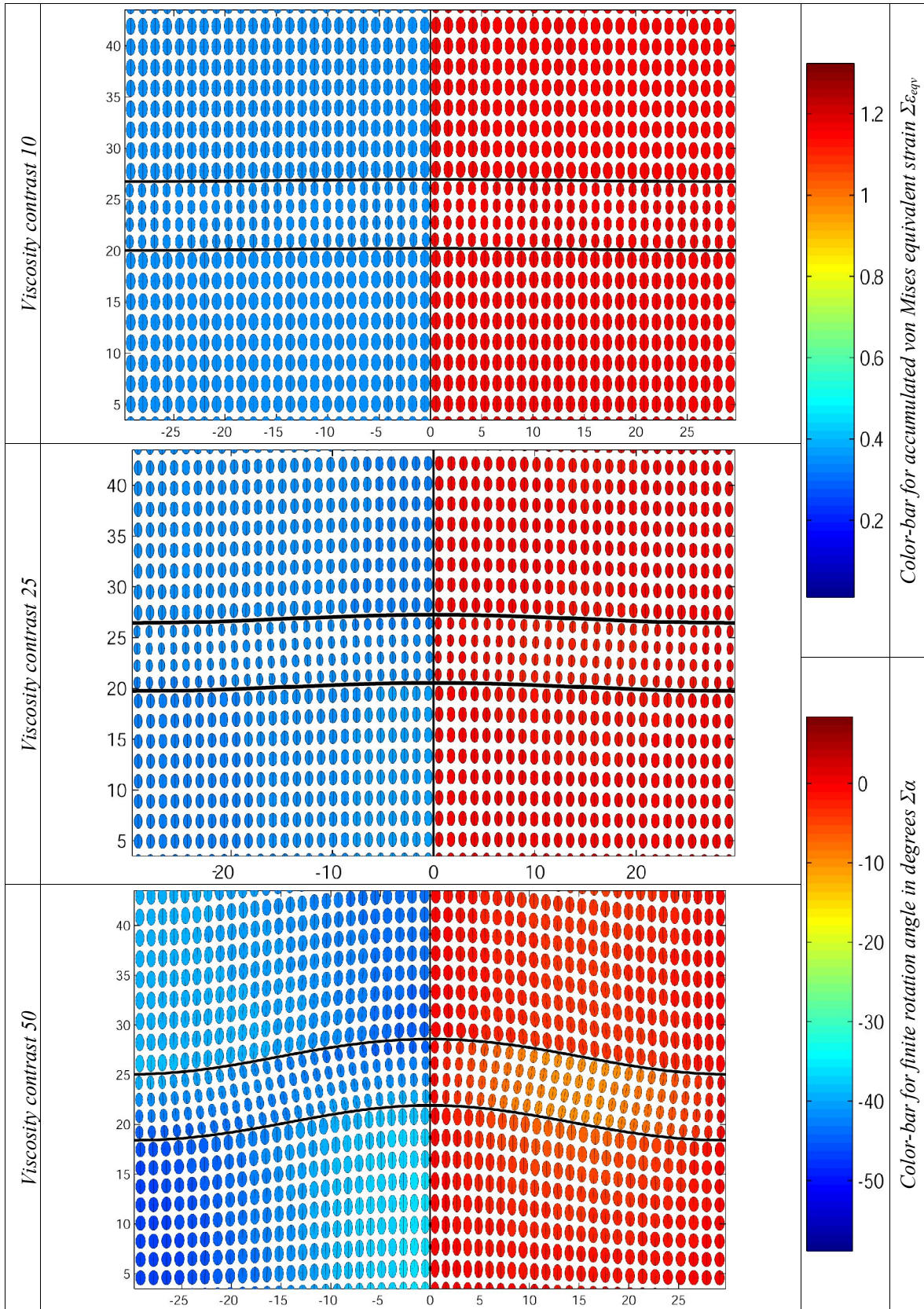
Within the stiff layer it is the finite rotation due to rigid body rotation that varies most notably. In all cases the rotation at the fold hinges is equal to zero during the whole deformation history. Because the amplification of the layer with a viscosity contrast of 50 is much higher than in the case of a viscosity contrast of 10, the variation of the finite rotation angle is also much higher. This is straightforward since the finite rotation angle for the stiff layers is directly visible from the geometry itself. Both the incremental and the finite neutral line behave different for different viscosity contrasts. The small bending in the hinge region of the layer with viscosity 10 causes too little folding-related extension in the outer arc compared to the far-field compression. Therefore, the compression dominates the outer arc and no neutral line can develop. In the case of a viscosity contrast of 25 the incremental neutral line develops between 40% and 50% shortening.

*Fig. E1 (pages 76 to 79): Growing single layer folds at different stages of external shortening and with different viscosity contrasts between the layer and the matrix. The finite strain ellipses on the left-hand side of every picture are colored with the accumulated von Mises equivalent strain while the ones on the right-hand side are colored with the finite rotation angle. Both color-schemes are the same for all pictures. If an incremental neutral line exists it is positioned behind the ellipses as a thick red line.*

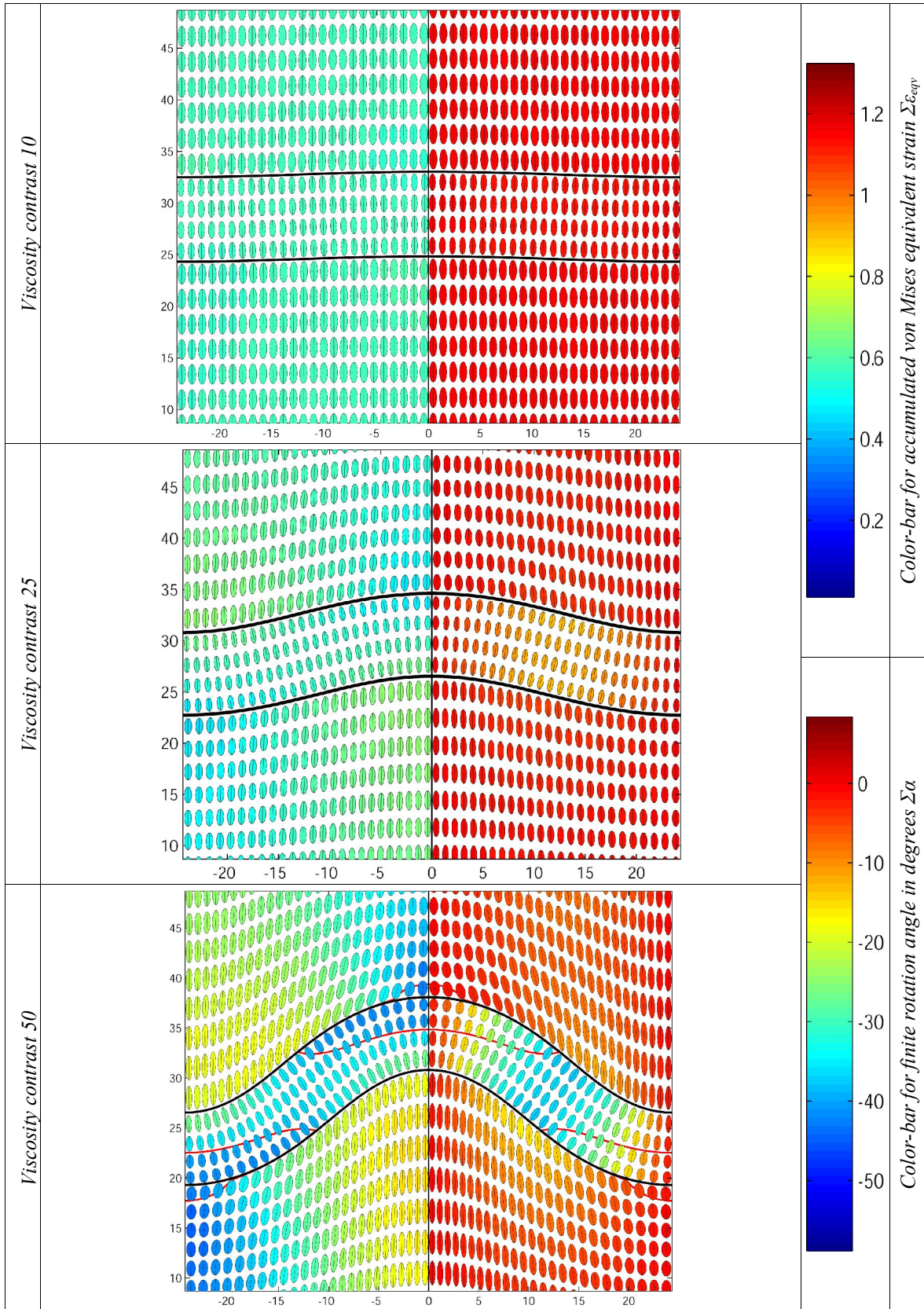
10% shortening



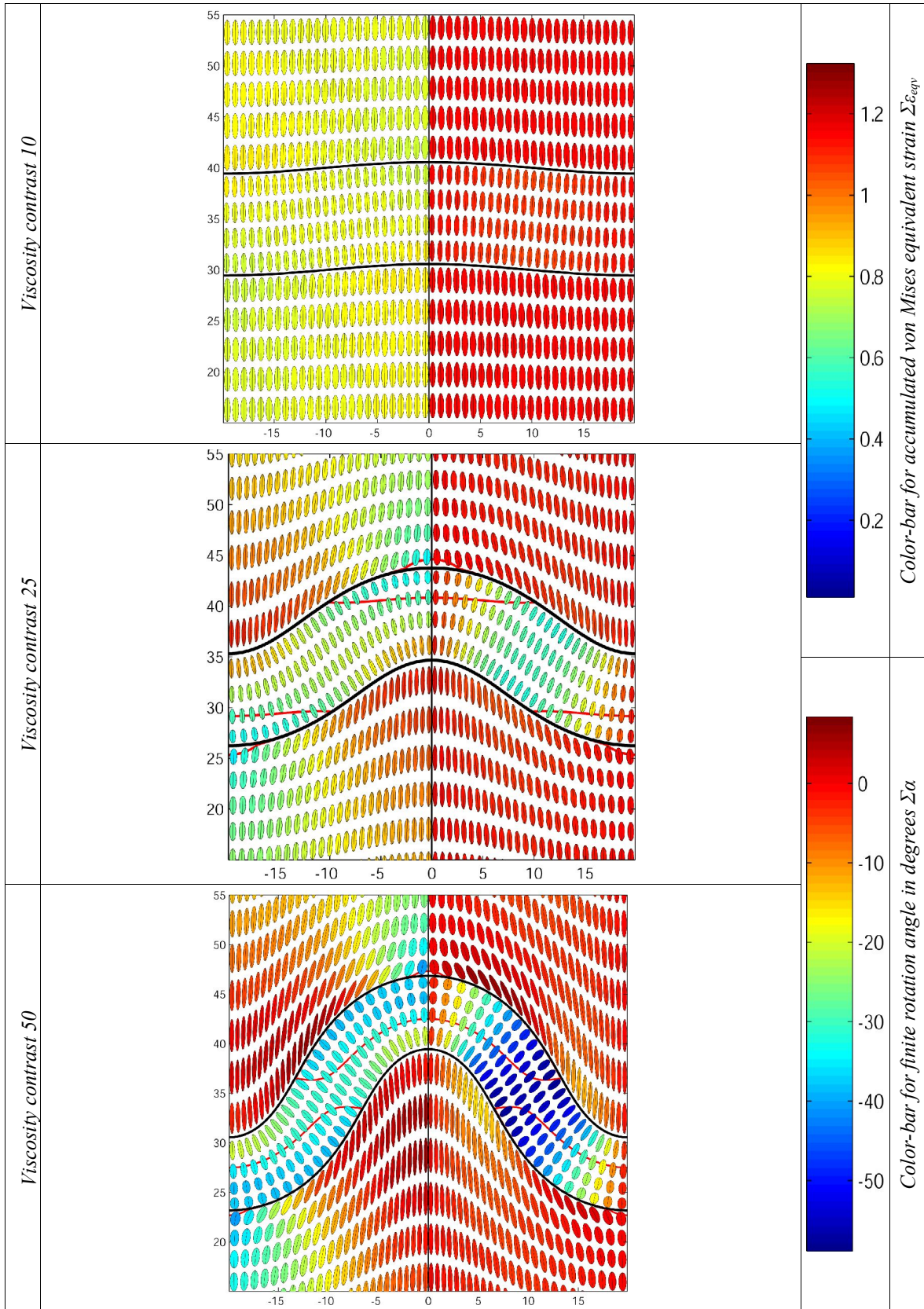
25% shortening



40% shortening



50% shortening



The case of a viscosity contrast of 50 is shown in detail in figure E2 with a single beam situated in the hinge region of the fold. For comparison the same setup is shown in figure 10, chapter 3.4.2. for a viscosity contrast of 100. Both the incremental and the finite neutral line move slower and later from outer arc to inner arc for the lower viscosity contrast. For the layer with a viscosity contrast of 100 the incremental neutral line develops between 10% and 25% shortening and the finite neutral line between 40% and 50%. On the contrary, the incremental neutral line for a viscosity contrast of 50 develops between 25% and 40% shortening and the finite neutral line between 60% and 70%. This clearly shows that the viscosity contrast between the matrix and the stiff layer has a major impact on the finite and on the incremental strain distribution.

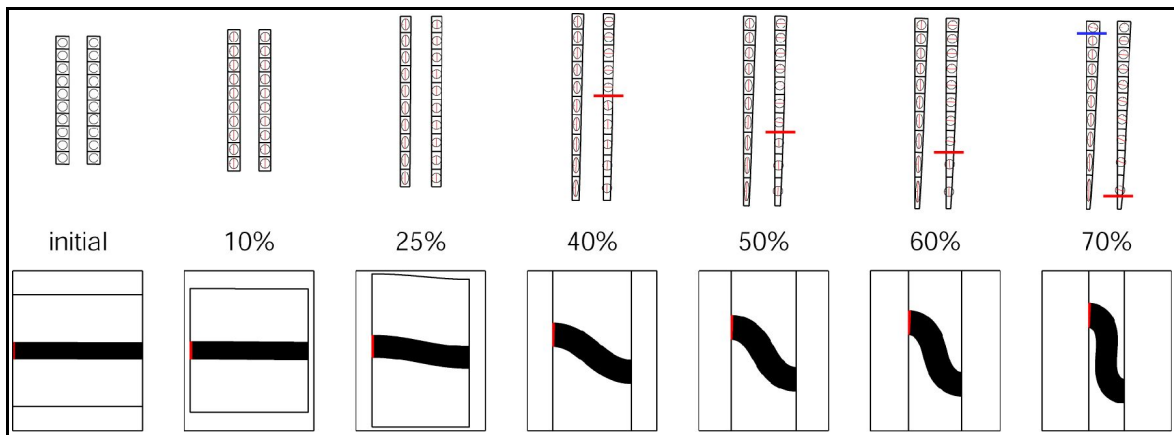


**Fig. E2:** Finite (left beams) and incremental strain ellipses in the fold hinge at different stages of shortening for a single layer fold with a viscosity contrast of 50. For comparison with a viscosity contrast of 100 see figure 10, chapter 3.4.2.